Experimental and numerical studies of the ignition of ammonia/additive mixtures and dimethyl ether burning velocities

Dai, Liming

DOI:
10.33612/diss.149049417

Experimental and Numerical Studies of the Ignition of Ammonia/Additive Mixtures and Dimethyl ether Burning Velocities

Liming Dai

university of groningen

The research described in this dissertation has been carried out at the Faculty of Science and Engineering (FSE), University of Groningen, The Netherlands, within the Energy Conversion Lab, Energy and Sustainability Research Institute Groningen.

The research presented in this dissertation was financially supported by the China Scholarship Council (CSC), the Chinese Ministry of Education.

university of groningen

Experimental and Numerical Studies of the Ignition of Ammonia/Additive Mixtures and Dimethyl ether Burning Velocities

PhD thesis

to obtain the degree of PhD at the
University of Groningen
on the authority of the
Rector Magnificus Prof. C. Wijmenga
and in accordance with
the decision by the College of Deans.

This thesis will be defended in public on

Monday 21 December 2020 at 11.00 hours

by

Liming Dai

born on 10 October 1990
in Jiangsu, China

Supervisor
Prof. H.B. Levinsky

Co-supervisor
Dr. A.V. Mokhov

Assessment Committee
Prof. T. Van Der Meer
Prof. A. Purushothaman Vellayani
Prof. D. Roekaerts

Contents

Chapter 1: Introduction

1.1 Motivation and objectives

At present, roughly 80% of the global energy demand, e.g. electricity power generation, traffic, heating and many other processes, is provided by fuel combustion [1]. Though the world is thriving based on the combustion of fossil fuels, it is simultaneously threatened by products formed in the combustion processes: unburned hydrocarbons, nitrogen oxides (NO and NO_2, collectively known as NO_x), soot and carbon dioxide (CO_2). The increasingly stringent emission regulations together with the fact of that fossil fuels are running out drive the search for clean and affordable alternatives to fossil fuels.

Hydrogen (H_2) is a promising alternative fuel. It can be produced using renewable energies, like solar and wind energy. As a carbon-free alternative fuel, H_2 can be used in combustion devices or fuel cells without carbon emissions [2]. However, despite its promise, H_2 faces challenges in becoming a renewable fuel on large scale due to its difficulties in storage and transportation from point of production to where it's needed. As a result, fuels that can be produced from renewable hydrogen and have higher energy densities are being considered, such as ammonia (NH_3) [3] and dimethyl ether (CH_3OCH_3 or DME) [4]. Ammonia is an efficient hydrogen energy carrier and could be burned directly in engines without carbon emissions. It has volumetric hydrogen density that is about 45% higher than that of liquid hydrogen [5]. In addition, ammonia can be liquefied under mild conditions, as it has similar physical properties to those of propane [5]. Last but not least, since it has long been widely used for production of fertilizer, nitrates, amines and textiles [6], ammonia has well established production, storage and transportation infrastructures. Regarding DME, it is an ideal alternative to diesel owing to its high cetane rating, higher than diesel (55–60), and good evaporation characteristics in the combustion chamber [7]. Besides, DME has a similar vapor pressure to that of LPG (liquefied petroleum gas) and thus can be used in the existing infrastructure for transportation and storage [8]. Moreover, DME has no C-C bonds, which decreases the tendency of soot formation [9]. It has been reported that emissions of soot, nitrogen oxides, carbon monoxide and unburned hydrocarbon are indeed lower in DME-fueled

engines, when using exhaust gas recirculation and proper injection strategies [9–11]. While DME can be used as an engine fuel itself, as discussed below, it can also be used as an ignition promoter to enhance the properties of ammonia for use in engines.

Despite their advantages in terms of CO_2 emissions, introducing alternative fuels in existing combustion devices is never a one-step task, due to their specific combustion properties. For instance, one of the greatest barriers to the implementation of ammonia as a fuel is its poor combustion properties, particularly the low burning velocity [12] and high auto-ignition temperature [13]. To overcome this barrier, the combustion of ammonia could be enhanced to the point at which it can be used with little or no alterations in existing combustion equipment by mixing it with more reactive fuels. For use in engines, hydrogen [14,15] and methane (CH_4) [16,17] are promising "additives" for ammonia-fueled spark-ignition (SI) engines due to their faster burning rate, while dimethyl ether (DME) [18,19] and diesel [20,21] can be used for compression-ignition (CI) engines due to their superior autoignition properties. However, the use of additives may lead to undesired side effects, particularly in ammonia fueled SI engines: hydrogen and methane have shorter ignition delay times, which increases the risk of knocking in SI engines. For CI engines, excessive use of diesel as an ignition promoter would increase soot emissions, while too little additive can lead to unstable ignition. To achieve stable combustion while maintaining low emissions, insight into the combustion properties of such alternative fuels and their mixtures is essential.

Fundamental investigations of the relevant combustion properties, including ignition delay time and burning velocity, can not only serve as input for the design of fuel compositions, but can also be used to interpret the combustion behavior in practical engines, thus aiding the design of ammonia-fueled engines. Importantly, fundamental studies on combustion characteristics performed at well-defined conditions are vital for assessing the ability of chemical mechanisms to predict combustion behavior. Using verified mechanisms in combustion models is a powerful tool for understanding the performance of new fuels in practical engines. In this thesis, we present experimental and numerical studies of a number of combustion properties of these new fuels and fuel mixtures. In particular, the ignition properties of ammonia and mixtures of ammonia with various additives and the propagation of DME flames are examined.

Regarding the literature on ammonia ignition, a number of studies have assessed the ignition delay times of NH_3 in shock tubes [22,23] and RCMs [13,24]. Mathieu and Petersen [22] reported shock tube measurements of ignition delay times of highly diluted NH_3/O_2 mixtures over a wide range of conditions, temperature (T = 1560-2455 K), pressure (P) in the range 1.4 - 30 atm and equivalence ratio (φ) between 0.5 and 2.0, and presented a mechanism that predicted their measurements well. Shu et al. [23] measured the ignition delay of ammonia/air mixtures in a shock tube at T = 1100-1600 K, P of 20 and 40 bar, and φ between 0.5 and 2.0. Their simulations using the mechanism of Mathieu and Petersen [22] also showed good agreement with their measurements. Pochet et al. [13] measured the ignition delay times of NH_3/H_2 mixtures (0, 10 and 25%vol. H_2) under fuel-lean conditions (φ = 0.2, 0.35, 0.5), high pressures (43 and 65 bar) and intermediate temperatures in the range 1000 - 1100 K in a rapid compression machine (RCM). Those authors evaluated the performance of five ammonia mechanisms from the literature (Konnov and De Ruyck [25], Zhang et al. [26], Song et al.[27], Dagaut and Nicolle [28], Nakamura et al. [29]) and found that none of the mechanisms predicted their measurements well. He et al. [24] reported RCM measurements of ignition delay time of NH_3 and NH_3/H_2 mixtures (1- 20% vol. H_2) at pressures from 20 to 60 bar, temperatures from 950 to 1150 K, and equivalence ratios from 0.5 to 2. They showed that, for their experimental conditions, the mechanism of Glarborg et al. [30] predicted pure NH_3 ignition delay times satisfactorily, but underpredicted the ignition delay times of the NH_3/H_2 mixtures by a factor of 3 (at P = 20 and 40 bar), while the mechanism from Klippenstein et al. [31] gave improved performance for the NH_3/H_2 mixtures, but overpredicted the results for pure NH_3 by more than a factor of 5. Very recently, Yu et al. [32], using n-heptane as a diesel surrogate, measured ignition delay times of NH_3/n-heptane mixtures in an RCM in the range T = 635–945 K, at pressures of 10 and 15 bar, and equivalence ratios of 1.0 and 2.0 with 0%, 20%, and 40% of the fuel energy contributed by NH_3. A NH_3/n-heptane mechanism was assembled based on the n-heptane mechanism from Zhang et al. [33] and the NH_3 (original) mechanism from Glarborg et al. [30]; significant discrepancies between experiments and the simulations were observed. More autoignition studies are needed to examine the advantages and limitations of ammonia blends with other potential combustion promotors, such as methane and dimethyl ether,

since which future transportation fuel will be used in which applications is at present uncertain. Therefore, the first objective of this thesis is to gain more insight in the autoignition behavior of pure NH_3, NH_3/H_2, NH_3/CH_4 and NH_3/DME mixtures (in Chapters 3-5) at conditions relevant to practical engines, as well as to compare the experimental results with the predictions using chemical mechanisms describing the oxidation of these fuels.

While the autoignition behavior of DME has been described in detail [34–39] and DME chemical mechanisms have been developed therein, the use of DME as a fuel also requires the experimental verification of the predictions of other flame properties as well. Premixed laminar flame studies play an important role in testing chemical mechanisms since they provide data, such as burning velocities and species profiles for this purpose. The majority of the experimental flame studies performed to date report the determination of free burning velocities [40–42]. However, only equivalence ratio, pressure and temperature of the unburned gas can be varied in this kind of experiment, where temperature variation is performed by heating unburned air-gas mixture [43]. To our knowledge, no previous studies have been performed examining DME flame conditions in which the burning velocity is below that of the free-flame, having flame temperatures below the adiabatic value. These conditions can be achieved in burner stabilized flames, where heat transfer to the burner reduces the burning velocity to the exit velocity. Following this idea, Sepman et al. [44] demonstrated a method to test chemical mechanism using temperature variation vs. exit velocity in burner stabilized hydrogen flames. The second objective of this thesis is to illustrate this method using DME. In Chapter 6, the flames temperatures are measured as a function of the exit velocity of the DME/air mixtures in a 1-D burner and the experimental results will be compared with flame simulations using different DME chemical mechanisms to evaluate their performance in predicting DME flame temperatures and free burning velocities.

Before proceeding to the more detailed presentation of the contents of this thesis, below we describe a number of general ideas that are used in the different chapters.

1.2 Homogenous, premixed reacting gas mixtures: equivalence ratio

Experimental and numerical studies on the homogeneous ignition of ammonia-based fuel mixtures and premixed laminar flames of dimethyl ether are performed in this thesis. A homogeneous, premixed fuel/oxidizer mixture can be characterized by its temperature, pressure and composition. In premixed mixtures, it is convenient to describe the composition using the equivalence ratio (φ), which defines the ratio of the fuel and oxidizer in the composition, relative to the ratio for a stoichiometric mixture. This can be expressed as:

$$\varphi = \frac{Fuel}{Oxidizer} * \frac{1}{f_{stoi}}, \tag{1.1}$$

where Fuel and Oxidizer are number of moles of fuel and oxidizer in the mixture, respectively, and f_{stoi} is the ratio of fuel to oxidizer given in the balanced chemical reaction describing combustion. For instance, for combustion of the hydrocarbon C_xH_y with balanced combustion reaction

$$C_xH_y + \left(x + \frac{y}{4}\right) O_2 = xCO_2 + \frac{y}{2} H_2O, \tag{R1.1}$$

f_{stoi} equals 1 / (x + y/4). A mixture with $\varphi = 1$ is called a stoichiometric mixture, if the fuel is provided in excess, $\varphi > 1$ and the mixture is termed fuel-rich. If the oxidizer is provided in excess, $\varphi < 1$ and the mixture is said to be fuel-lean. The real combustion of hydrocarbon fuels does not occur in a one-step reaction like *R*1.1; many elementary reactions and intermediates are involved [45]. Therefore, to gain more information on the combustion process, it is necessary to solve governing equations of combustion system using a detailed chemical mechanism. Briefly, a chemical mechanism is a set of chemical reactions describing the transformation of reactants into products. More details will be discussed in **Section 1.5**.

1.3 Zero-Dimensional homogenous ignition systems

Zero-Dimensional (0-D) homogenous ignition processes are of great interest in combustion science. From a practical point of view, this process is a simplification of compression-ignition (CI) engines, in which ignition is caused by the elevated temperature and pressure of fuel/air in the cylinder due to the mechanical compression. The data from ignition studies under conditions that simulate a 0-D homogeneous reactor experimentally provide a reliable benchmark for the design and development of CI engines.

A closed system can be described by the mass and energy conservation equations [45]. The total mass will remain constant, that is

Mass conservation:

$$\frac{d(\rho V)}{dt} = 0, \tag{1.2}$$

where ρ is the overall mass density, and V is the system volume. The mass fraction of each species changes with the time,

Species conservation:

$$\rho \frac{d(Y_k)}{dt} = \omega_k W_k, \qquad k = 1,2,3 \dots \dots \text{K}, \tag{1.3}$$

where Y_k is the mass fraction of *k*-th species in the system, ω_k and W_k are the net molar chemical production rate per unit of volume and molecular weight of the *k*-th species, respectively. The density can be derived from ideal gas law,

Ideal gas law:

$$\rho = \frac{P}{RT}\overline{W}, \tag{1.4}$$

where P is the pressure, R is the gas constant, T is the temperature and $\overline{W} = \frac{1}{\sum_{k=1}^{K}\frac{Y_k}{M_k}}$, the average molecular weight of the mixture. The energy equation can be derived from the first law of thermodynamics:

$$dU = \delta W + \delta Q, \tag{1.5}$$

where U is internal energy of the system and W is work be done to the external environment, Q is the heat added to the system. Substituting δW with $-PdV$ in Eq. (1.5), one receives

$$dU = -PdV + \delta Q, \tag{1.6}$$

which can be rewritten as

$$\frac{dU}{dt} + P\frac{dV}{dt} = \frac{dQ}{dt} = Q_{loss}, \tag{1.7}$$

where Q_{loss} is heat loss rate. The internal energy of the mixture is given by

$$U = \sum_{k=1}^{K} \rho V Y_k u_k\,, \tag{1.8}$$

where u_k is a specific energy of the *k*-th component. Differentiating equation (1.8), substituting in (1.7) and using (1.2-1.4), one can get

Energy conservation:

$$C_V \frac{dT}{dt} + P\frac{d\left(\frac{1}{\rho}\right)}{dt} + \frac{1}{\rho}\sum_{k=1}^{K} u_k \omega_k W_k = q_{loss}, \tag{1.9}$$

where $q_{loss} = \frac{Q_{loss}}{\rho V}$ is the heat loss per unit of mass and C_V is the specific heat capacity at constant volume, equal to $\sum Y_k \frac{du_k}{dT}$.

The set of governing equations from 1.2, 1.3, 1.4 and 1.9 contain (K+2) linear independent equations, while containing (K+3) unknowns (T, P, V, ρ, Y_1, …, Y_{k-1}). An additional equation should be given or one of the unknowns should be fixed to solve the set of equations. In practice, it is done by fixing one of the variables, for instance, specifying constant volume. A typical solution for a combustible mixture compressed to above its autoignition temperature in a closed, constant-volume system is shown in Fig. 1.1, for initial conditions T =T_0, P = P_0.

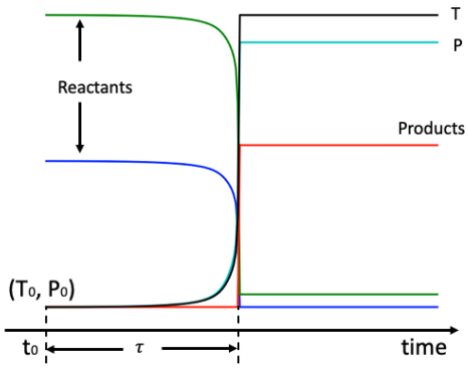

Figure 1.1. Time evolution of thermodynamic parameters (T, P, Y_k).

The ignition delay time (τ) can be defined as the time interval between maximum in the rate of temperature or pressure increase and t_0. Nevertheless, other definitions of the time at which ignition occurs exist, for example the time at 20% of the adiabatic flame temperature [46]. Several simulation programs have been developed to solve the set of governing equations. The program used in this study is the homogenous reactor code in the Cantera package [47].

1.4 One-Dimensional premixed laminar flames

1.4.1 Background

Flames are often classified as premixed (fuel and oxidizer mix first and burn later) or non-premixed (combustion and mixing of fuel and oxidizer occur simultaneously); each of these categories is further subdivided based on whether the fluid flow is laminar or turbulent. Three geometrically-simple types of laminar flames are often used in laboratory studies, as shown in Fig. 1.2. Fig. 1.2 (a) illustrates the geometry of one-dimensional (1-D) premixed flame, where fuel and air mix with each other before entering a porous burner. In a 1-D counterflow flame (Fig. 1.2b), the fuel and air flow in opposite directions. In the coflow flame (Fig. 1.2c), the flux of fuel and air are parallel to each other and diffuse radially into each other. All these types of flames are used to study flame structure and can be used to gain insight into chemical kinetics, by comparing model predictions with experimental results. Compared with counterflow and coflow flames, where the transport of fuel and oxidizer occur simultaneously with combustion and demand a more

complex description of flame structure, the 1-D premixed flame has the simplest flame structure, thus facilitating detailed experiment measurements of temperature and species profiles.

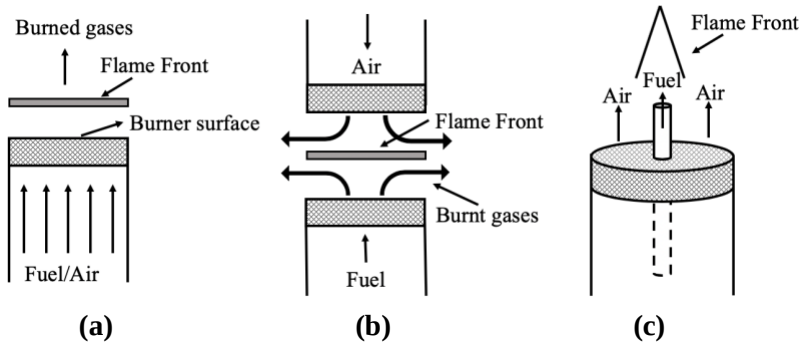

Figure 1.2. Schematic of laminar flames, (a) One-Dimensional premixed flame, (b) Counterflow flame, (c) Coflow flame.

One of the most important properties of premixed laminar flame is the 'free-flame' burning velocity, S_L, which is the velocity at which the 1-D flame front propagates relative to the velocity of the unburned mixture. S_L is determined by the specific fuel and the equivalence ratio, temperature and pressure of the initial mixture. The unburned mixture exits the burner with velocity v and thus the propagation velocity of flame front is v - S_L. If the v = S_L, the flame front is stationary above the burner surface as shown in Fig. 1.3 (a). In this special situation, there is no heat transfer from the burned gas to burner, resulting in an adiabatic flame or 'free flame' (neglecting radiation to the environment) [48]. If $v < S_L$, the flame front will move to the unburned mixture and lose heat to the burner, thereby reducing its temperature and, consequently, reducing the burning velocity to the exit velocity of the mixture. In the water-cooled burner used here, the heat lost to burner is taken away by cooling water circulating inside the burner. In this situation, the flame is called a burner-stabilized flame, as shown in Fig. 1.3 (b). If $v > S_L$, the flame front will move away from the burner and eventually lead to a blow off, as shown in Fig. 1.3 (c).

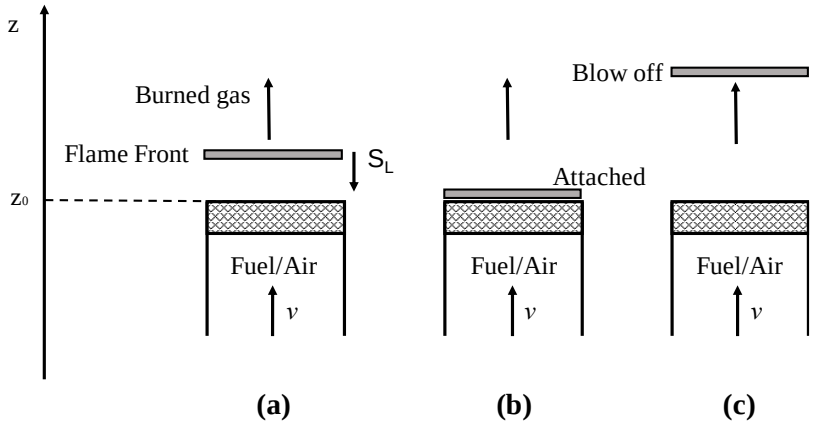

Figure 1.3. Schematic illustration of flame burning downstream on a porous burner. *v* is the exit velocity of fuel/air mixture and S_L is free burning velocity towards unburned mixture.

1.4.2 Governing equations for a one-dimensional premixed laminar flame

By definition, the properties of a stationary 1-D flame (e.g., temperature and gas compositions) depend only on one spatial (axial) coordinate, z. Neglecting the effects of external forces (e.g., gravity) and radiation, the conservation equations can be summarized as follows [45]:

Mass Conservation:

$$\frac{d(\dot{M})}{dz} = 0, \tag{1.10}$$

where $\dot{M}$ is the mass flux and *z* is the distance above the burner surface. $\dot{M} = \rho v$, where v is the velocity of the mixture.

Species Conservation:

$$\rho v \frac{dY_k}{dz} + \frac{d}{dz}(\rho Y_k V_k) = \omega_k W_k, \quad k = 1 \ldots K, \tag{1.11}$$

where V_k is the diffusion velocity of the *k*-th species, which is caused by the concentration gradients of the *k*-th species. The diffusion velocity can be assumed to be a known function of flame temperature and species concentrations [49].

Energy Conservation:

$$\frac{d}{dz}\left(\sum_k \rho Y_k(v+V_k)h_k - \lambda\frac{dT}{dz}\right) = 0, \tag{1.12}$$

where h_k is the specific enthalpy of *k*-th species, and λ is the coefficient of thermal conductivity. The governing equations (1.4) and (1.10-1.12) contain (K+2) linearly independent equations containing (K+3) unknowns (T, P, ρ, v, Y_1, …, Y_{k-1}).

Boundary conditions

It is important to consider two circumstances, burner-stabilized flames and freely propagating flames. The governing equations and boundary conditions at the hot boundary are the same for both flames, while the boundary condition at the cold boundary differ. For the hot boundary condition, since both flames reach equilibrium downstream (taken as $+\infty$), the gradients of temperature and composition vanish:

$$\frac{dY_k}{dz}|_{z=+\infty} = 0, \tag{1.13}$$

$$\frac{dT}{dz}|_{z=+\infty} = 0. \tag{1.14}$$

Burner stabilized flame

For a burner stabilized flame, v is a specified parameter, provided as exit velocity of unburned mixture as is the temperature at the burner surface (z = 0). The species boundary condition is specified through mass-flux fraction [50]. The mass fluxes of species into the burner are generally known, since they can be measured directly from mass-flow controllers. On the flame side of the burner face, however, there may be, and quite often are, diffusive-fluxes of species from the flame zone back to the burner face [51]. The mass-flux fraction of *k*-th species (ε_k) is obtained by integrating equation (1.11) while neglecting the species generated from reactions at burner surface (z_0),

$$\varepsilon_k|_{z=0} = Y_k + \frac{Y_k V_k}{v}, \tag{1.15}$$

$$T|_{z=0} = T_u, \tag{1.16}$$

Freely propagating flame

In the freely propagating flame, the burning velocity is obtained as an eigenvalue from the solution of the governing equations. The cold boundary condition for this case is prescribed as the initial composition and temperature of the mixture upstream of the flame front where there are no gradients of temperature or species fractions, taken at z = -∞:

$$T|_{z=-\infty} = T_u, \tag{1.17}$$

$$Y_k|_{z=-\infty} = \varepsilon_k. \tag{1.18}$$

The program used to solve the set of equations in this study is the steady-state one-dimensional flame code from the Cantera package [47]. A typical solution of the 1-D premixed free flame structure is illustrated in Fig. 1.4, where the flame can be divided into three regions, referred as the preheat zone, the reaction zone and the burned gas zone. The unburned mixture flows into the preheat zone and is warmed up by the heat generated from reaction zone and transported upstream. The reaction zone, known as flame front, is a thin layer, on the order of one millimeter at atmospheric pressure. In the reaction zone, the fuel is rapidly consumed and temperature increases sharply causing a buildup of a large radical pool. In the burned gas zone, recombination of radicals take place, moving the temperature and species concentrations towards equilibrium.

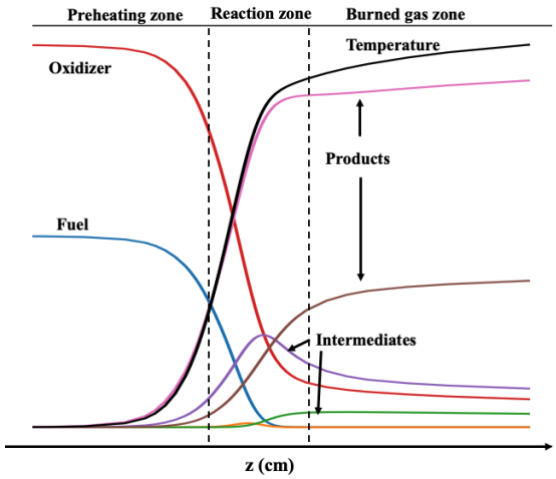

Figure 1.4. One-dimensional premixed free flame structure.

1.5 Chemical mechanisms

1.5.1 Chemical kinetics

The equations of conservation of species (1.3) and (1.11) both include the net production rate of species, ω_k, due to chemical reaction. These rates can be obtained from the mechanism describing the oxidation process. Consider the chemical reaction of the general type:

$$aA + bB \underset{k_r}{\overset{k_f}{\Leftrightarrow}} cC + dD\,, \tag{1.19}$$

where A, B, C, … represent the different species involved in the reaction, a, b, c … denote the numbers of moles of species A, B, C, …, and k_f and k_r are rate constants of forward and reverse reactions. For elementary reactions, the rate of change of species A can be expressed [45]:

$$\omega_A = \frac{d[A]}{dt} = -k_f[A]^a[B]^b + k_r[C]^c[D]^d. \tag{1.20}$$

where the square brackets denote concentration.

In equilibrium, the net rate of change of species A should be zero, therefore from (1.20), one receives equilibrium constant, K_{eq}:

$$K_{eq} = \frac{k_f}{k_r} = \frac{[C]_{eq}^c[D]_{eq}^d}{[A]_{eq}^a[B]_{eq}^b}. \tag{1.21}$$

K_{eq} is related to the free Gibbs energy [45],

$$K_{eq} = e^{\frac{-\Delta G}{RT}}, \tag{1.22}$$

where ΔG is standard free Gibbs energy change between products and reactants [45], which is a function of temperature [45]. Thus, the changing rate of species A is obtained by substituting (1.21) and (1.22) into (1.20),

$$\omega_A = -k_f [A]_{eq}^a [B]_{eq}^b + \frac{k_f}{K_{eq}} [C]_{eq}^c [D]_{eq}^d. \quad (1.23)$$

The rate constant (k_f) of many chemical reactions depends strongly on temperature. This temperature dependence is often expressed by a modified Arrhenius formula [45]:

$$k_f = AT^b e^{\frac{-E_a}{RT}}, \quad (1.24)$$

where A is the preexponential factor, b is the temperature exponent and E_a is activation energy, which corresponds to an energy barrier to be overcome during the reaction.

1.5.2 Chain reaction mechanism: the H_2/O_2 system

A chemical mechanism is the detailed list of the individual chemical steps that reactants take on their way to becoming products, including all intermediate species. For example, it describes which changes occur as the reactants H_2 and O_2 become H_2O, as will be illustrated below. In combustion, the individual steps are usually so-called elementary reactions, where the reactants physically react with each other according to the stoichiometry of the reaction. This is in contrast to the overall reaction to produce water, H_2 + 1/2 O_2 → H_2O; hydrogen molecules and oxygen molecules do not really react with each other to produce water, but progresses by a number of elementary reactions. Hydrogen requires approximately 30 elementary reactions and eight species to describe its oxidation over a wide range of pressures and temperatures [52]. To calculate how fast reactants become products, the rate constants for each step must also be known. The combustion of most fuels progresses by a 'radical chain reaction mechanism' and the terminology for chain reactions is used.

As a typical example of a detailed chain-reaction mechanism [51], the ignition of a homogenous hydrogen/oxygen mixture at high pressure and relatively low temperatures usually starts by the reaction [45]

$$H_2 + O_2 = H + HO_2, \quad (R1.2)$$

which is termed a *chain initiation step*, where reactive species (radicals) are formed from stable species. In this case, a hydrogen atom and an HO_2 radical are formed that can then react with other species in the reactive mixture. Other potential initiation steps, i.e. thermal dissociation of H_2 or O_2, are too slow to be important except at very high temperatures [51]. The very reactive H atom from *R*1.2 serves as a chain carrier, and can react with an O_2 molecule via,

$$H + O_2 = O + OH. \qquad (R1.3)$$

*R*1.3 is called a *chain branching step*, in which a reactive radical (H) reacts with stable species to forming two reactive species (O atoms and OH radicals). Chain-branching steps are essential for increasing the number of radicals in the reacting mixture. There are also *chain propagation steps*, in which the reaction consumes one radical and produces another, thus maintaining the number of radicals in the mixture. An example is,

$$OH + H_2 = H_2O + H. \qquad (R1.4)$$

More importantly, the chain branching steps compete with *chain termination steps*, which remove radicals from the system, for example

$$H + OH + M = H_2O + M \qquad (R1.5).$$

In addition, reactive radicals may be deactivated at the walls of vessel. Chain-termination reactions such as *R*1.6 are pressure dependent because of the necessity of a third body (M). When chain-termination reactions dominate, the net reaction will stop (in this case, no ignition). When chain-branching reactions are much faster than chain termination, the reaction rate will increase 'explosively', resulting in the sharp ignition process illustrated in Fig. 1.1.

A special reaction in fuels containing hydrogen is reaction *R*1.6,

$$H + O_2(+M) = HO_2(+M). \qquad (R1.6)$$

While HO_2 is a reactive radical, compared to the very reactive H atom it is relatively unreactive. Thus, this reaction is often considered to be chain terminating, which as will be seen below can be misleading.

The ignition process of hydrogen is mainly controlled by the competition between chain-branching reaction *R*1.3 and pressure-dependent *R*1.6, which here is considered chain terminating [53]. Reaction *R*1.6 has higher reaction order (third order) than *R*1.3 (second order) and the relative importance of *R*1.6 compared to *R*1.3 will increase with pressure [51]. At higher temperatures, the rate constant for $H + O_2 = O + OH$ becomes faster than that of $H + O_2 (+M) = HO_2 (+ M)$ and thus becomes dominant [54]. To illustrate this point, the rate constants of *R*1.3 and *R*1.6 taken from ref. [55] are shown in Fig 1.5. As can be seen, at high pressure (60 bar), the rate constant of *R*1.3 exceeds that of *R*1.6 at temperatures ~1500 K, while at atmospheric pressure, the rate constant of *R*1.3 surpasses the rate constant of *R*1.6 at roughly 1000 K.

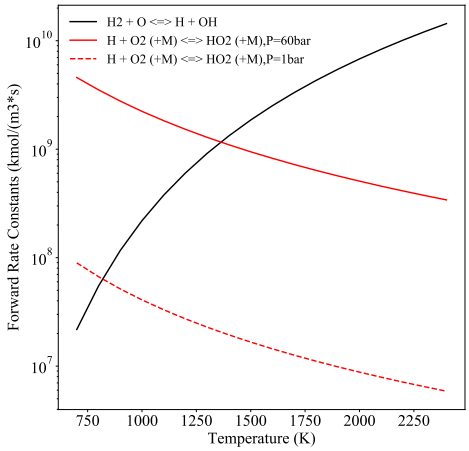

Figure 1.5. Rate constants of *R*1.3 (Solid black line) and *R*1.6 at 60 bar (Solid red line) and atmospheric pressure (dashed red line). Rate constants taken from ref. [55].

However, HO_2 can further react with H_2 or HO_2, leading to the formation of hydrogen peroxide H_2O_2, which further decomposes into two OH radicals,

$$HO_2 + H_2 = H_2O_2 + H \qquad (R1.7)$$

$$HO_2 + HO_2 = H_2O_2 + O_2 \qquad (R1.8)$$

$$H_2O_2(+M) = 2OH(+M). \qquad (R1.9)$$

Thus, while HO_2 formation prevents chain branching by *R*1.3, it also provides an additional pathway for chain branching through the reactions *R*1.6 - *R*1.9. This channel plays an important role in ignition of hydrogen and hydrocarbon fuels at high pressure and intermediate temperatures [53]. This importance can be demonstrated by performing ignition delay time calculation of H_2/air using mechanism from ref. [55] with and without H_2O_2 dissociation reaction (*R*1.9). As can be seen in Fig. 1.6, the ignition delay times are increased by a factor of 20 if the chain-branching channel through reaction *R*1.9 is blocked in the H_2 mechanism [55].

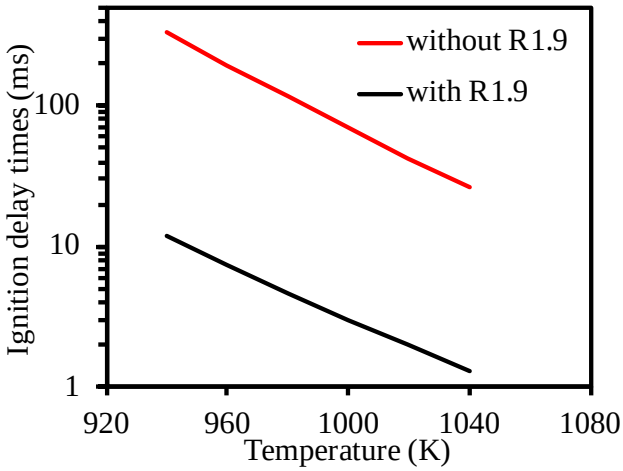

Fig. 1.6. Calculated ignition delay times of stoichiometric H_2/air mixture at 30 bar using mechanism from ref. [55], with (black) and without (red) R1.9 reaction.

Let's consider another situation, a H_2-air flame at atmospheric pressure. The free burning velocity (S_L) under these conditions are controlled not only by reactions discussed previously, *R*1.3 and *R*1.7, but also by other chain-branching reactions [56]:

$$O + H_2 = H + OH \qquad (R1.10)$$

$$HO_2 + H = OH + OH \qquad (R1.11)$$

and the chain-termination reaction, *R*1.6.

Interestingly, decomposition of H_2O_2 (*R*1.10), as a pressure dependence reaction shows dramatic influence on the ignition of hydrogen but doesn't influence the flame propagation. It can be demonstrated by performing free burning velocity calculation with and without channel *R*1.9, shown in Fig. 1.7. H_2O_2 formation requires HO_2 as precursor, however, HO_2 is mainly consumed by abundant reactive radicals, H, O and OH under the conditions discussed here. Thus, the channel of H_2O_2 formation and decomposition is completely unimportant for the free burning velocity of H_2/air mixture at atmosphere.

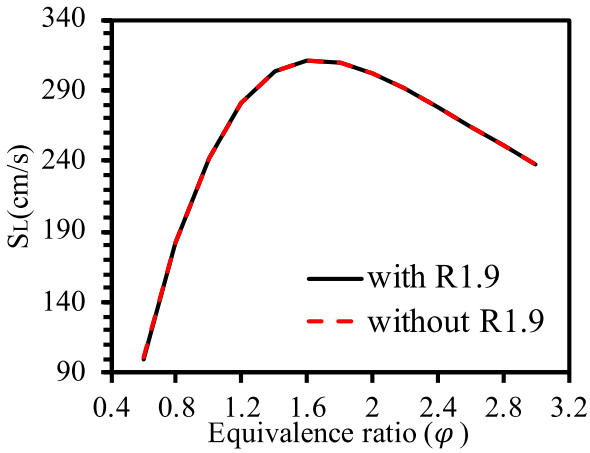

Figure 1.7. Calculated free burning velocity of stoichiometric H_2/air mixture at P_0= 1 atm and T_0=298 K, using mechanism from ref. [55], with (black line) and without (dashed red line) *R*1.9 reaction.

These examples show that the oxidation process under different conditions can be controlled by different elementary reactions. Therefore, insight into the important elementary reactions is essential to understand the oxidation process of different fuels under different conditions and to provide the possibility of controlling the oxidation process.

1.5.3 Development, analysis and testing of chemical mechanisms

As mentioned previously, a chemical mechanism is a set of elementary reactions quantified with rate constants. Since combustion systems can involve changes in temperature and pressure, to calculate combustion properties like burning velocity and ignition delay time, it is also necessary to have thermophysical/chemical data describing the system. Thermodynamic data is essential in determination of heat release and for the equilibrium

constants for the elementary reactions used in the mechanism. Transport data is necessary to characterize combustion properties having spatial gradients in temperature or concentration, such as in calculations of flame structure. Fortunately, thermodynamic and transport data are often expanded and updated [57–59].

For ammonia or hydrocarbon fuels, the oxidation process requires hundreds to thousands of elementary reactions to comprehensively describe the oxidation process under a wide range of temperatures, pressures and equivalence ratios. This complexity can be better understood if the oxidation is organized in a hierarchical structure, as described by Westbrook and Dryer [60]. For example, the H_2-O_2 mechanism serves as a core submechanism of the mechanism describing CO-H_2-O_2 oxidation. This CO-H_2-O_2 mechanism then becomes a subset of the CH_4 mechanism. The CH_4 mechanism is then incorporated into mechanisms for fuels, like ethane (C_2H_6) and ethanol (C_2H_5OH), having 2 carbon atoms. This hierarchical process can continue to C_3, C_4 and higher hydrocarbons. Details about the process of developing chemical kinetic mechanisms have been described by Kee et al. [51], Miller et al. [61] and Frenklach et al. [62].

One challenge in developing large mechanism is that when more species and reactions are incorporated, the reliability of such mechanism decreases due to the uncertainty in the rate constants of new reactions. Many rate constants of elementary reactions are either directly measured, for example in flow reactors [63], or calculated using quantum chemistry theory [63–66]. Measured rate constants for chemical mechanisms can have uncertainty within 30% [67], while those obtained from quantum chemistry calculation can vary by orders of magnitude. For example, in order to improve the ignition prediction of methanol, Klippenstein et al. [68] and Altarawneh et al. [69] both did theoretical calculations for the reaction of methanol (CH_3OH) with HO_2 radicals,

$$CH_3OH + HO_2 = CH_2OH + H_2O_2 \qquad (R1.12)$$

The rate constant of *R*1.12 calculated in these two studies varied by roughly an order of magnitude. Considering the uncertainties in the rates of the elementary reactions, it is important to test the predictions of chemical mechanisms over a wide range of conditions in various low-dimensional

combustion facilities, such as rapid compression machines, shock tubes, burner-stabilized flames, flow reactors and jet reactors.

To avoid overlooking potentially important elementary reactions in constructing new mechanisms, all possible relevant intermediates and reaction channels are included, leading to a, perhaps unnecessarily, large size of a mechanism. In practice, only a few of the many elementary reactions determine the rate of the overall oxidation process. *Sensitivity analysis* is a handy tool, which is used to identify the rate-limiting reactions at the specific conditions. The information obtained by sensitivity analysis can help to understand the oxidation process and discover important reactions that deserve a more precise evaluation of their rate constants.

The sensitivity analysis can be performed by varying each individual rate constant while keeping the others constant and computing the change in combustion property caused by the change in each rate constant. The sensitivity coefficient S_i is defined as:

$$S_i = \frac{(\Delta\tau/\tau)}{(\Delta k_i/k_i)} \tag{1.25}$$

where in this case $\Delta\tau$ is the change in ignition delay time, τ, upon changing rate constant of reaction k_i by Δk_i. One can also substitute S_L and ΔS_L, when performing the sensitivity analysis of burning velocity to the reaction mechanism. Usually, the rate constant is changed by increasing or decreasing the pre-exponential A factors in the Arrhenius equation.

Another tool is *flux analysis*, which determines the reaction path from reactants to products and provides an intuitive picture as to how different reactions contribute to the formation (or consumption) of the different chemical species. It can be obtained automatically from the software packages when solving the governing equations. An example of the oxidation of a methane/air mixture under conditions of autoignition (φ = 0.5, T_0 = 1000 K, P_0 = 60 bar), the reaction path that obtains at the time corresponding to 20% fuel consumption is shown in Fig. 1.8.

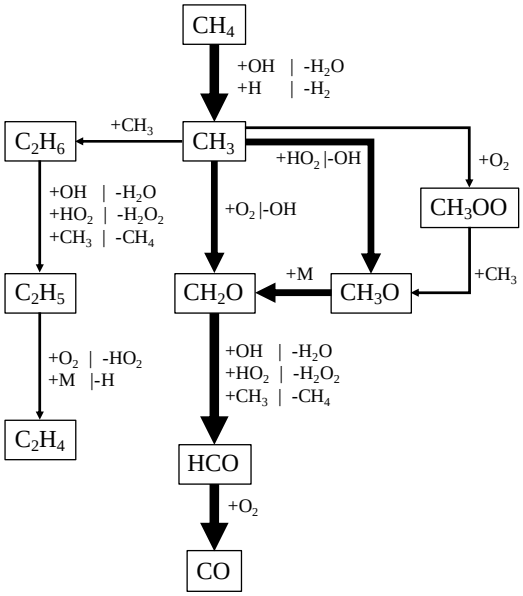

Figure 1.8. Flux analysis of methane oxidation in a homogeneous reactor at 20% fuel consumption at φ = 0.5, T_0 = 1000 K, P_0 = 60 bar, using mechanism from ref. [70].

In this case, methane oxidation starts from hydrogen abstraction reactions,

$$CH_4 + OH = CH_3 + H_2O \qquad (R1.13)$$

$$CH_4 + O = CH_3 + OH \qquad (R1.14)$$

$$CH_4 + H = CH_3 + H_2. \qquad (R1.15)$$

The methyl radicals (CH_3) produced are mainly converted into formaldehyde (CH_2O) through three channels: firstly through the intermediate CH_3O,

$$CH_3 + HO_2 = CH_3O + OH \qquad (R1.16)$$

$$CH_3O(+M) = CH_2O + H(+M) \qquad (R1.17)$$

secondly through the intermediate CH_3OO,

$$CH_3 + O_2 = CH_3OO \qquad (R1.18)$$

$$CH_3OO + CH_3 = CH_3O + CH_3O, \qquad (R1.19)$$

followed by dissociation, reaction *R*1.17,

and the third channel is directly oxidized by O_2,

$$CH_3 + O_2 = CH_2O + OH. \qquad (R1.20)$$

CH_2O is further attacked by radicals (OH, CH_3, CH_3OO, H, HO_2, O_2) forming the formyl radical (HCO). HCO is subsequently oxidized by O_2 producing CO.

Chapter 2: Experimental setups

2.1 Rapid compression machine

As discussed previously, autoignition properties of fuels are of great importance in combustion science. Many facilities have been designed to determine ignition delay times as function of temperature, pressure and compositions. Such facilities can be divided by the range of working conditions.

Flow reactor: A flow reactor usually is surrounded by external heating sources in order to provide a uniform temperature in the reaction zone. Fuel is injected into the air flow forming a premixed mixture and reaction takes place throughout the whole domain of reactor. Ignition occur at a certain location inside the reactor and depends on the flow rate of the mixture flow and temperature and pressure [71]. Flow reactor experiments have the advantage of being able to vary composition, pressure and temperature independently. However, flow reactors usually can only run at relatively low pressures (generally up to ~30 bar) and intermediate temperatures (up to ~1200 K) [51].

Shock tube: The reaction zone of a shock tube is occupied by highly diluted reactants at low pressure and is separated by a thin diaphragm from a region that contains an inert driver gas at high pressure, typically several bars. The reactants will be quickly compressed to high temperature (up to ~2500 K) and pressure (up to 80 bar) by incident and reflected shocks after the diaphragm is punctured [72]. A shock tube is ideal for measuring ignition delay times in the range from the order of microseconds to roughly 2 ms [73]. However, above ~1 ms [74], the conditions deviate from the constant volume, which require consideration in the interpretation and simulation of the results.

Rapid compression machine (RCM): An RCM resembles a single compression stroke of an internal combustion engine. The working condition of an RCM is usually in the range of temperature from ~ 550 K to ~1200 K and pressures from 5 bar to 80 bar, covering the working area of many combustion engines and partially overlaps with that of shock tubes [75]. The RCM allows measurement of ignition delay times over a wide range, from ~1 ms to ~100 ms. However, the conditions do not resemble a constant-volume reactor, and both the compression and ‘heat loss’ must be considered when

analyzing the results, similar to those for shock tubes at longer times (discussed below). Several RCMs have been developed worldwide, as reviewed by Goldsborough et al. [73]. The RCM used in this study is a replica of the MIT RCM [76] with improvements in the so-called fast acting valve [77]. More details of this RCM, described more completely in [77], will be discussed in next section.

2.1.1 Operation of the RCM

The schematic of the RCM used in this study is illustrated in Fig 2.1. It contains a T-type piston, with a 30 bar nitrogen driving chamber above the piston, which drives the piston in the combustion chamber. There are two main oil chambers, a speed-control oil chamber and an oil reservoir chamber, which are separated by a fast-acting valve. After a run, the piston is at the bottom of the stroke and the fast-acting valve is open, connecting the speed-control oil chamber and oil reservoir chamber. Referring to Fig. 2.1, to start a new run, the pressure in the combustion chamber is evacuated to ~0.7 mbar. The piston is then moved up to its maximum position by pressurizing the oil reservoir chamber with ~3 bar nitrogen. The fast-acting valve is first gently closed by ~7 bar nitrogen, followed by 70 bar oil pressure to isolate the speed-control oil chamber from the reservoir oil chamber. The piston is then locked at the top position by pressurizing the speed-control oil chamber with to ~ 48 bar. The 7 bar nitrogen and 3 bar nitrogen can be then both safely depressurized, because the piston and fast-acting valve have both been locked. In the next steps, the driving chamber is filled with 30 bar nitrogen and the combustion chamber is filled with unburned mixture. The experiment is started by opening the solenoid valve, releasing the 70 bar oil pressure on the fast-acting valve, and the fast-acting valve will be pushed up by the 48 bar oil pressure in the speed-control oil chamber. The rapid release of the oil pressure, with subsequent oil flow from the speed-control chamber into the oil reservoir, frees the piston and the 30 bar nitrogen pressure drives the piston down to compress the fuel-air mixture in the combustion chamber. The piston accelerates rapidly to a constant velocity; towards the end of the stroke, the velocity is slowed by a hydraulic damper [78] and arrives at the bottom plate without rebound. The piston is held firmly by the force of driving nitrogen, which is greater than the force of the compressed gas mixture in the reaction chamber. A creviced piston head is used in this RCM suppresses the roll-up

vortex during compression to obtain a homogenous reacting core during the experiment [76]. The piston speed can be controlled by varying the pressure in the driving chamber. To cover a wide range of compression ratios, the rapid compression machine was designed with an adjustable piston stroke, which be varied by turning the stroke adjustment screw. The clearance height, the distance between the end of the piston and the bottom wall of the combustion chamber, which determines the volume of the combustion chamber, can be changed by replacing the clearance ring in the combustion chamber (not shown in the figure).

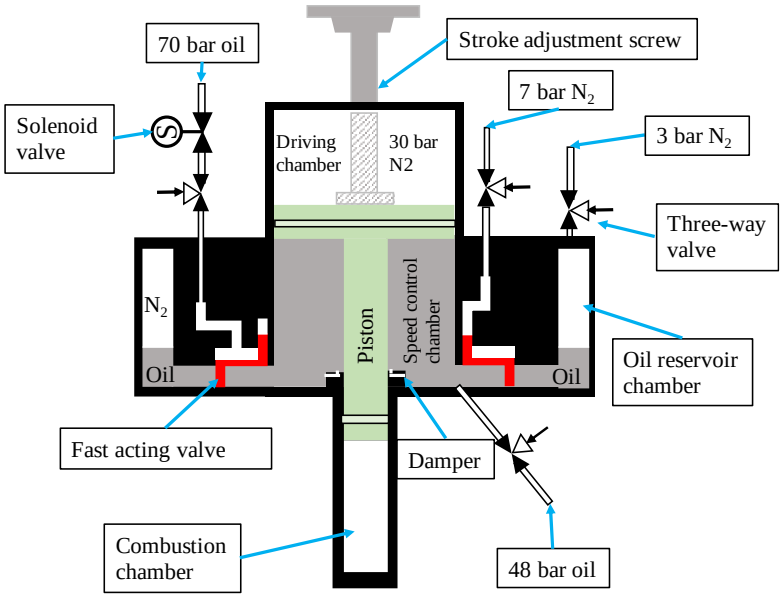

Figure 2.1 Schematic of the RCM.

2.1.2 Gas handling system and data acquisition

The gas handling system of the RCM is shown in Fig 2.2. The composition of the unburned gas mixture is calculated from the measured partial pressures of the individual gases when introduced into the 10-liter mixture tank. The tank and gas lines are evacuated to less than 0.5 mbar using a vacuum pump before preparing the gas mixture. After filling the tank with an individual component, the tank is closed and the gas lines are evacuated before filling with the next component. The gas mixture is allowed to mix in

the tank for at least 24 hours to ensure homogeneity. Before each ignition measurement, the poppet valve and the solenoid valve in Fig. 2.2 are opened, and the whole system is evacuated to a pressure below 0.7 mbar. Then the combustion chamber is filled with the gas mixture from the mixture tank to the desired initial pressure. The poppet valve is then closed and the mixture is ready for compression. After each run, the compressed gases in the RCM are first vented to the outside air and the chamber is evacuated again before preparing the next run. The solenoid valve in the gas-filling line is included for safety purposes. When the solenoid valve used to trigger the fast-acting valve is open, the solenoid in the gas-filling line is always closed. This prevents flame propagation back to the gas-mixture bottle if the poppet valve is not properly closed.

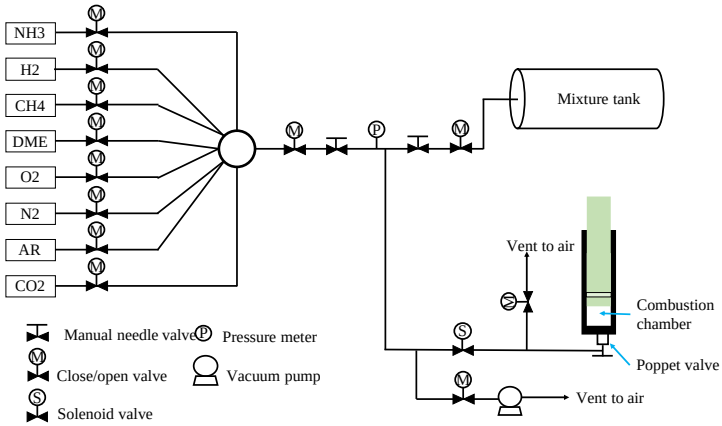

Figure 2.2 Gas handling system of RCM.

A DPI pressure gauge (type 800P) with an operating range from 0 - 3000 mbar with an accuracy of 0.5% of reading is used for measuring all partial pressures of the components when filling the tank and all other pressures in the gas lines. A Pt-Rh thermocouple with an accuracy of ± 0.2K was installed in the wall of the combustion chamber to measure the initial temperature of the mixture. A Kistler ThermoComp quartz sensor (range 1-250 bar, linearity ± 0.1%) with thermal-shock-optimized construction is installed in the bottom of the combustion chamber to monitor the pressure traces in the combustion chamber during compression and throughout the post-compression period. The signal from the transducer was amplified by a 5010B Kistler charge amplifier, recorded digitally by an oscilloscope with a sample rate of 500 kHz

and 16-bit resolution, and processed by a PC. The data acquisition was triggered simultaneously with the opening of the solenoid for the fast-acting valve.

The compression temperature T_c can be calculated with measured T_0, P_0 and P_c, using equation

$$\int_{T_0}^{T_c} \frac{\gamma(T)}{\gamma(T)-1}\frac{dT}{T} = \ln\left(\frac{P_c}{P_0}\right), \tag{2.1}$$

which is derived from Eq. (1.9) by considering it as particular case when chemical producing term can be neglected and the term of heat loss q_{loss} is zero due to adiabatic compression.

2.1.3 Determination of ignition delay time and numerical simulations

A typical measured pressure trace is shown in Fig 2.3. The total compression process takes around 10-20 ms and 80% of the total compression occurs in less than 3 ms to limit substantial heat losses and radical build up before the end of the compression. After compression, the pressure decreases due to heat loss, while the chemical reactions leading to ignition occur. The ignition delay time (τ) is defined as the time interval between the end of compression and the maximum in the rate of pressure increase during ignition, as shown in Fig. 2.3(a). There are fuels (such as DME [37]and some heavier hydrocarbons [79,80]) that have two or multiple-stage heat release. In the case of two-stage ignition, as shown in Fig. 2.3(b), the total ignition delay time (τ) has the same definition of single stage ignition while the first stage ignition (τ_1) is defined as the interval between the end of compression and the point of maximum pressure rise during the first stage of heat release. The ignition delay times for the conditions in the RCM were simulated using the homogenous reactor code from the Cantera package [47] as discussed in Section 1.3.2. To account for changes in the mixture conditions during compression and post-compression heat loss, the specific volume trace as a function of time was used as an input in the simulations by applying the adiabatic core assumption [81]. The rationale behind the approach is that, as the near-wall boundary layer cools during the post-compression period, the core gas away from the boundary layer experiences an effective volumetric expansion even though the geometric volume of the reaction chamber remains

the same after reaching the end of compression. In addition, when the roll-up vortex is effectively suppressed by using a creviced piston, the effect of heat loss on the core gas occurs only through this expansion [75]. The specific volume was derived from the measured pressure trace of a non-reactive gas mixture that had the same average heat capacity as the combustible mixture. The importance of using a mixture having the average heat capacity for the measured non-reactive trace will be discussed below in Chapter 3, while a potential limitation of this method is discussed in Chapter 5.

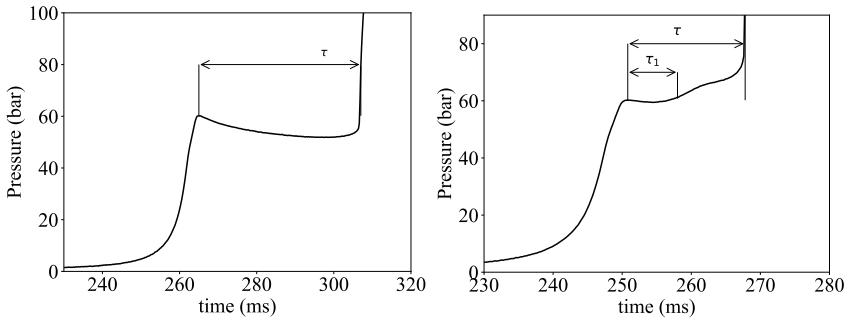

Figure 2.3. Typical measured pressure traces, (a) single stage ignition of ammonia, (b) two stage ignition in ammonia/DME mixture.

2.2 Flat-flame burner

2.2.1 Burner schematic

The laminar premixed flame experiments presented in this thesis were performed on a commercially available flat-flame burner from McKenna Products. A schematic of this burner is illustrated in Fig. 2.4. As can be seen, the core part of this burner is a porous sintered plate (6 cm diameter) made of bronze which contains a spiral cooling circuit for water. The radial temperature gradient vanishes in the burner plate due to fast heat transfer and evenly distributed cooling circuit. The water-cooled porous plate is pressed into a stainless-steel housing which is then screwed into the stainless steel main-body. Unburned mixture flows into the cavity located below the sintered plate within the housing and then goes through the burner plate evenly. A bronze shroud ring is fitted into the main-body surrounding the top part of housing. Inert gas (usually nitrogen) is introduced through the shroud to

isolate the flame from environment. The porous plate design ensures a homogeneous flow rate of unburned mixtures and prevents flashback from the flame propagation towards unburned mixture. The burner is affixed on a digitally controlled positioner that can move the burner in three dimensions with a precision of 0.1cm. A cylindrical chimney with a 6 cm inner diameter was centrally positioned approximately 5 cm above the burner surface to stabilize the post-flame gases.

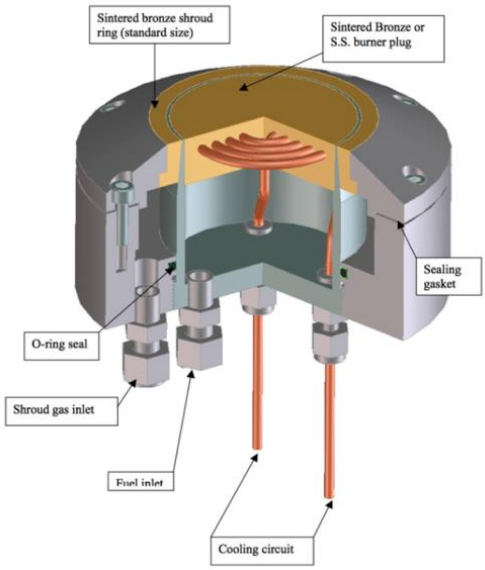

Figure 2.4. Overview of the McKenna Flat Flame Burner [12], reprinted from www.flatflame.com, reprinted with permission.

2.2.2 Gas handling system for the burner

The schematic of the gas handling system used to provide required the composition of the unburned mixture is shown in Fig. 2.5. Compressed air was used as oxidizer, taking the air to consist of 20.95% O_2 and 79.05% N_2. Fuel and air were premixed homogenously in the mixing tube before going to the burner. The reproducibility of flames relies on the accurate measurement of flow rate and equivalence ratio (φ) of unburned mixtures. For this purpose, flow rates of all cold gases were measured by calibrated Bronkhorst flow meters with different full-scale ranges, having accuracy better than 3% full scale. The exit velocity of the unburned gas mixture can be determined from the flow rates,

$$v = \frac{Q_{air} + Q_{fuel}}{\pi r^2}, \tag{2.2}$$

where Q_{air} and Q_{fuel} are the flow rates of air and fuel with units in liter/s, respectively, and r is the radius of burner surface, that is, 3 cm in this study. The equivalence ratio can be derived from measured Q_{air} and Q_{fuel} using Eq. (1.1). Alternatively, instead of measuring Q_{air} and Q_{fuel}, the equivalence ratio can be determined by measuring the oxygen concentration in the fuel/air mixtures using Maihak S710 gas analyzer.

$$[O_2] = \frac{Q_{O2}}{Q_{air} + Q_{fuel}} = \frac{0.2095 * Q_{air}}{Q_{air} + Q_{fuel}} \tag{2.3}$$

where $[O_2]$ is measured O_2 concentration from Maihak S 710 extractive gas analyzer, Q_{O2} is the flow rate of O_2, which is 20.95% of the air flow rate Q_{air}. Equation (2.3) can be rewritten as

$$[O_2] = \frac{Q_{O2}}{Q_{air} + Q_{fuel}} = \frac{0.2095}{1 + \frac{Q_{fuel}}{Q_{air}}}. \tag{2.4}$$

The ratio between fuel flow rate and air follow rate is represented by a function of oxygen concentration,

$$\frac{Q_{fuel}}{Q_{air}} = \frac{0.2095}{[O_2]} - 1 \tag{2.5}$$

Thus, combining Eq. (1.1) and (2.5), equivalence ratio is obtained

$$\varphi = \frac{Q_{fuel}}{Q_{air}} / f_{stoi} = (\frac{0.2095}{[O_2]} - 1) / f_{stoi}. \tag{2.6}$$

The equivalence ratio determined by measuring oxygen concentration has an accuracy of ~2 % [82].

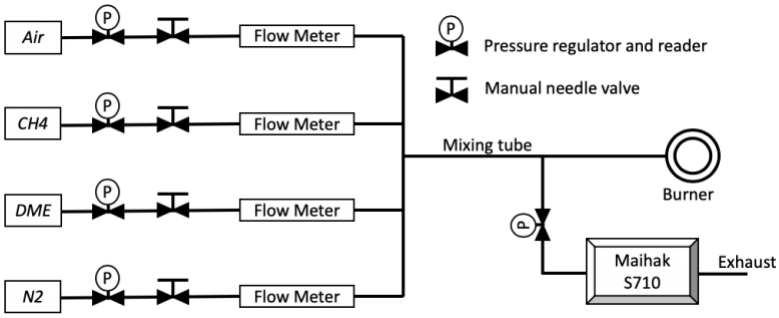

Figure 2.5. Schematic of gas handling system.

2.3 Flame temperature measurement using spontaneous Raman scattering

One of the objectives in this thesis is to measure the temperatures in 1-D premixed DME/air flames. Raman scattering has been widely used to measure temperature and major species concentration in flames, providing high spatial and temporal resolution. The results obtained from laser diagnostics are non-invasive, which is important when studying chemically reacting flows.

2.3.1 Theory of spontaneous Raman scattering

When a single laser beam with frequency (ν_0) goes through a gas medium, if there is no energy exchange between the incident photons from the laser and the molecules or particles being studied, it is called an elastic scattering process. The elastic scattering of light quanta from molecules have the same energy (frequency) as the incident photon, leading to *Rayleigh scattering*. On the other hand, in Raman scattering, inelastic scattering occurs when some of the energy from photons is transferred to the molecules, or vice versa, causing a transition of the molecule from its initial state to some other state. The inelastically scattered photons have different frequency from the incident photons. The shift in frequency is associated with the difference in energy between the different molecular states. In the molecules considered here, the transitions are among vibrational and rotational levels. The transition of a molecule from the initial level to a level with a higher energy is called *Stokes Raman scattering* and transition from a higher level to a lower level is called *anti-Stokes Raman scattering*. An illustration of the scattering process is shown in Fig. 2.6. In this work, spontaneous Stokes Raman scattering was chosen to study DME/air flames.

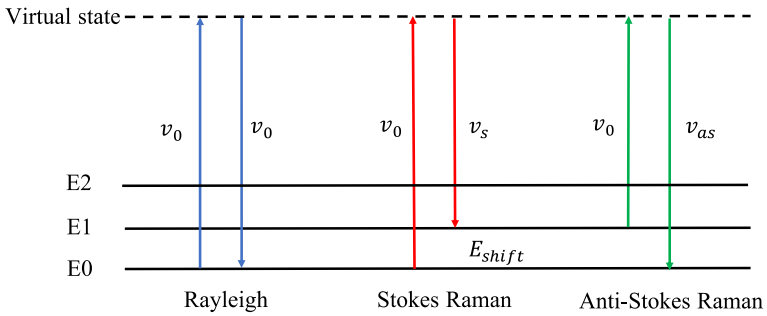

Figure 2.6. Vibrational Rayleigh, Stokes and anti-Stokes Raman scattering.

The quantization of the molecular energy state distribution follows Boltzmann distribution [83],

$$P_m = \frac{g_m \times e^{-E_m/kT}}{Z_m(T)}, \tag{2.7}$$

where P_m is the probability of a molecule being in the *m*th state having energy E_m, g_m is the degeneracy of the mth state, indicating the number of molecules which can occupy any given energy state, *k* is Boltzmann's constant; $Z_m(T)$ is the molecular partition function, given as

$$Z_m(T) = \sum_m g_m \times e^{-E_m/kT}. \tag{2.8}$$

Since the energy states of molecules are quantized, the Raman spectrum has fixed frequency separations from laser line, which is characteristic for the molecule under study [83]. Since different molecules have different spectra, the composition of a gas mixture (like the composition of a flame) can be analyzed using Raman scattering.

2.3.2 Layout of laser system and temperature determination

The optical setup and operation of spontaneous Raman scattering used in this study was described in [84] and is shown in Fig. 2.7. A Nd:YLF laser (Spectra Physics Empower, 5 kHz repetition rate, 400 ns pulse duration, average power 30 W, wavelength 527 nm) is used as excitation source. The laser beam passes through a beam shutter and polarizer and then focus above

the center of the burner by a focus lens with f = 500 mm. After passing through the flame, the laser beam is trapped in a beam dump. The scattering signal is collected perpendicular to the beam by an f/2.8 lens with a focal length of 300 mm. The signal is projected onto the entrance slit of the spectrometer, which is parallel to the laser beam. The signal is dispersed by the spectrometer (Acton Research Sepctra-Pro, f/4. 150 mm, 5nm/mm dispersion) with magnification factor of 0.5. At the exit plane of spectrometer, an intensified CCD camera (PI-MAX, Princeton Instruments, 1024 x 1024 pixels, 13 µm pixel size) was mounted for collecting the spectral distribution. The full range of horizontal pixels on the senor of CCD chip is used, binning them in pairs. Vertical pixels 301-700 are binned in one group, enabling an integration of the signal over the sample distance of ~10 mm along the laser beam. The sensor is cooled to -40 ℃ to limit dark current. The data collection, storage and processing were performed using WinSpec 32 (Princeton Instruments) software.

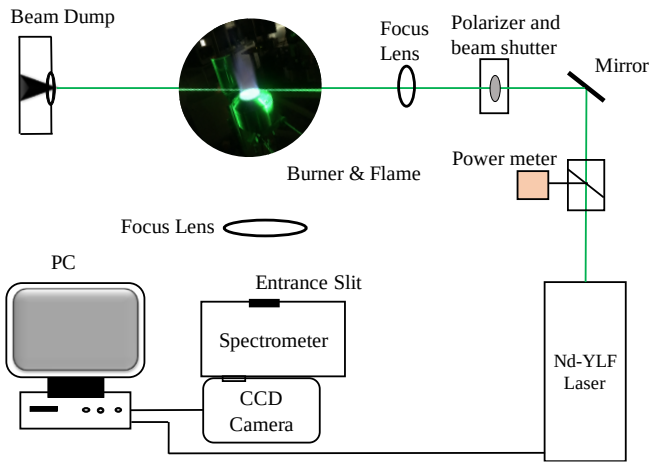

Figure 2.7 Schematic for the Raman experimental setup.

In all experiments, the CCD camera was used in 'gate' mode [84]; the detection of a signal will start only when the laser pulse arrived at the measuring location in order to minimize the effect of background signals on the scattered signal. Due to the low cross section for Raman scattering [83], accumulation of the scattering signal from many laser pulses are necessary to record a high-quality spectra. The exposure time for the signal acquisition by

the CCD camera in the experiment was set at 2 min (20 accumulations for a spectra). Further extension of exposure time did not improve the quality of the Raman spectra significantly. The spectra are always measured twice, first with the laser beam polarized perpendicular to the scattering plane and then with parallel polarization by turning the polarizer 45 degrees. Since the background signal is unpolarized, the signal/noise ratio can be significantly increased by subtracting the signal measured with parallel incident radiation from the signal with perpendicular incident radiation [84]. An example of Raman spectra for different gases measured at room temperature is shown in Fig. 2.8.

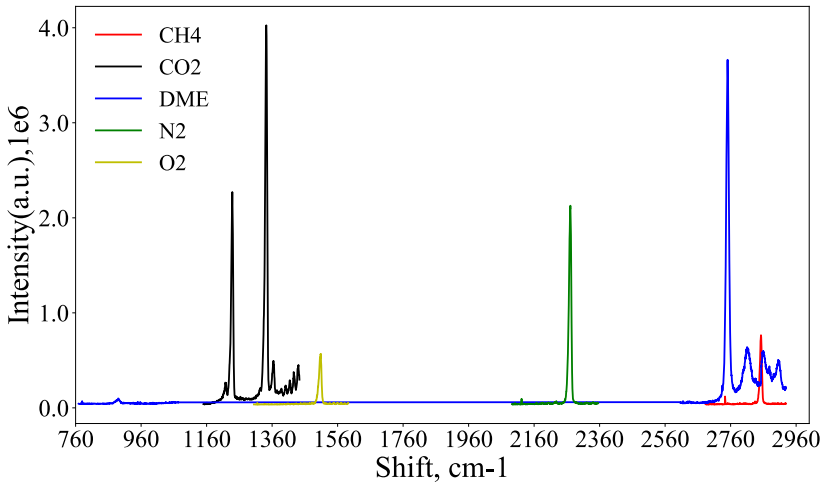

Figure 2.8. Raman spectra of methane, CO_2, DME, N_2 and O_2 measured pure gases at room temperature.

The flame temperature was derived by fitting the measured Raman spectra from nitrogen (N_2). An inhouse program to fit the Raman spectra has been described in ref. [84,85]. A typical N_2 Raman spectrum in the DME/air flame at φ = 1.2, v = 25 cm/s, at 1.0 cm height above the burner (HAB) is shown in Figure 2.9. The fitting procedure for this flame yields T = 1967 K. Vertical temperature profiles were measured over a range of ~ 2 cm from the initial position at HAB = 2 mm by moving the burner in 2 mm steps both down and up, providing two profiles for the same experimental condition. The differences in derived temperatures were less than 20 K, indicating the short-term reproducibility (regarding flame conditions and positioning) of our measurements. The day-to-day reproducibility was generally better than ±20 K, obtained by repeated measurements on different days.

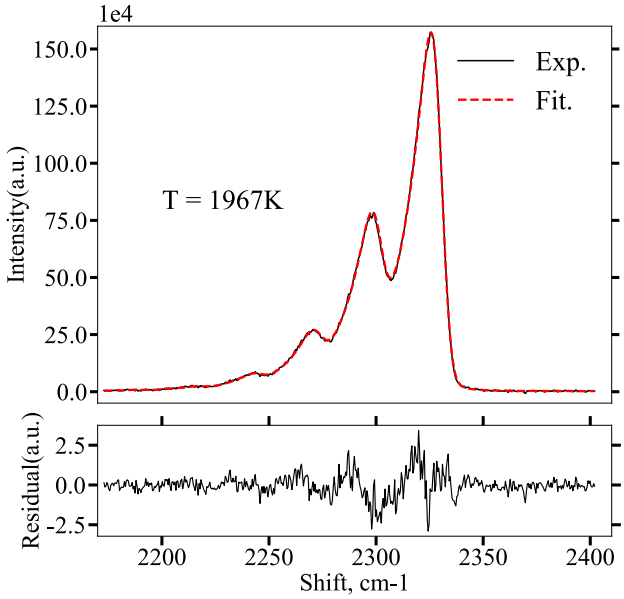

Figure 2.9. Measured and fit N_2 Raman spectrum in DME/air flame at φ = 1.2, v = 25 cm/s, HAB = 1cm. Above, measured and fit spectrum; below the difference between measured and fit.

Chapter 3: Experimental and numerical analysis of the autoignition behavior of NH_3 and NH_3/H_2 mixtures at high pressure

This chapter is based on the work presented in: L. Dai, S. Gersen, P. Glarborg, H. Levinsky, A. Mokhov. Experimental and numerical analysis of the autoignition behavior of NH_3 and NH_3/H_2 mixtures at high pressure. Combust Flame 2020;215:134–44

3.1 Experimental conditions and mechanism details

To gain more insight in the autoignition behavior of NH_3 and NH_3/H_2 mixtures at conditions relevant to practical engines, as well as to provide additional benchmark data for mechanism verification, this chapter reports measurements of the ignition delay times of NH_3 and NH_3/H_2 mixtures in an RCM at equivalence ratios varying from 0.5 to 3.0, pressures from 20-75 bar, and temperatures in the range 1040-1210 K. The measurements of pure ammonia at pressures above 40 bar and at φ = 2.0 and 3.0 reported here are a significant extension of the test of the chemical mechanism in comparison with previous reports. The hydrogen fraction was varied in the range 0-10%. the measurements were compared with calculations using a modified version of the mechanism of Glarborg et al. [30], as well as with the mechanisms of Klippenstein et al. [31], Mathieu and Petersen [22], and Shrestha et al. [86]. A kinetic analysis was performed to examine NH_3 oxidation under these conditions and the influence of H_2 addition on the ignition process. The compositions (in mole fraction) of the mixtures examined in this chapter are shown in Table 3.1.

Table 3.1. Compositions of NH_3 and NH_3/H_2 mixtures studied in this work

Mixtures	φ	H_2/fuel	NH_3	H_2	O_2	N_2	Ar
Mixture 1	0.5	0	0.118	0	0.176	0	0.706
Mixture 2	0.5	0	0.1	0	0.15	0.1	0.65
Mixture 3	1.0	0	0.143	0	0.107	0	0.75
Mixture 4	2.0	0	0.182	0	0.068	0	0.75
Mixture 5	3.0	0	0.16	0	0.04	0	0.8
Mixture 6	0.5	5%	0.113	0.006	0.176	0	0.705
Mixture 7	0.5	10%	0.109	0.012	0.176	0.141	0.562
Mixture 8	1.0	5%	0.138	0.007	0.107	0.037	0.711

An example of measured ignition pressure trace is illustrated in Fig. 3.1. The day-to-day reproducibility of the measurements, including repositioning of the piston height, was determined to be better than 5%. The uncertainty of the calculated core gas temperature (T_c) is less than ± 3.5 K for all measurements [77]. It's necessary to point out that the pre-ignition pressure

rise reported in [24] was not observed in any of the experiments reported for these mixtures.

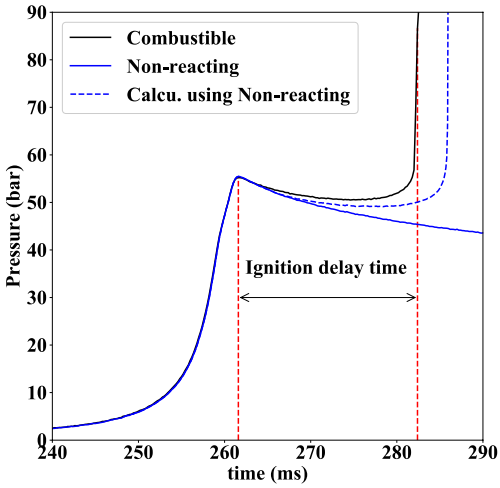

Figure 3.1. Example of pressure profiles. Measured combustible mixture (black line) and non-reactive mixture (blue solid line) pressure trace and calculation (blue dashed line) based on non-reactive gas for mixture 1 at T_c = 1080 K, P_c = 55 bar.

The reaction mechanism was drawn largely from the recent review by Glarborg et al. [30]. The H/N/O subset of their mechanism was based on the work by Klippenstein et al. [31], but rate constants for selected key reactions were updated. The amine subset of the kinetic model was intended to describe fuel-N oxidation in combustion, as well as selective non-catalytic reduction of NO with NH_3 (Thermal DeNO$_x$), but the mechanism was not evaluated for ammonia ignition under the high-pressure conditions reported here.

The shock tube work of Mathieu and Petersen [22], conducted at pressures up to 30 bar, indicated that inclusion of an N_2-amine subset involving N_2H_4, following Klippenstein et al. [31], had a detrimental impact on modeling predictions. In the present work, the rate coefficients for the reaction forming hydrazine, $NH_2 + NH_2 (+M) = N_2H_4 (+M)$ (R3.1), were re-evaluated; this re-evaluation was performed by P. Glarborg and is included here for completeness. Both Glarborg et al. [30] and Klippenstein et al. [31] relied on the theoretical work of Klippenstein et al. [87], which was in good agreement with the low temperature measurements of the reaction [88–92]. At elevated temperature, the reaction has been studied over a wide range of pressure in shock tubes. Diesen [93] and Meyer et al. [94] report data, presumably at the low-pressure limit. Kinetic modeling of the experiments of

Diesen [93] indicates that $k_{1b,0}$ is roughly 1/3 of the observed disappearance rate for N_2H_4, since both the amino radicals formed in the dissociation act to remove hydrazine. The rate constant reported by Diesen [93] has thus been reduced by a factor of three. Similarly, the rate constants reported by Meyer et al. [94] were multiplied by a factor of 2/3. Figure 3.2 compares data for the low-pressure limit of R 3.1; i.e., the low temperature experimental data of Khe et al. [88] and Altinay and Macdonald [92], the theoretical value by Klippenstein et al. [87], and data derived from low-pressure measurements of the reverse rate constant by Diesen [93] and Meyer et al. [94], converted through the equilibrium constant.

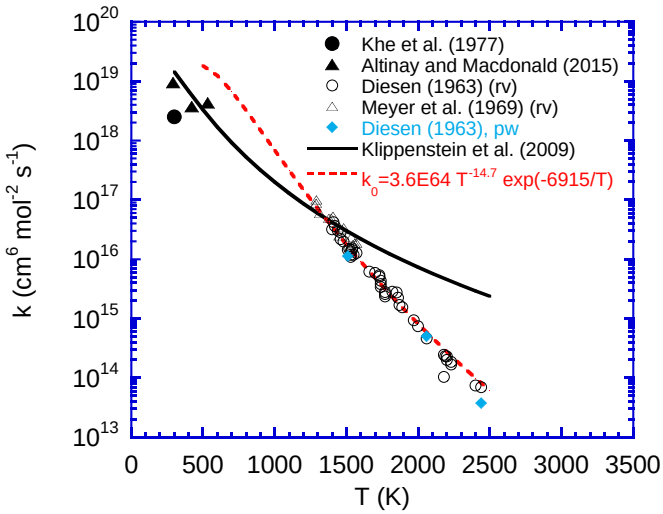

Figure 3.2. Data for the low pressure limit $k_{1b,0}$ of the $NH_2 + NH_2$ (+M) = N_2H_4 (+M) reaction (R 3.1). Symbols denote the experimental data of Khe et al. [88] and Altinay and Macdonald [92] for the forward reaction, and data derived from low-pressure measurements of the reverse rate constant by Diesen [93] and Meyer et al. [94], converted through the equilibrium constant. The solid line shows the theoretical value by Klippenstein et al. [87], while the short-dashed line shows a fit to $k_{1b,0}$, obtained in the present work.

The data in Fig. 3.2 indicate that the low pressure limit by Klippenstein et al. [87] agree well with the low temperature data for the forward reaction and also with results for R1b at around 1500 K, but at higher temperatures the value from Klippenstein et al. appears to overpredict the recombination rate. Fig. 3.3 shows results obtained at high pressure, presumably at the high pressure limit. Data for the forward reaction, obtained at low temperature by Khe et al. [88], Lozovskii et al. [89], Sarkisov et al. [90] and Fagerstrom et al. [91] are scattered, varying almost an order of magnitude. The results derived

from the high temperature measurements by Meyer et al. [94] and Genich et al. [95] are in good agreement, but indicate a high pressure limit somewhat smaller than calculated by Klippenstein et al. [87].

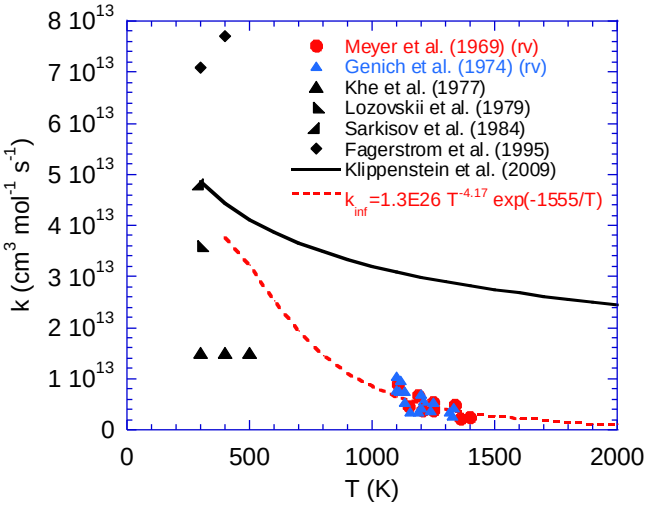

Figure 3.3. Data for the high pressure limit $k_{1b,inf}$ of the NH_2 + NH_2 (+M) = N_2H_4 (+M) reaction (R 3.1). Symbols denote the experimental data of Khe et al. [88], Lozovskii et al. [89], Sarkisov et al. [90] and Fagerstrom et al. [91] for the forward reaction, and data derived from high-pressure measurements of the reverse rate constant by Meyer et al. [94] and Genich et al. [95], converted through the equilibrium constant. The solid line shows the theoretical value by Klippenstein et al. [87], while the short-dashed line shows a fit to $k_{1b,inf}$, obtained for use in the present work.

The reason for the discrepancy between the theoretical rate coefficients for NH_2 + NH_2 (+M) = N_2H_4 (+M) and the shock tube measurements of the reverse step is not known at present. The heat of formation of N_2H_4 has been in question, but the current value [30] is in excellent agreement with the recent recommendations by Dorofeeva et al. [96] and Feller et al. [97]. It is an issue whether the experimental data are truly obtained at the low and high pressure limits, respectively, but more work is required to resolve this issue. Under the conditions of the present work, the modification of the rate constant for R1 turns out to have only a limited impact on ignition delay predictions and calculations with the mechanism of Glarborg et al. [30] are largely within 10% of those using the modified mechanism; consequently, only the latter are shown.

3.2 Results and discussion

3.2.1 Pure NH_3 mixtures

The ignition delay times of pure NH_3 measured at φ = 0.5, 1.0 and 2.0 are shown in Fig. 3.4. As can be seen, the ignition delay times decrease with increasing temperature and pressure at all equivalence ratios. The data for isobars and isotherms indicate a significant increase in ignition delay time with equivalence ratio, by a factor of two when going from 0.5 to 1 and from 1 to 2. The substantial differences in measured ignition delay times for equivalence ratios 0.5 and 1.0 reported here were not observed in [24]. However, the interpretation of this functional dependence for practical devices is complicated by the change in $(Ar+N_2)/O_2$ ratio that was necessary to reach the ignition temperatures under these condition of pressure, as is often done in ignition studies (see, for example, [22,24,98]). The possible impact of the changes in inert/oxygen ratio is considered below.

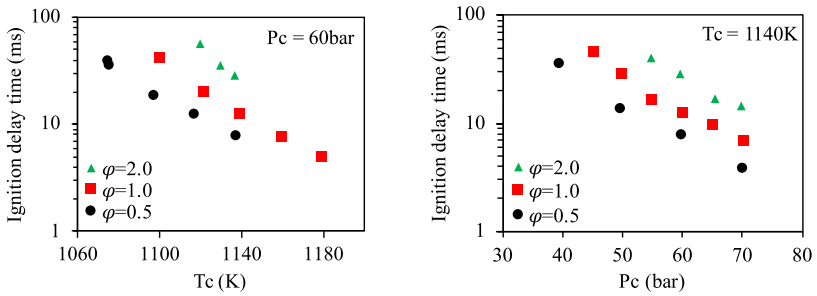

Figure 3.4. Effect of equivalence ratio on ignition delay time for pure NH_3 at φ = 0.5 (mixture 2), 1.0 and 2.0. (a) measurements varying T_c at constant P_c (isobars), (b) measurements varying P_c at constant T_c (isotherms). Note: the error bars of ignition delay times (±5%) are covered by the symbols and are thus not visible in the figures.

The measured ignition delay times of pure NH_3 were used to evaluate the performance of the four mechanisms referred to above at φ = 0.5, 1.0, 2.0 and 3.0, as shown in Fig. 3.5. The mechanism from the present study, drawn from Glarborg et al. [30] with the modification described in Section 3.1, predicts the ignition delay times well at all conditions, with a maximum deviation less than 30%. The agreement under lean conditions marks a departure from the results in He et al. [24], who noted a significant underprediction, more than a factor of 2, with the mechanism from [30]; as noted above, the differences

between the mechanism in [30] and that used here do not account for this discrepancy (see below). The model from Shrestha et al. [86] shows underprediction for all conditions, by factors of ~1.5, 2, 2 and 3 at φ = 0.5, 1.0, 2.0 and 3.0, respectively. The Mathieu and Petersen mechanism [22] yields good predictions at φ = 0.5 (again in contrast with [24]) and 1.0, with deviation less than 20%; however, it overpredicts the ignition delay times by a factor of ~2 at φ = 2.0 and 3.0. The model from Klippenstein et al. [31] overpredicts the ignition delay times by more than a factor of 2 at φ = 0.5, and 2.0. However, at φ = 1.0 and 3.0, good agreement is obtained only at high temperatures, while at lower temperature the ignition delay is overpredicted by up to a factor of 5. The overprediction reported here is in agreement with the observations in [24].

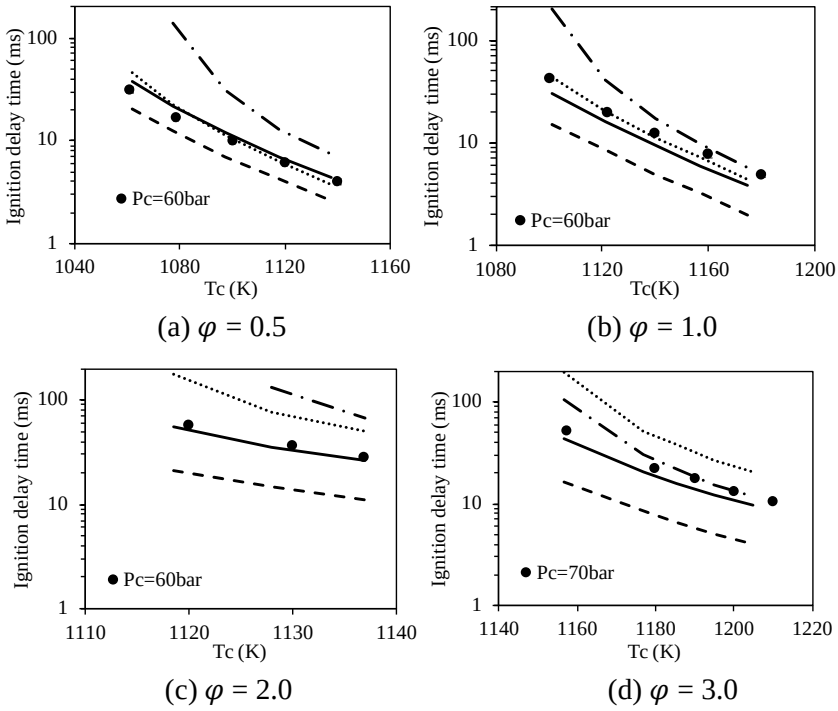

Figure 3.5. Measured (points) and calculated (lines) ignition delay times of NH_3 as function of temperature at φ = 0.5 (mixture 1), 1.0, 2.0 and 3.0. Solid lines: the mechanism presented here, dashed lines: the Shrestha et al. mechanism [86], dotted lines: the Mathieu and Petersen mechanism [22], and dash-dot lines: the Klippenstein et al. mechanism [31]. (The small apparent mismatches in temperature between some experimental and calculated data arise from slight differences in temperature between the reactive and non-reactive experiments.)

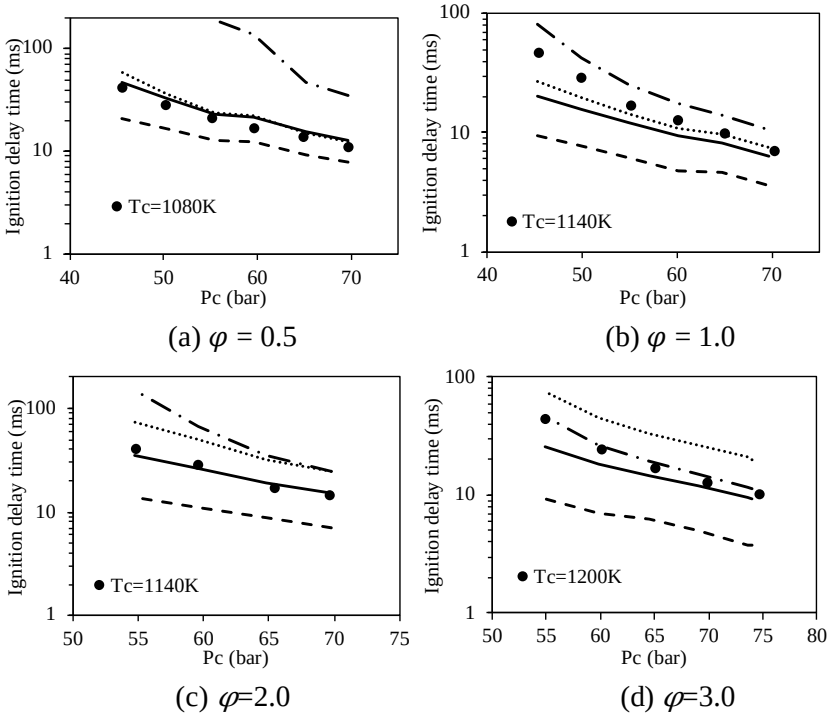

Figure 3.6. Measured (points) and calculated (lines) ignition delay times of NH_3 as function of pressure at φ = 0.5 (mixture 1), 1.0, 2.0 and 3.0. Solid lines: the mechanism in this work, dashed lines: the Shrestha et al. mechanism [86], dotted lines: the Mathieu and Petersen mechanism [22] and dash-dot lines: the Klippenstein et al. mechanism [31].

Figure 3.6 illustrates the measured ignition delay times as a function of pressure at φ = 0.5, 1.0, 2.0 and 3.0, at fixed T_c = 1080 K, 1140 K, 1140 K and 1200 K, respectively. As noted above, the ignition delay time decreases with increasing P_c at all four equivalence ratios. The present mechanism predicts the ignition delay times very well at φ = 0.5 and 2.0, with deviations below 25%. However, at φ = 1.0 and 3.0, good agreement is obtained only at high pressures, while at lower pressure the ignition delay is underpredicted by up to 60%. The Shrestha et al. [86] mechanism again shows underprediction by more than a factor of 2 at all conditions. Mathieu and Petersen's mechanism [22] yields similar predictions as the present model at φ = 0.5 and 1.0, but overpredicts the ignition delay times by a factor of ~2 at φ = 2.0 and 3.0. The model from Klippenstein et al. [31] shows overprediction by a factor larger than 2 at φ = 0.5, 1.0 and 2.0, whereas it predicts ignition delay times very well at φ = 3.0. In general, the present mechanism, based on Glarborg et

al. [30], has the best performance in predicting ignition delay times of pure NH_3 in the range of equivalence ratio φ = 0.5-3.0 for the pressures and temperatures used here.

Given the agreement between the experiments and the simulations using the current mechanism, the computations can be used to disentangle the effects of varying inert/O2 ratio from those of the change in equivalence ratio mentioned above. The equivalent data for Fig. 3.4a is shown in Fig. 3.7, but using a constant Ar/O_2 ratio of 5. These results show that, while the effect of inert/O_2 ratio seen in Fig. 3.4 is substantial, the ignition delay time for ammonia increases with equivalence ratio, in contrast with the ignition of many hydrocarbons (see, for example, [76,79]).

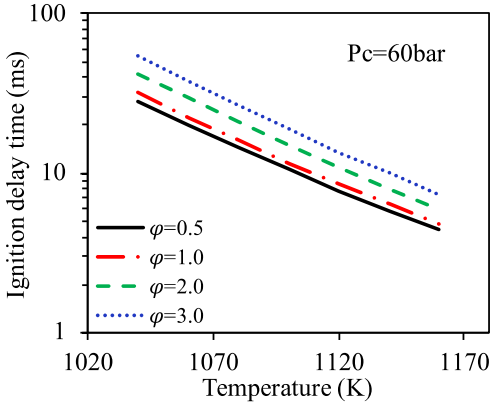

Figure 3.7. Calculated ignition delay times of pure NH_3 using the mechanism presented here at a constant Ar/O_2 ratio of 5.

3.2.2 NH_3/H_2 mixtures

Experiments with three NH_3/H_2 mixtures (5% and 10% H_2 addition at φ = 0.5 and 5% H_2 addition at φ = 1.0, see Table 3.1) were conducted to characterize the impact of H_2 on the ignition delay and to further evaluate the performance of the mechanisms. As reported by others [24], Fig. 3.8 shows a significant ignition-enhancing effect of H_2. At φ = 0.5, the ignition delay times of both isobars (Fig. 3.8a) and isotherms (Fig. 3.8b) are reduced by a factor of ~12 when H_2 addition increases from 0 to 5% of the fuel mixture, and by an additional factor of ~2 when increasing the H_2 fraction from 5% to 10%. At φ = 1.0, 5% H_2 addition to NH_3 leads to a reduction of the ignition delay times by a factor of ~28, indicating that the ignition-enhancing effect of

H_2 addition is more pronounced at higher φ. The NH_3/H_2 measurements were extended to P_c = 40 and 20 bar, as shown Figs. 3.8b and 3.9. For all three mixtures, the ignition delay times decrease with increasing pressures. At φ = 0.5 (Fig. 3.8b and 3.9a/b) for both 5% and 10% H_2 addition, increase of P_c from 20 bar to 40 bar and from 40 bar to 60 bar leads to reduction of the ignition delay times by factors of ~4.5 and ~2.5, respectively. A similar trend is found at φ =1.0 (Fig. 3.9c), again with a factor of ~2.5 between P_c = 40 and 60 bar, but with a larger factor, of ~6, between P_c = 20 and 40 bar.

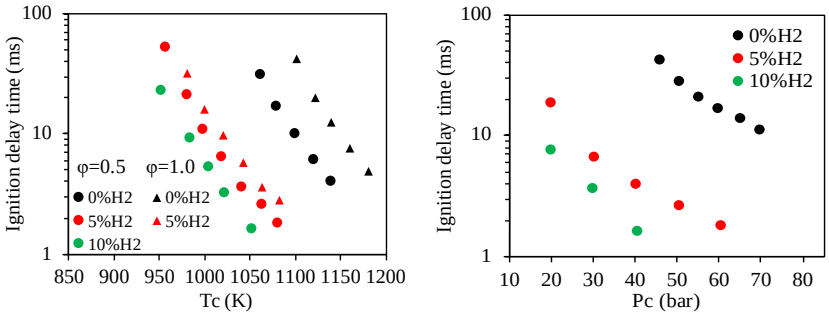

(a) φ = 0.5 and 1.0, P_c = 60 bar (b) φ = 0.5, T_c = 1080 K

Figure 3.8. Effect of H_2 addition on the ignition delay times at φ = 0.5 (circles) and φ =1.0 (triangles). (a) isobars, (b) isotherms.

The agreement of the calculations using the present mechanism with the measurements for the isobars at P_c = 40 bar and 60 bar, is generally within 30%. At P_c = 20 bar, an underprediction by a factor ~2 is observed for both hydrogen fractions at φ = 0.5 (Figs. 3.9a and b) and by a factor of 4.5 for 5% H_2 at φ = 1.0. The Shrestha et al. mechanism [86] underpredicts the ignition delay times by a factor of ~2.5 for isobars at P_c = 40 and 60 bar and by a factor of ~10 at P_c = 20 bar for all three H_2-containing mixtures. Predictions with the model from Mathieu and Petersen [22] are close to those using the mechanism of the present study. The Klippenstein et al. mechanism [31] yields an overprediction by a factor ~2 for isobars at φ = 0.5, P_c = 40 and 60 bar, whereas the deviation for the isobars at P_c = 20 bar is less than 40%.

At φ = 1.0, this mechanism predicts ignition delay times within ~20% for isobars at P_c = 40 and 60 bar, while an underprediction by a factor ~3 is observed at P_c = 20 bar. Overall, for the NH_3/H_2 mixtures studied in this work, the present mechanism and that of Mathieu and Petersen [22] show the best performance at high pressure (P_c = 40 and 60 bar), while the Klippenstein et

al. mechanism [31] yields better results at low pressures (P_c = 20 bar). The mechanism from Shrestha et al. [86] tends to underpredict ignition delay times at all conditions. While the simulation results under similar conditions as reported in [24] show close agreement between the mechanisms of Glarborg et al. [30] and Mathieu and Petersen [22] for all mixtures studied, they do not observe the good agreement for these mechanisms with the experimental results for NH_3/H_2 mixtures at 40 bar observed here. Also, while the improved predictions for the mechanism of Klippenstein et al. [31] at 20 bar and lean conditions (Fig. 3.9 a and b) is noted, the agreement in [24] with the measurements under the same conditions is significantly poorer. Possible origins of these differences will be discussed below.

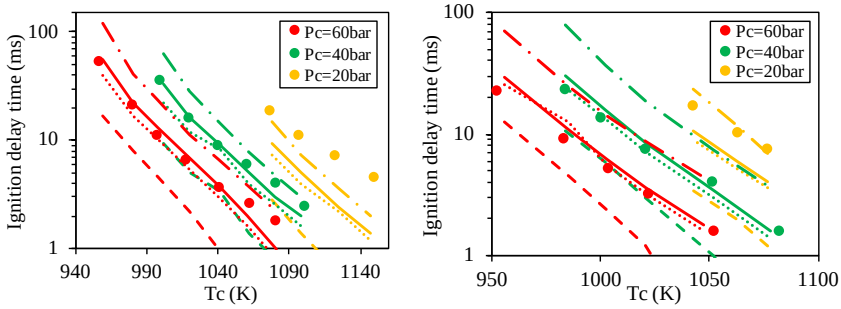

(a) φ = 0.5, 5% H_2 addition (b) φ = 0.5, 10% H_2 addition

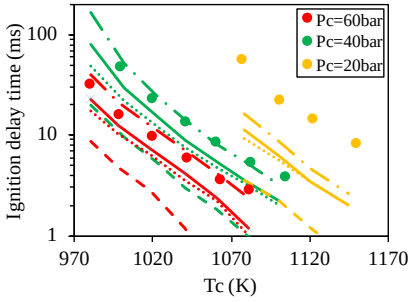

(c) φ =1.0, 5% H_2 addition

Figure 3.9. Measured (points) and calculated (lines) ignition delay times as function of temperature for mixture 5% H_2, φ =0.5 (a), 10% H_2, φ =0.5 (b) and 5% H_2, φ =1.0 (c). Solid lines: using the mechanism in this work, dashed lines: the Shrestha et al. mechanism [86], dotted lines: the Mathieu and Petersen mechanism [22] and dash-dot lines: the Klippenstein et al. mechanism [31].

3.2.3 Comparison with previous RCM measurements

As mentioned in the introduction, very recently He et al. [24] also reported ignition delay time measurements for NH_3/H_2 mixtures. They found

that the mechanism from Glarborg et al. [30] underpredicts the ignition delay times for NH_3/H_2 mixtures compared to their measurements. For instance, an underprediction by a factor of ~3 was observed at φ = 0.5, P_c = 40 bar with 5% H_2 addition (Fig. 3.5c in [24]). The ignition delay times measured for the same conditions in this study are consistent with those measured by He et al. [24]. However, as shown in Fig. 3.10, calculated ignition delay times using the current mechanism (with marginal differences in computed delay times compared with those obtained using Glarborg et al. [30]) agree to better than 30% with the ignition delay times measured under the same conditions.

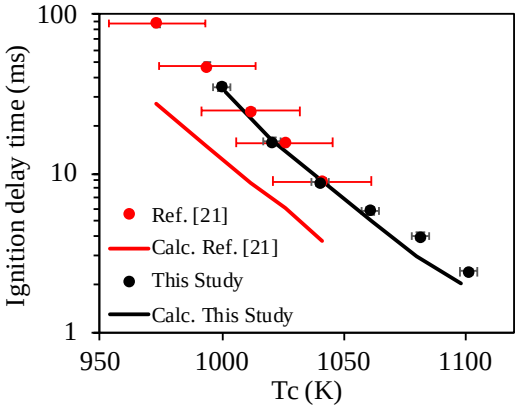

Figure 3.10. Comparison between the measurements from He et al. [24] and this study at φ = 0.5, 5% H_2 addition, P_c = 40 bar. (For explanation of the error bars, see text.)

Since the ignition delay times were simulated using pressure traces derived from non-reactive mixtures, a difference in the way in which the non-reactive experiments were performed is noticed between [24] and the method used here, which may contribute to the observed differences. In [24], as well as in [35,39,98], the non-reactive experiments were conducted by replacing the O_2 in the combustible mixtures with the same fraction of N_2. Because N_2 has slightly smaller heat capacity than O_2, this leads to larger ratios of the heat capacities and thus to higher T_c in the non-reactive experiments than in the reactive mixture. For example, a set of measured pressure traces and the derived volume traces for 'mixture 5b' in [24] were provided to us by the authors of [24], shown in Fig. 3.11. The non-reactive pressure and volume traces show differences with the reactive traces. The equivalent non-reactive temperature history for this example gives T_c roughly 15 K higher than that derived from the measured profile. In the present study, rather than replacing

the oxygen by nitrogen to yield the unreactive mixture, the difference in the heat capacities between O_2 and N_2 were considered: the N_2 fraction was adjusted (to be slightly larger than that of the O_2 being replaced, with a corresponding reduction in the Ar fraction) to give the same average ratio of the heat capacities as in the reactive mixture. This results in a faithful duplication of the peak pressure and pressure decrease after compression but prior to ignition as shown in Fig. 3.12. The differences in computed temperature after compression (T_c) were less than 1 K in this case. When using the reactive mixture heat capacity in the non-reactive volume trace from [24], the pressure trace still shows the same discrepancy with the measured reactive trace, but the error in the maximum temperature is reduced to roughly 4 K. (The 4 K inconsistency when simply replacing oxygen by the same fraction of nitrogen is specific for this example; under other conditions, the inconsistency could be significantly different.) Although significant, the 4 K for this example is still not enough to account for the differences in simulated results observed in the present comparison. A direct comparison of the reactive pressure traces in Figs. 3.11 and 3.12 (visible in the insets in these figures) shows that the pressure (and coupled to it the temperature) after compression in the profile from [24] is nearly constant until ignition, while the pressure profile measured here decreases significantly after compression. Since T_c in both mixtures is reported to be the same, it is not physically reasonable for these two profiles to give the same ignition delay time.

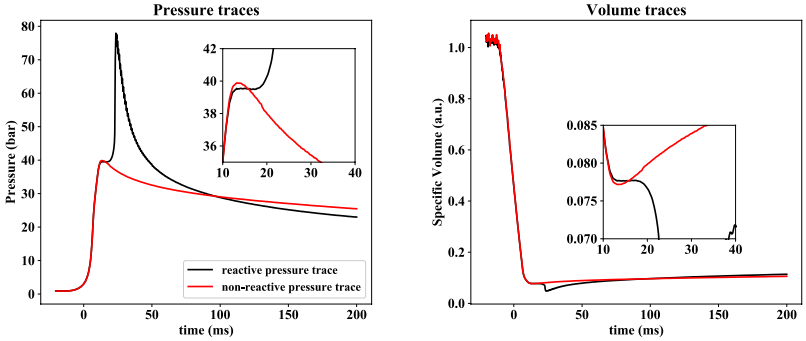

Figure 3.11. Pressure traces of combustible (black) and non-reactive (red) gas of 'mixture 5b' from [24] measured at T_c = 1041.2 K, P_c = 39.5 bar and temperature and specific volume traces derived from pressure traces.

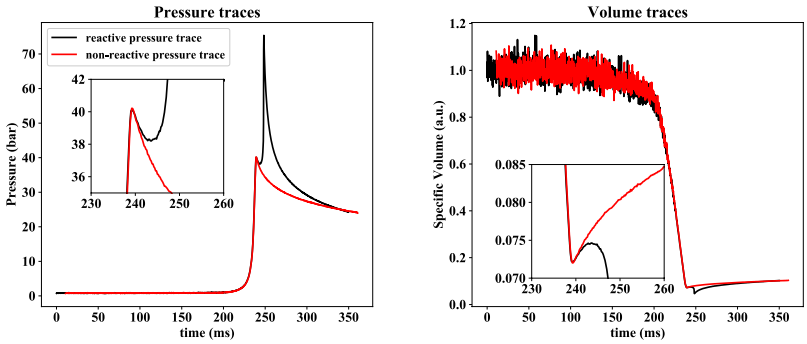

Figure 3.12. Pressure traces of combustible (black) and non-reactive (red) gas of 'mixture 6' of this study measured at T_c = 1040.5 K, P_c = 40.1 bar and temperature and specific volume traces derived from pressure traces.

The supplementary material in [24] discusses the uncertainties in the experimental conditions, particularly initial temperature and pressure after compression, that result in a net uncertainty in T_c of 10-20 K. In Fig. 3.10 this uncertainty in the measurement conditions is reflected, using error bars of ± 20 K as an example. As shown in [24], this results in an uncertainty in the computed ignition delay time of roughly a factor of three; Fig. 3.10 shows that a difference of 20 K in T_c is enough to bring the measured and simulated ignition delay times reported in [24] to within ~50%. In the current report, the measured quantities are ascertained to yield the resultant ± 3.5 K [77] uncertainty in T_c noted above and indicated by the error bars in Fig. 3.10. This uncertainty in T_c translates into an uncertainty in the computed ignition delay times of 5-10%. The differences in the pressure profiles for similar reported experimental conditions and uncertainty in the temperature after compression argue for caution when regarding the apparent excellent agreement between the experimental results suggested by the points neglecting the error bars seen in Fig. 3.10. Inclusion of the error bars for T_c facilitates the quantitative interpretation of the degree to which simulations and measurements are consistent.

Based on these observations, this discussion emphasizes the importance of matching the heat capacity of the reactive mixture when determining the volume profile from the non-reactive mixture, indicating the uncertainty in T_c and reducing the uncertainty in the quantities that determine T_c when quantitatively assessing the agreement between experimental and simulated ignition delay times for the purposes of mechanism evaluation.

3.2.4 Kinetic analysis

To analyze the effect of H_2 addition on the ignition delay times, a sensitivity analysis using the current mechanism was performed. The sensitivities at φ = 0.5, T_c = 1080 K, P_c = 60 bar with H_2 fractions of 0, 5 and 10% are shown in Fig. 3.13. The most important reaction promoting ignition for pure NH_3 under these conditions is $H_2NO + O_2 = HNO + HO_2$, followed by $NH_2 + NO = NNH + OH$ and reactions of NH_2 with HO_2, NO_2 and O_2 producing reactive intermediates and radicals like H_2NO, OH, O and NO. Oxygen is directly involved in the oxidation of H_2NO and NH_2, and in the formation of NO; these reactions will be promoted if more O_2 is provided, resulting in shorter ignition delay times, consistent with the results measured in leaner mixtures as shown in Fig. 3.4. The most inhibiting reactions are the terminating steps $NH_2 + NO = H_2O + N_2$ and $NH_2 + NO_2 = H_2O + N_2O$, which compete with the promoting reactions $NH_2 + NO = NNH + OH$ and $NH_2 + HO_2 = H_2NO + OH$. The competition between these reactions is discussed in detail in [31].

With H_2 addition, key reactions involved in the H_2/O_2 mechanism become important, including the competition between $H + O_2 = O + OH$ and $H + O_2 (+M) = HO_2 (+M)$, for which the ignition of pure ammonia exhibits virtually no sensitivity. The dissociation of H_2O_2, $H_2O_2 (+M) = 2OH (+M)$, becomes the second most important ignition-enhancing reaction at a relatively modest 10% H_2 in the fuel. The increased sensitivity of ignition to $HO_2 + NH_3 = H_2O_2 + NH_2$ upon hydrogen addition as compared to pure ammonia is observed in the Figure. Note that while hydrazine formation is an important step in ammonia oxidation, Fig. 3.13 indicates a sensitivity of at most ~10%, consistent with the observation that the changes in the rate constant for this reaction presented in Section 3.1 has only a modest effect on the ignition delay time as compared with the mechanism in [30].

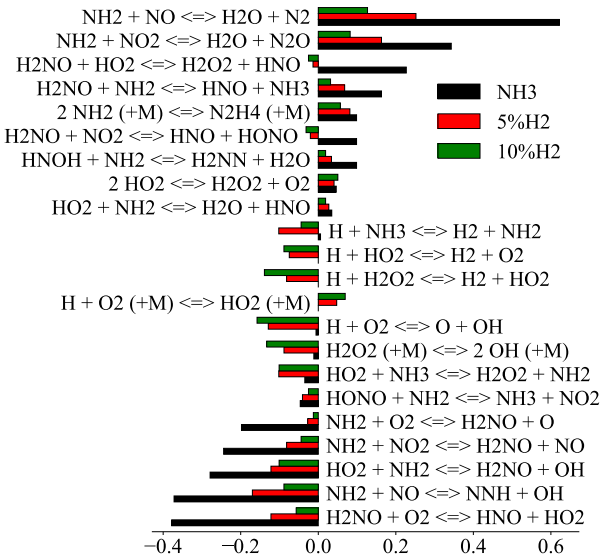

Figure 3.13. Sensitivity analysis for the ignition delay time of NH_3 with 0, 5 and 10% H_2 addition at φ = 0.5, T_c =1080 K, P_c = 60 bar.

Figure 3.14 shows the most sensitive reactions for pure NH_3 and NH_3 with 5 and 10% H_2 addition at φ = 1.0, T_c = 1080 K, P_c = 60 bar. The most sensitive reactions for pure NH_3 at φ = 1.0 are identical to those for pure NH_3 at φ = 0.5. The reactions H + O_2 = O + OH and H_2O_2 (+M) = 2OH (+M) remain important for H_2 addition at φ = 1.0. Interestingly, at 5% H_2 addition the reaction H + NH_3 = H_2 + NH_2, which gives no sensitivity at φ = 0.5, is seen to be ignition enhancing addition at the same level of sensitivity as the branching reaction between NH_2 and HO_2, while at 10% H_2 the sensitivity all but vanishes. These results suggest that, under stoichiometric conditions, the shortage of hydrogen enhances the importance of H+NH_3=H_2+NH_2. While the sensitivities observed for the conditions here (60 bar) are qualitatively similar to those reported in [24] (up to a maximum pressure of 40 bar), there are some differences in the relative ranking. Since the sensitivity analyses in [28] appear to be normalized (while here they are not), and with no details as to how the analyses were performed, this study refrains from a detailed comparison with the analysis presented there. Note that in [24] the mechanism from [30] shows H + NH_3 = H_2 + NH_2 as ignition inhibiting at 20% H_2 in the mixture, in contrast to the ignition-enhancing behavior observed here at lower H_2 fractions.

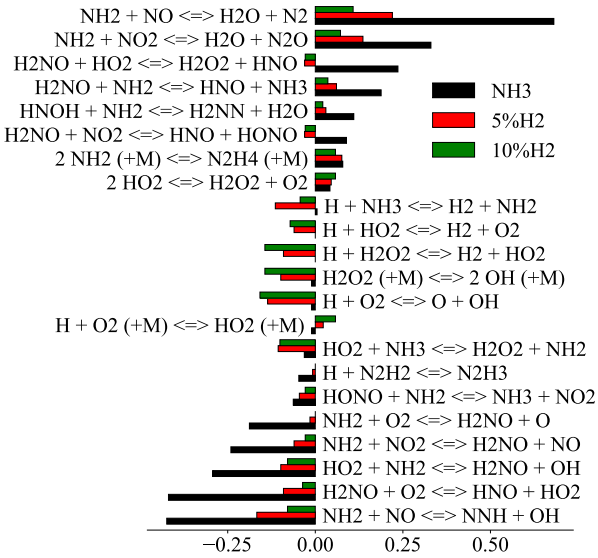

Figure 3.14. Sensitivity analysis for the ignition delay time of NH_3 with 0, 5 and 10% H_2 addition at φ = 1.0, T_c =1080 K, P_c = 60 bar.

The reaction path of pure NH_3, calculated using the current mechanism, is shown in Fig. 3.15. Fluxes lower than 5% are not shown to avoid clutter. As can be seen, ammonia is primarily consumed by O, H and OH radicals, producing the amine radical NH_2. The NH_2 radical is partly converted into NO in the sequence $NH_2 \xrightarrow{+HO_2,\, NO_2} H_2NO \xrightarrow{+O_2} HNO \xrightarrow{+O_2} NO$. Nitric oxide then reacts with NH_2 through either $NH_2 \xrightarrow{+NO} N_2$ or $NH_2 \xrightarrow{+NO} NNH \xrightarrow{+O_2} N_2$. The NH_2 radical can also recombine to form hydrazine (N_2H_4), followed by sequential H abstraction to form N_2. The reaction path of NH_3 with 10% H_2 (not shown) indicates that 10% H_2 addition had no significant influence on the NH_3 oxidation paths. While the major paths observed here are similar to those reported in [24], using the mechanism in [30], the route via hydrazine has been left out of the analysis in [24]. However, the path to hydrazine formation changes the routing of NH_2 by only 10% under the conditions described here.

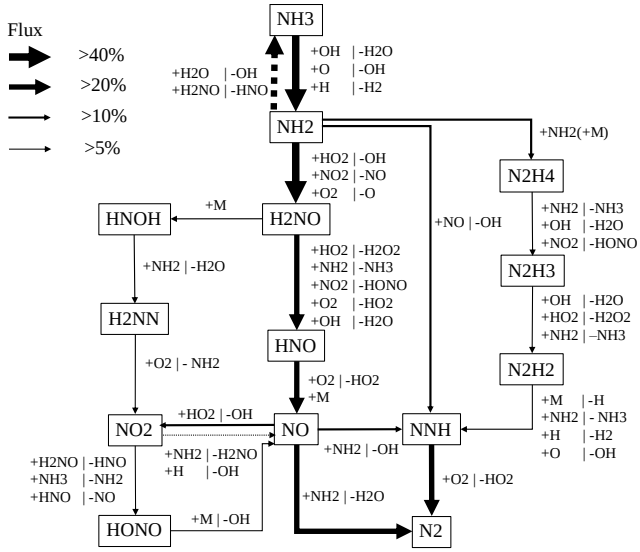

Figure 3.15. Reaction path diagram for pure NH_3 at φ = 0.5, T_c =1080 K, P_c = 60 bar.

To obtain a better understanding of the effect of H_2 addition on ignition, the species histories for H_2O_2, HO_2, OH and H in the period leading to ignition for pure NH_3 and for 10% H_2 addition were calculated using the current mechanism, shown in Fig. 3.16. For this purpose, the calculations are performed as constant volume simulations.

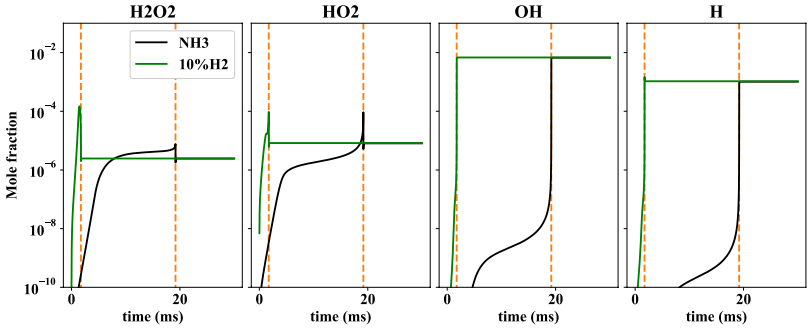

Figure 3.16. Selected species history in ignition of NH_3 (black lines) and NH_3 with 10% H_2 addition (green lines) at φ = 0.5, T_c = 1080 K, P_c = 60 bar. Orange dashed line –time at which ignition occurred in the simulations.

As can be seen, with 10% H_2 addition, hydrogen peroxide H_2O_2 and HO_2 accumulate before ignition to a fraction that is ~10 times higher than when igniting pure NH_3. This results in a faster buildup of the radical pool, particularly for OH. Similar species histories were found at φ = 1.0. Clearly,

with only modest hydrogen addition the fractions of species that are important for the ignition in fuels dominated by the H_2/O_2 mechanism are drastically increased.

3.3. Summary and Conclusions

In this chapter, measurements of autoignition delay times of NH_3 and NH_3/H_2 mixtures in a rapid compression machine are reported at pressures from 20 - 75 bar and temperatures in the range 1040-1210 K. The equivalence ratio, using $O_2/N_2/Ar$ mixtures as oxidizer, varied for pure NH_3 from 0.5 to 3.0; NH_3/H_2 mixtures with H_2 fraction between 0-10% were examined at equivalence ratios 0.5 and 1.0. In contrast to many hydrocarbon fuels, the results indicate that, for the conditions studied, autoignition of NH_3 becomes slower with increasing equivalence ratio. Hydrogen is seen to have a strong ignition-enhancing effect on NH_3. The experimental data, which show similar trends to those observed previously by He et al. (2019), were used to evaluate four NH_3 oxidation mechanisms: a new version of the mechanism described by Glarborg et al. (2018), with an updated rate constant for the formation of hydrazine, $NH_2 + NH_2 (+M) = N_2H_4 (+M)$, and the literature mechanisms from Klippenstein et al. (2011), Mathieu and Petersen (2015), and Shrestha et al. (2018). In general, the mechanism from this study has the best performance, yielding satisfactory prediction of ignition delay times both of pure NH_3 and NH_3/H_2 mixtures at high pressures (40-60 bar). Kinetic analysis based on present mechanism indicates that the ignition enhancing effect of H_2 on NH_3 is closely related to the formation and decomposition of H_2O_2; even modest hydrogen addition changes the identity of the major reactions from those involving NH_x radicals to those that dominate the H_2/O_2 mechanism. Flux analysis shows that the oxidation path of NH_3 is not influenced by H_2 addition. The results also indicate the methodological importance of using a non-reactive mixture having the same heat capacity as the reactive mixture for determining the non-reactive volume trace for simulation purposes, as well as that of limiting the variation in temperature after compression, by limiting the uncertainty in the experimentally determined quantities that characterize the state of the mixture.

Chapter 4: Autoignition studies of NH_3/CH_4 mixtures at high pressure

This chapter is based on the work presented in: L. Dai, S. Gersen, P. Glarborg, A. Mokhov, H. Levinsky . Autoignition studies of NH_3/CH_4 mixtures at high pressure. Combust Flame 2020;218:19-26.

4.1 Experimental conditions

To quantify the impact of methane addition to ammonia on autoignition and to provide benchmark data for mechanism evaluation, this chapter reports ignition delay times of NH_3 and NH_3/CH_4 mixtures measured in an RCM, at equivalence ratios of 0.5, 1.0 and 2.0, with CH_4 addition of 0, 5, 10 and 50%, pressures in the range 20 - 70 bar, and temperatures from 930 to 1140 K. Furthermore, the measurements are used to assess the veracity of predictions of ignition using recently developed chemical mechanisms appropriate for ammonia/methane ignition. In addition to the mechanism presented in our previous report on NH_3/H_2 [70], using a modified mechanism from the review on nitrogen chemistry and hydrocarbon/nitrogen interactions by Glarborg et al. [30], five NH_3/CH_4 mechanisms taken from the literature are also evaluated: the mechanism from Shrestha et al. [86], the "San Diego" mechanism [99], the mechanism from Tian et al. [100], the Li-Konnov mechanism [101] and the mechanism from Okafor et al. [102]. In addition, a kinetic analysis is performed to provide insight into the changes in ammonia oxidation upon methane addition that are responsible for the ignition behavior of the mixtures.

The ignition delay time measurements were performed in the RCM whose details are described in Chapter 2. The compositions (in mole fraction) of the mixtures examined in this Chapter are shown in Table 4.1. The simulation method for RCM experiments has been discussed in Chapters 1 and 2.

Table 4.1. Compositions of NH_3/CH_4 mixtures

Mixtures	φ	CH_4/fuel	NH_3	CH_4	O_2	N_2	AR
Mixture 1*	0.5	0	0.118	0	0.176	0	0.706
Mixture 2	0.5	5%	0.104	0.006	0.178	0	0.712
Mixture 3	0.5	10%	0.098	0.011	0.191	0.105	0.595
Mixture 4	0.5	50%	0.04	0.04	0.22	0.2	0.5
Mixture 5	1.0	10%	0.144	0.016	0.14	0	0.7
Mixture 6	2.0	10%	0.188	0.021	0.091	0	0.7

* Mixture 1 is taken from Chapter 3.

4.2. Results and discussion

4.2.1 Effect of CH_4 addition at lean conditions

The ignition delay times of NH_3 with CH_4 addition from 0 to 50% were measured at fixed P_c = 60 bar and $\varphi = 0.5$, at temperatures ranging from 930 K to 1140 K, as shown Fig. 4.1. As can be seen, the observed ignition delay times decrease roughly exponentially with increasing temperature at all pressures. The figure illustrates a substantial ignition-enhancing effect of CH_4 addition to NH_3: the ignition delay times of NH_3 are reduced by a factor of ~5 with even a small quantity (5%) of CH_4 at T_c = 1100 K. Under the conditions of the experiments, no ignition is observed below ~1050 K for pure ammonia, while methane addition extends the limit of ignition considerably. As seen in Fig. 4.1, the effect of CH_4 addition decreases at higher CH_4 fraction; the ignition delay times are globally decreased by a factor of ~3 between 5 and 10% methane, and by a factor of ~2 when going from 10% to 50% in the mixture. The calculations, using the mechanism from Glarborg et al. [30] with the modification proposed in [70] and discussed in Chapter 3, predict the measured delay times to better than 30% for 0-10% methane addition; at 50% CH_4, the maximum deviation is ~50%, at T_c = 1025 K.

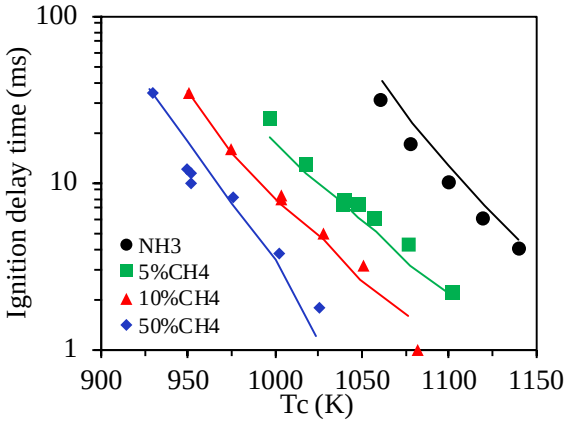

Figure 4.1. Measured (symbols) and calculated (lines) ignition delay times of NH_3 with different CH_4 additions at $\varphi = 0.5$, P_c = 60 bar. The data for pure NH_3 are taken from Chapter 3. (Both vertical (±5%) and horizontal (±3.5 K) error bars are not visible in this and other figures). Calculations using the mechanism from [30,70].

Examining the pressure dependence at fixed temperature, Figure 4.2 shows the ignition delay time measurements as function of pressure at T_c = 1080 K for 0, 5 and 10% CH_4 (Fig. 4.2a), and at T_c = 1000 K for 10% and 50%

CH_4 (Fig. 4.2b). The ignition delay times decrease monotonically with increasing pressure for all conditions measured, as also observed for other fuels [79,103], and the curves are more or less parallel. At T_c = 1080 K, the ignition delay times of pure NH_3 are reduced by a factor of ~5 by 5% CH_4 addition and reduced by an additional factor of 2 when increasing the methane fraction to 10%. At T_c = 1000 K, 50% CH_4 reduces the ignition delay times by another factor of 2.5 as compared to 10% CH_4, also illustrative of the decreasing effect of methane addition at higher methane fraction in the fuel, as observed in Fig. 4.1. Similar to the data in Fig. 4.1, for the data in Fig. 4.2 the mechanism from [30,70] predicts the ignition delay times to within 25% for methane-containing mixtures above ~30 bar, whereas the difference increases to 50% below this pressure. Since data in Fig. 4.1 for 50% CH_4 in the mixture are already within a factor of two of those for pure methane under similar conditions [104,105], the measurements were not extended to higher methane fractions.

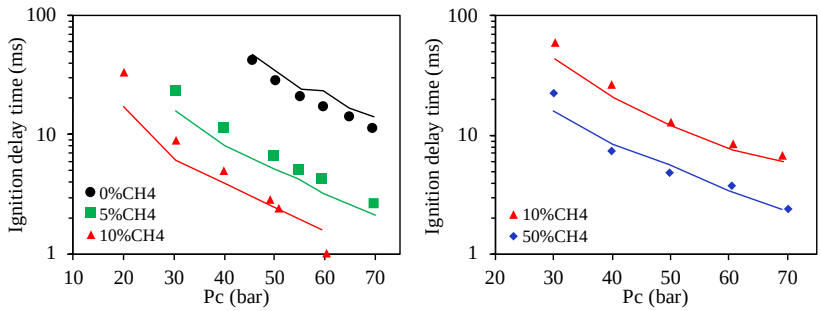

(a) T_c =1080K (b) T_c =1000K

Figure 4.2. The measured (symbols) and calculated (lines) ignition delay times with different CH_4 additions at fixed T_c =1080 K (a) and T_c =1000 K (b). Calculations using the mechanism from [30,70].

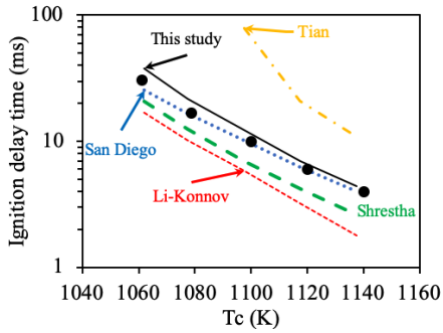

Figure 4.3. Measured (symbols) and calculated (lines) ignition delay times of pure NH_3 at φ = 0.5, Pc = 60 bar. Calculations are based on the mechanisms from [30,70] ("This study"), Shrestha et al. [86], "San Diego" [99]**, Tian et al.** [100]**, Li-Konnov** [101] **and Okafor et al.** [102]**, respectively.**

Extending the comparison of the measurements with the simulations to the other mechanisms for ammonia/methane ignition indicated above, Fig. 4.3 shows the comparison of simulations from all 6 mechanisms with the measurements of pure NH_3 at φ = 0.5 and P_c = 60 bar taken from Fig. 4.1, above. In general, the calculations using the mechanism from Tian et al. [100] overpredicts the ignition delay times by more than a factor of 3, while the calculations using the San Diego mechanism [99] agree very well with the measurements. The mechanisms from both Shrestha et al. [86] and Li-Konnov [101] consistently underpredict the measurements by a factor of ~1.5 and ~2, respectively. The mechanism from Okafor et al. [102] fails to predict ignition for pure NH_3 under the conditions in this study.

The measured ignition delay times of NH_3 with 50% CH_4 taken from Fig. 4.1 and the calculations using the 6 mechanisms are compared in Fig. 4.4. Calculations using Tian et al. [100] and the San Diego [99] mechanism both overpredict the ignition delay times by a factor of ~2. The mechanism from Shrestha et al. [86] and the Li-Konnov [101] mechanism both slightly underpredict the ignition delay times, by a factor of ~1.5. While failing to predict any ignition in pure ammonia, the mechanism from Okafor et al. [102] predicts ignition delay times for this NH_3/CH_4 mixture that are too long by a factor of ~20. Additional comparisons between the full set of measurement data and calculations using the different mechanisms are provided in Appendix 4.1. Since the mechanism from [30,70] consistently predicts the experimental data well for all mixtures studied here, only comparisons with this mechanism will be discussed below.

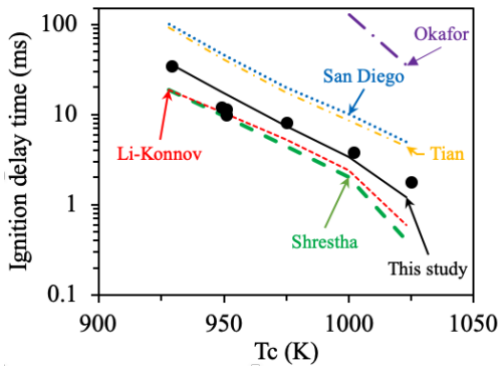

Figure 4.4. Measured (symbols) and calculated (lines) ignition delay times of NH_3 with 50% CH_4 at φ = 0.5, Pc = 60 bar. Calculations are based on the mechanisms from [30,70] ("This study"), Shrestha et al. [86], "San Diego" [99]**, Tian et al.** [100]**, Li-Konnov** [101] **and Okafor et al.** [102]**, respectively.**

4.2.2 Effect of equivalence ratio

The ignition delay times of NH_3 with 10% CH_4 addition were also measured at φ = 1.0 and 2.0 as a function of temperature at P_c = 60 bar and as a function of pressure at T_c = 1000 K, shown in Fig. 4.5a and 4.5b, respectively. As can be seen in both figures, the differences in the ignition delay times at φ = 0.5 and 1.0 are less than 10%. Increasing φ from 1.0 to 2.0 increases the measured ignition delay times by a factor of ~1.5. Ignition delay times of pure NH_3 at these three equivalence ratios were reported previously in Chapter 3 [70] and [24]; in Chapter 3 it was found that ignition delay times of pure NH_3 is increased by a factor of 2 when increasing φ from 0.5 to 1.0 and another factor of 2 when φ is increased from 1.0 to 2.0. Ammonia has longer ignition delay times at higher φ, while the trend is opposite for common hydrocarbon fuels [76,105]. Phenomenologically, the results imply that, upon increasing the equivalence ratio from 0.5 to 1.0, the faster ignition of the hydrocarbon is counteracted by the slower ignition of the ammonia, resulting in no change in the results. Upon increasing φ from 1.0 to 2.0, any potential ignition enhancement from the presence of 10% methane with increasing φ appears to be overwhelmed by the increased delay time from ammonia. The mechanism from [30,70] predicts the ignition delay times very well at all three equivalence ratios, with deviations less than 30% at φ = 0.5 and 1.0 and with an underprediction of less than 40% at φ = 2.0.

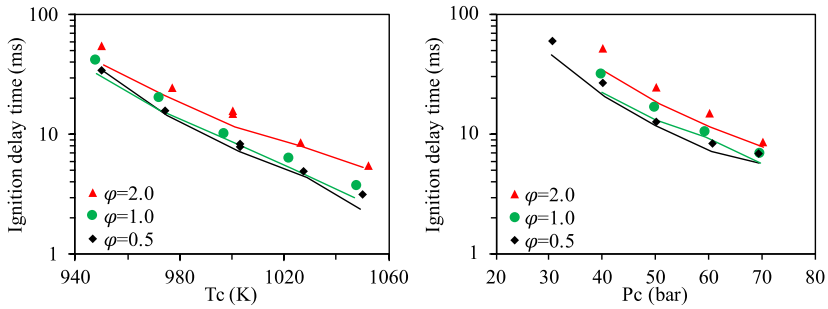

(a) P_c = 60 bar (b) T_c = 1000 K

Figure 4.5. Ignition delay times of NH_3 with 10% CH_4 addition at φ = 0.5, 1.0 and 2.0. Symbols are measurements, lines simulations using the mechanism from [30,70] (see text).

4.2.3 Anomalous pre-ignition pressure rise at 50% methane

For the mixture that contains 50% methane in NH_3, an anomalous pre-ignition pressure rise was observed at three conditions (950 K/60 bar,

1000 K/40 bar and 1000 K/50 bar), which resulted in accelerated ignition, similar to that reported for pure NH_3 reported in [24]. In our experiments, this phenomenon was not observed in other fuel mixtures. Normal ignition is illustrated in Fig. 4.6a, in which the pressure rise at ignition is very sharp. In contrast, the pressure trace shown in Fig. 4.6b shows a slow rise over several milliseconds before ignition occurs. Contrary to the reports for NH_3 [24] and ethanol [106], who reported that this phenomenon was irregular, the slow pre-ignition pressure rise observed here was very reproducible: the observed ignition delay time was reproducible to within 2 ms at T_c = 950 K, P_c = 60 bar. This is similar to the results discussed in [107] for ethanol measurements in a shock tube. It's necessary to point out that the phenomenon reported here resulted in a shortened ignition delay time as compared to the computations, as also noted in [107]; the three points below the simulation line in Fig. 4.1 at 950 K, and Fig. 4.2 at 40 and 50 bar are examples of this, while the other experimental points are on or above the simulation line. No simulations (using any of the 6 mechanisms examined) reflected a slow pre-ignition pressure rise. Whether the observed effect arises through the mechanism operative in [107], referred to phenomenologically as "sequential autoignition", or from some condition-specific chemistry involving the coupling between ammonia and hydrocarbon chemistry not manifest in the current mechanism is a subject of future investigation. However, this study does warn that the occurrence of a significant shortening of the ignition delay time could seriously affect the knock resistance of an ammonia/methane fuel adversely in practical engines.

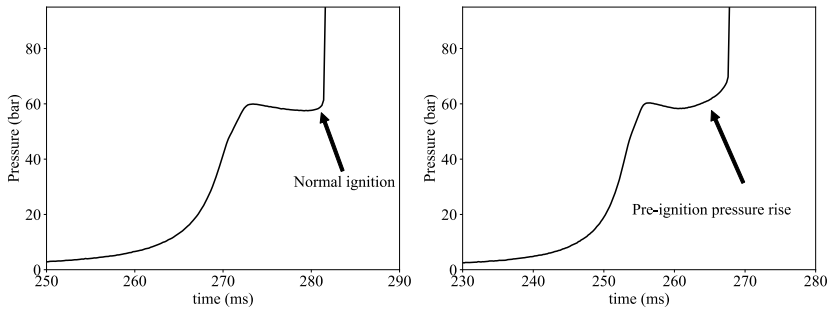

(a) T_c = 975 K, P_c = 60 bar (b) T_c = 950 K, P_c = 60 bar

Figure 4.6. Pressure traces of normal ignition (a) and anomalous pre-ignition pressure rise (b) observed at 50% CH_4 addition.

4.2.4 Kinetic analysis

It will be useful for the discussion of the kinetic aspects of ammonia/methane ignition first to consider the overall oxidation pathways for these mixtures obtained from a flux analysis. This will also expose any interaction between NH_3 and CH_4 during oxidation. A flux analysis was performed for the mixtures studied by tracing both the N (Fig. 4.7a) and C (Fig. 4.7b) elements, at $\varphi = 0.5$, $T_c = 1000$ K, $P_c = 60$ bar; as stated above, the flux was analyzed at the point at which 20% of the fuel is consumed. Since the flux analysis for pure ammonia using the same mechanism as applied here has been reported in Chapter 3 (albeit at somewhat higher temperature), this analysis focuses on the differences in reaction path caused by methane addition. As observed previously in Chapter 3 [70] and [23,24], the initial step in ammonia oxidation is to form NH_2, with further oxidation proceeding via either H_2NO or N_2H_4, following reaction of NH_2 with HO_2 or NH_2. At 50% CH_4, while the major oxidation path of NH_3 is unaltered (except that the N_2H_4 channel is suppressed, with a flux lower than 5%), the analysis shows the participation of carbon-containing species as reactants with the nitrogen species. Thus CH_4 and CH_3 become significant in $NH_2 + CH_4 = NH_3 + CH_3$ and $CH_3 + H_2NO = NH_2 + CH_3O$, with the former reaction being the dominant reaction for converting NH_2 back into NH_3. Meanwhile, CH_3NO_2 formation becomes an important route at 50% CH_4 addition. Nitromethane is produced mainly by recombination of CH_3 and NO_2 at low temperatures, but dissociates as the temperature increases. As shown in Fig. 4.7b, amine radicals influence the CH_4 oxidation route primarily in the initial stage. CH_4 undergoes H abstraction by NH_2, OH, O and H radicals; the reaction with NH_2 (to produce NH_3 as mentioned above) is second only to oxidation of methane by OH. The methyl radical is mainly oxidized by N-containing species into CH_3O, either directly (by H_2NO and NO_2) or via CH_3OO (by NO). Comparing the paths at 10% CH_4 addition between $\varphi = 0.5$ and $\varphi = 2$ (not shown) indicates little change in the main ammonia routes, but the methane path shifts towards oxidation via ethane following recombination of methyl radicals, as is the case for pure methane. Interestingly, at $\varphi = 2$, $CH_3 + NH_2 (+M) = CH_3NH_2 (+M)$ becomes a significant destination for NH_2 radicals, consistent with the sensitivity analysis (see below).

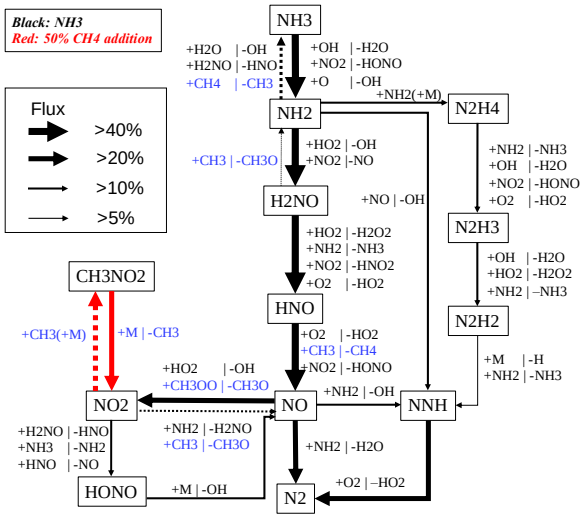

(a) Pure NH_3 and NH_3 with 50% CH_4

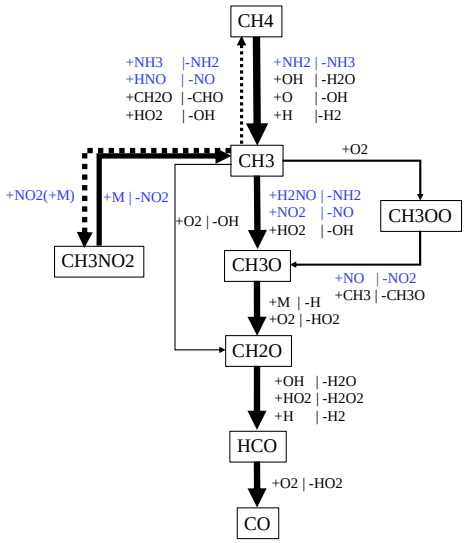

(b) NH_3 with 50% CH_4

Figure 4.7. Flux analysis for elemental nitrogen (a) and carbon (b) showing impact of 50% CH_4 in fuel mixture at φ = 0.5, T_c = 1000 K, P_c = 60 bar, at 20% fuel consumption. In (a), black species indicate the reactants for pure NH_3, while blue species are reactants from methane oxidation. In (b), the blue species indicate reactants from NH_3 oxidation that participate in CH_4 oxidation. The red arrows in (a) indicate an additional path step coupling the N and C paths. (Fluxes lower than 5% are not shown to avoid clutter.)

Sensitivity analyses were performed for NH_3 with different CH_4 fractions at φ = 0.5, T_c = 1000 K, P_c = 60 bar, as shown in Fig. 4.8a. As observed

previously in Chapter 3 and [24], $H_2NO + O_2 = HNO + HO_2$ and $NH_2 + NO = NNH + OH$ promote ignition most in pure NH_3, and compete with $NH_2 + NO = H_2O + N_2$, as most inhibiting. At 5% CH_4, two new promoting reactions appear: $CH_4 + NH_2 = CH_3 + NH_3$ and $CH_3OO + NO = CH_3O + NO_2$. However, at 50% CH_4, $CH_4 + NH_2 = CH_3 + NH_3$ becomes slightly inhibiting. Examination of the net rates of reaction shows that this reaction proceeds in the direction as written for methane fractions in the range of 5-95%. Apparently, NH_2 is an important reactant for initiating the decomposition of CH_4 at low methane fraction, while at high methane fraction, production of relatively unreactive CH_3 (in terms of methane oxidation) and reconversion of NH_2 in the fuel NH_3 modestly inhibits ignition. At 50% methane, a shift is observed in the most important reactions for ignition from those among nitrogen-containing species themselves or with oxygen, as indicated above, to reactions involving H_2O_2 and HO_2, as expected in hydrocarbon ignition. Thus, the decomposition of H_2O_2 and the reaction $HO_2 + NH_2 = H_2NO + OH$ promote ignition most, while $2HO_2 = H_2O_2 + O_2$ is the most inhibiting at 50% methane. However, none of the inhibiting reactions exceeds 10% sensitivity.

To explore the effect of equivalence ratio on ignition delay times of NH_3/CH_4 mixtures, sensitivity analyses for NH_3 with 10% CH_4 addition were performed at φ = 0.5, 1.0 and 2.0, as shown in Fig. 4.8b. Generally, variation in the equivalence ratio has a modest influence on the most sensitive reactions for NH_3 ignition with 10% CH_4 in the mixture; the most sensitive reactions are the same as those observed in Fig. 4.8a at φ = 0.5 and 5% CH_4. However, at φ = 2.0, the analysis shows that $CH_3OO + NO = CH_3O + NO_2$ has the largest promoting effect; this reaction converts the comparably unreactive peroxide to methoxy, which rapidly dissociates to yields atomic hydrogen. Since NO production is relatively limited under fuel-rich conditions, the increasing scarcity of this reactant presumably renders ignition more sensitive to this reaction and contributes to the increase in ignition delay time at this equivalence ratio seen in Fig. 4.5, above. The reaction $CH_3 + NH_2 = CH_3NH_2$ also gains in importance with increasing φ, resembling the recombination of methyl radicals in binding these species under richer conditions.

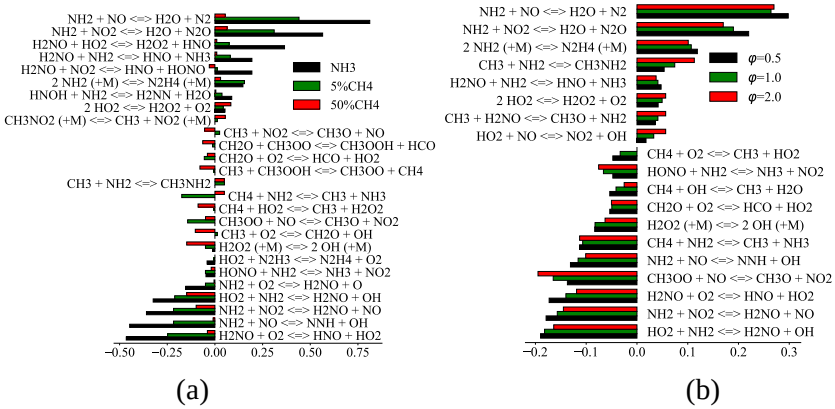

Figure 4.8. Sensitivity analysis of (a) NH_3 with different CH_4 fractions at φ = 0.5, T_c = 1000 K, P_c = 60 bar and (b) NH_3 with 10% CH_4 addition at different equivalence ratios.

The sensitivity results in Fig. 4.8b also suggest a reason for the constancy of the ignition delay time with when changing from φ = 0.5 to φ = 1 shown in Fig. 4.5 for 10% methane in the mixture. In addition to reactions involving O_2, HO_2 and NO/NO_2, which dominate the ignition of pure ammonia, additional reactions involving CH_4 and carbon-containing species present similar sensitivity in the analysis at 10% methane. Thus, the reduction in O_2 and other oxygenated species when going from φ = 0.5 to φ = 1 slows the ignition process through reactions such as $HO_2 + NH_2 = H_2NO + OH$, but can be compensated by reactions that benefit from the increase in the methane fraction, like $CH_4 + NH_2 = CH_3 + NH_3$, facilitating ignition under these conditions.

Similar to the analysis in Chapter 3 [70], Figure 4.9 illustrates the influence of CH_4 addition on the temporal profiles of some important species, at φ = 0.5, T_c = 1000 K, P_c = 60 bar, where the vertical dashed lines show the point of ignition. The largest change in species concentrations upon methane addition is on H_2O_2. As can be seen in Fig. 4.9, H_2O_2 is accumulated before ignition, with a maximum concentration two orders of magnitude higher at 50% CH_4 and whose growth is substantially faster than for pure NH_3. The importance of this species is further supported by ignition delay times computed for the same conditions as in Fig. 4.9 without H_2O_2 dissociation in the mechanism; this increases the ignition delay by a factor of 2 at 5% CH_4, increasing to a factor of 3 at 50% CH_4. Interestingly, despite its absence from the major reactions showing sensitivity for ignition in pure ammonia, H_2O_2

decomposition still has a major effect on the computed ignition delay time; removing the dissociation reaction from the mechanism increased the ignition delay for ammonia by a factor of 1.7. Together with the increasing sensitivity of ignition to H_2O_2 decomposition with increasing CH_4 fraction in the mixture, seen in Fig. 4.8, above, at least part of the ignition-enhancing effect of methane addition to ammonia can be ascribed to its impact on H_2O_2 formation.

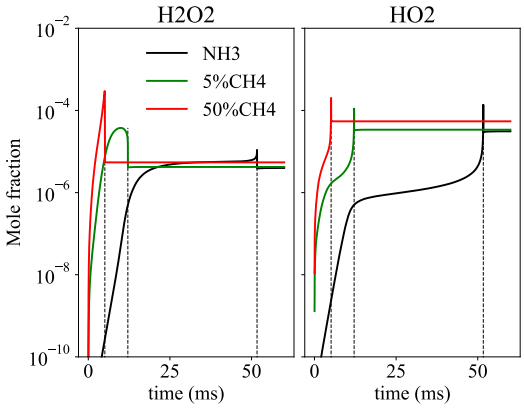

Figure 4.9. Species history at different CH_4 additions at φ = 0.5, T_c = 1000 K, P_c = 60 bar. Dashed lines indicate the time of ignition.

Given the importance of the dissociation of H_2O_2 in the ignition of all mixtures studied, the rate-of-production analysis (ROP) was performed at the same conditions as in Fig. 4.9 (φ = 0.5, T_c = 1000 K, P_c = 60 bar) for pure ammonia and 50% methane, included in the Appendix 4.2. The region below 1200 K is chosen to consider the buildup of species in the pre-ignition period seen in Fig. 4.9. It is observed that the primary formation reaction for H_2O_2 for both pure ammonia and 50% methane is $H_2NO + HO_2 = H_2O_2 + HNO$, but with a dramatic increase in the production rate (nearly a factor of 30 at 1200 K) in the pre-ignition period for 50% methane as compared to pure ammonia. The ROP for HO_2 under the same conditions shows that the dominant reaction for the formation of HO_2 is $HNO + O_2 = HO_2 + NO$ for pure ammonia, but is augmented with $HCO + O_2 = HO_2 + CO$ and $H + O_2 + M = HO_2 + M$; furthermore, the rates of these three reactions are (each) 20-30 times higher at 50% methane than the rate of $HNO + O_2$ for pure ammonia at the same temperatures. The higher rates for these reactions result in the higher rates of H_2O_2 formation indicated above and the buildup of H_2O_2 in Fig. 4.9.

4.3. Summary and Conclusions

In this chapter, autoignition delay times of NH_3/CH_4 mixtures with CH_4 fractions of 0, 5, 10 and 50% were measured in a rapid compression machine at equivalence ratio φ = 0.5, pressures from 20 - 70 bar and temperatures from 930 to 1140 K. In addition, measurements were performed for NH_3 mixtures with 10% CH_4 at φ = 1.0 and 2.0. Methane shows a strong ignition-enhancing effect on NH_3, which levels off at higher CH_4 fractions, as the ignition delay time approaches that of pure methane. Autoignition delay times at 10% CH_4 at φ = 0.5 and 1.0 are indistinguishable, while an increase of ignition delay times by factor of 1.5 was observed upon increasing φ to 2.0. The experimental data were used to evaluate six NH_3 oxidation mechanisms capable of simulating NH_3/CH_4 mixtures. The mechanism discussed in Chapter 3 shows the best performance: generally, it predicts the measured ignition delay times to better than 30% for all conditions, except for 50% CH_4 addition for which the differences increase up to 50% at the highest temperature. Sensitivity analysis based on the mechanism used indicates that under lean conditions the reaction $CH_4 + NH_2 = CH_3 + NH_3$ significantly promotes ignition for modest CH_4 addition (5% and 10%), but becomes modestly ignition-inhibiting at 50% CH_4. Sensitivity and rate-of-production analyses indicate that the ignition-enhancing effect of 50% CH_4 addition is closely related to the formation and decomposition of H_2O_2. Flux analysis for NH_3/CH_4 mixtures indicates that $CH_4 + NH_2 = CH_3 + NH_3$ contributes substantially to the decomposition of methane early in the oxidation process, while $CH_3 + NO_2 (+M) = CH_3NO_2 (+M)$ is a significant reservoir of NO_2 at low temperature. Additionally, an anomalous pre-ignition pressure rise phenomenon, which is not reproduced by the simulations, was observed with high reproducibility for the NH_3 mixture with 50% CH_4 addition.

Appendix 4.1

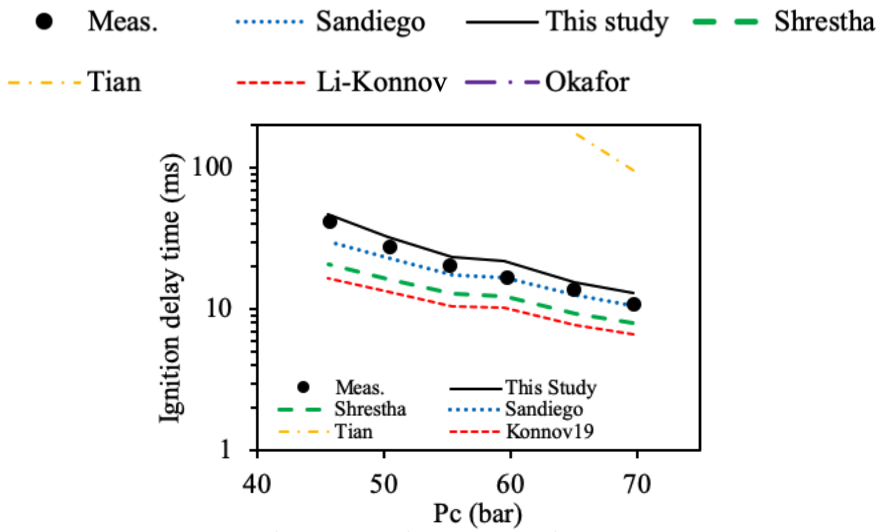

Figure A4.1.1. Measured (circles) and calculated (lines) ignition delay times of pure NH_3 at $\varphi = 0.5$, Tc = 1080K.

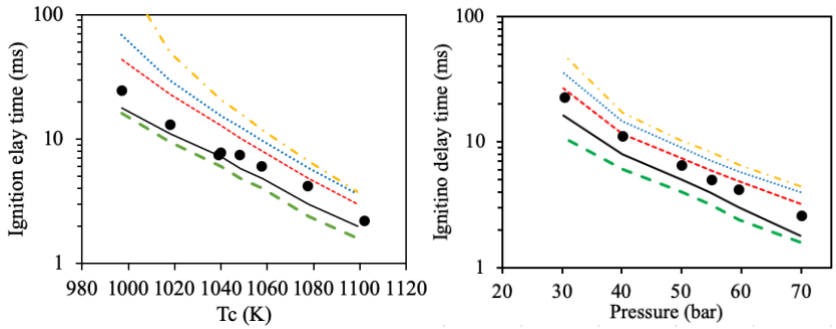

(a) P_c = 60 bar (b) T_c = 1080K

Figure A4.1.2. Measured (circles) and calculated (lines) ignition delay times of NH_3 with 5%CH_4 at $\varphi = 0.5$

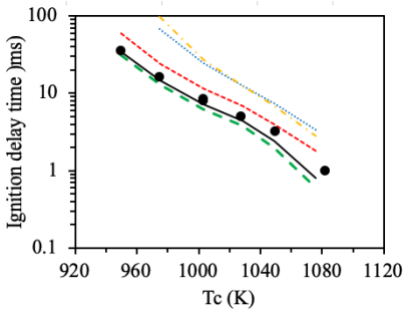

(a) P_c = 60 bar

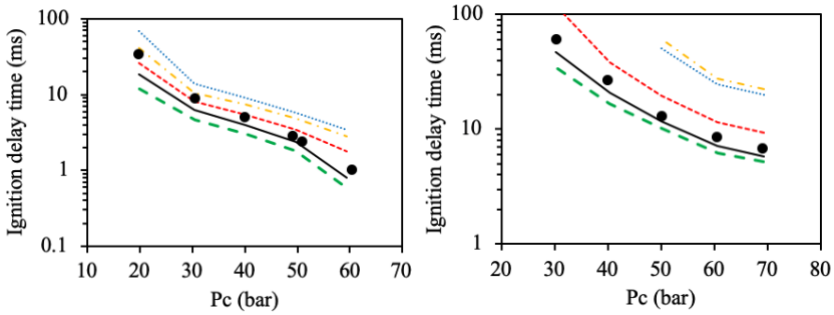

(b) T_c = 1080 K (c) T_c = 1000K

Figure A4.1.3. Measured (circles) and calculated (lines) ignition delay times of NH_3 with 10%CH_4 at $\varphi = 0.5$

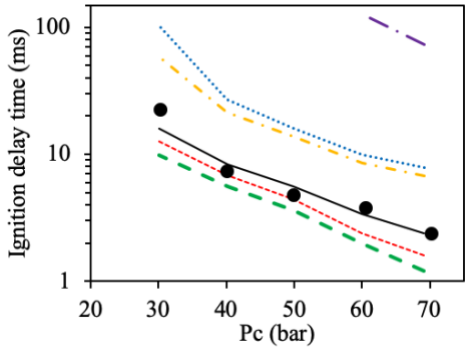

Figure A4.1.4. Measured (circles) and calculated (lines) ignition delay times of NH_3 with 50%CH_4 at $\varphi = 0.5$, Tc = 1000K.

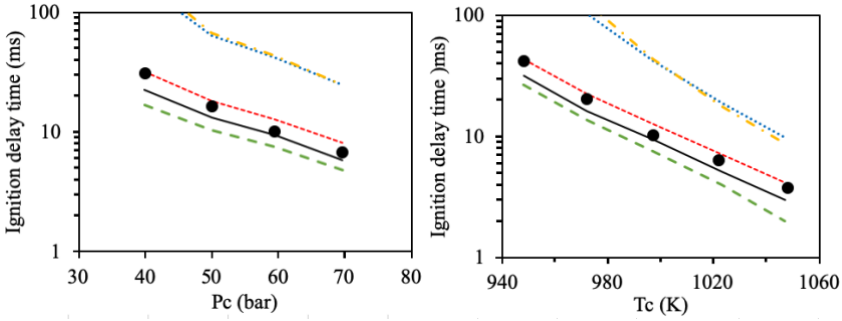

(a) P_c = 60 bar (b) T_c = 1000K

Figure A4.1.5. Measured (circles) and calculated (lines) ignition delay times of NH_3 with 10%CH_4 at $\varphi = 1$

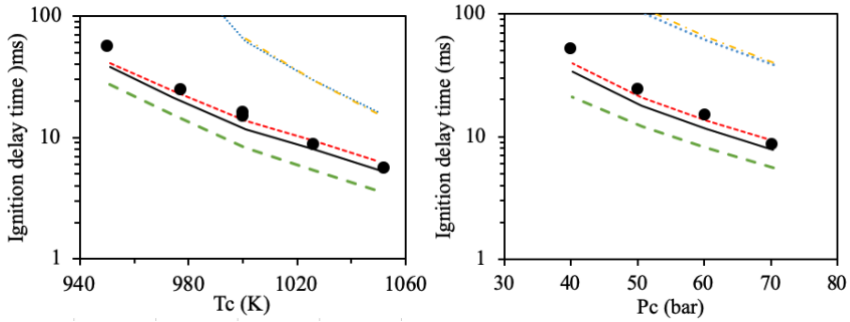

(a) P_c = 60 bar (b) T_c = 1000K

Figure A4.1.6. Measured (circles) and calculated (lines) ignition delay times of NH_3 with 10%CH_4 at $\varphi = 2$.

Appendix 4.2

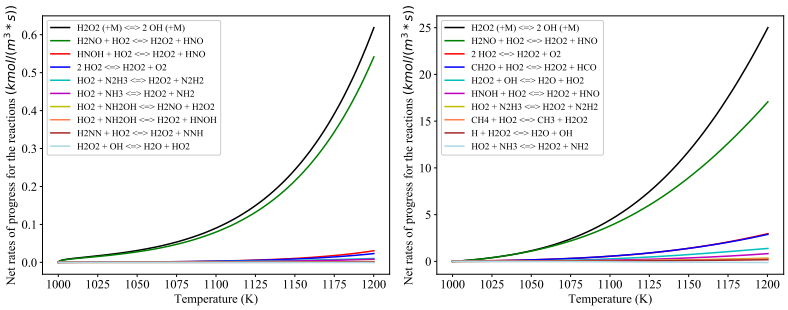

Figure A4.2.1. ROP of H_2O_2 calculated at φ = 0.5, T_c = 1000 K, P_c = 60 bar for pure NH_3 (left) and NH_3 with 50% CH_4 (right)

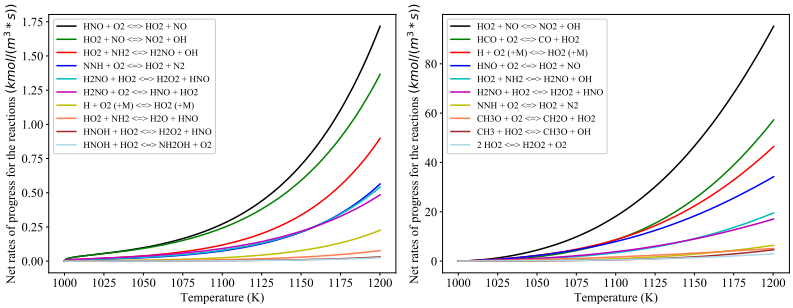

Figure A4.2.2 ROP of HO_2 at φ = 0.5, T_c = 1000 K, P_c = 60 bar for pure NH_3 (left) and NH_3 with 50% CH_4 (right)

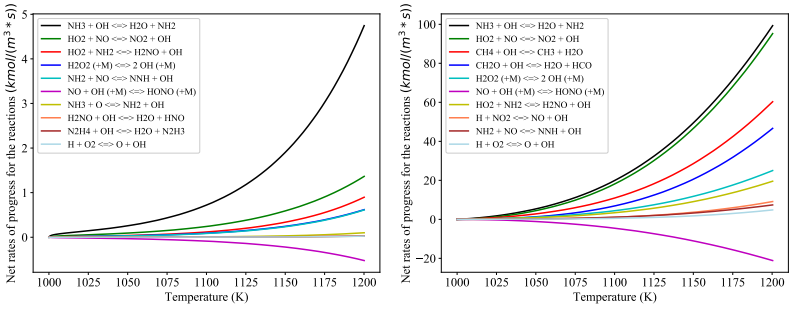

Figure A4.2.3 ROP of OH at φ = 0.5, T_c = 1000 K, P_c = 60 bar for pure NH_3 (left) and NH_3 with 50% CH_4 (right)

Chapter 5: Ignition delay times of NH_3/DME blends at high pressure and low DME fraction: RCM experiments and simulations

This chapter is based on the work presented in: L. Dai, H. Hashemi, P. Glarborg, S. Gersen, P. Marshall, A. Mokhov, H. Levinsky. Ignition delay times of NH_3 /DME blends at high pressure and low DME fraction: RCM experiments and simulations, submitted to Combust. Flame 2020.

5.1. Experimental conditions and mechanism details

To investigate the influence of DME addition on the autoignition behavior of ammonia and to evaluate the performance of a new NH_3/DME mechanism, this chapter presents the ignition delay times of NH_3/DME mixtures measured in the RCM. The measurements were performed at equivalence ratios of 0.5, 1.0 and 2.0, with DME fractions in the fuel of 0, 2%, 5% and 100%, pressures in the range 10 - 70 bar and temperatures from 620 K to 1140 K. The compositions (in mole fraction) of the mixtures examined in detail here are shown in Table 5.1.

Table 5.1. Compositions of NH_3/DME mixtures (unit: mole fraction)

Mixtures	φ	DME/fuel	NH_3	DME	O_2	N_2	Ar	CO_2
Mixture 1*	0.5	0	0.1	0	0.15	0.1	0.65	0
Mixture 2	0.5	2%	0.095	0.002	0.153	0.4	0.35	0
Mixture 3	0.5	5%	0.087	0.005	0.158	0.5	0.25	0
Mixture 4	0.5	100%	0	0.036	0.214	0.45	0	0.3
Mixture 5*	1.0	0	0.143	0	0.107	0	0.75	0
Mixture 6	1.0	2%	0.136	0.003	0.111	0.4	0.35	0
Mixture 7	1.0	5%	0.128	0.007	0.116	0.5	0.25	0
Mixture 8	1.0	100%	0	0.063	0.188	0.45	0	0.3
Mixture 9*	2.0	0	0.182	0	0.068	0	0.75	0
Mixture 10	2.0	2%	0.175	0.004	0.071	0.15	0.6	0
Mixture 11	2.0	5%	0.166	0.009	0.075	0.55	0.2	0
Mixture 12	2.0	100%	0	0.1	0.15	0.65	0	0.1

* Compositions and data taken from Chapter 3

The experimental protocol for using the RCM and method for simulating the results have been described in Chapters 1 and 2. As will be seen below, significant pre-ignition heat release was observed for several of the experimental conditions studied, arising either from two-stage ignition or from a process reminiscent of that observed for t-butanol ignition by Weber and Sung [108]. While the use of the specific volume from the non-reactive pressure trace in this case can result in computed overall ignition delay times that tend to be too short, the magnitude of the resulting discrepancy has been estimated to be less than 30% [109]. As done in other systems showing pre-ignition heat release (for example, [34,35,38,39,109], the same approach is

used here, while cognizant of its shortcomings. For the kinetic analysis, simulations at constant specific volume were performed to avoid the complications in interpretation caused by post-compression heat loss.

The chemical kinetic model used is an updated version of the mechanism proposed in the review of Glarborg et al. [30], as discussed in Chapter 3 [70]. This mechanism was, with minor updates, used successfully in our previous studies of ignition delay of NH_3, NH_3/H_2 and NH_3/CH_4 mixtures described in Chapters 3 and 4 [70,110]. To be useful for DME addition, it was extended to include a DME subset and a subset describing DME/NH_3 interactions. This extension has been performed by H. Hashemi, P. Glarborg and P. Marshall, and is described here for completeness. The DME subset was drawn from the high pressure study of Hashemi et al. [111]. This mechanism did not provide a good description of ignition delays for DME measured in shock tubes and RCMs. For its use in the present work, a few modifications were made to improve its performance. The rate coefficients for thermal dissociation of CH_3OCH_2 to form $CH_2O + CH_3$ was drawn from the recent theoretical study by Gao et al. [112], while for the dissociation of HO_2CH_2OCHO to $OCH_2OCHO + OH$, the rate constant has been multiplied by a factor of two compared to the estimate of Burke et al. [35]. There are no kinetic studies of DME/NH_3 interactions reported in the literature and a kinetic subset was developed. Table 5.2 shows selected reactions in the DME/NH_3 subset. Several classes of reactions are relevant for this interaction

The NH_2 radical may abstract H-atoms from the DME and from stable intermediates formed in DME oxidation. The most important step is the NH_2 + DME reaction,

$$CH_3OCH_3 + NH_2 = CH_3OCH_2 + NH_3. \qquad (R5.1)$$

There are no experimental data available for the rate constant of R5.1. A preliminary estimate was based on the rate constant for the $C_2H_6 + NH_2$ reaction [113]. Modeling predictions of ignition delays under the conditions investigated in this work turned out to be very sensitive the value of k_1. To improve the agreement with experiment, the pre-exponential factor was lowered by a factor of five. More work is desirable on this reaction. Other reactions between NH_2 and stable species include $CH_4 + NH_2$, already

included in the starting mechanism [30] and $CH_2O + NH_2$, drawn from the theoretical study by Li and Lu [114]. The NH_2 radical may also recombine with radicals formed in DME oxidation, primarily

$$CH_3OCH_2 + NH_2(+M) = CH_3OCH_2NH_2(+M) \qquad (R5.2)$$

and $CH_3+NH_2(+M)=CH_3NH_2(+M)$ (which was also part of the mechanism in [30]). The $CH_3OCH_2+NH_2(+M)$ reaction was included with a rate constant similar to $CH_3+NH_2(+M)$. As part of the present work, thermodynamic properties for the $CH_3OCH_2NH_2$ adduct was calculated from ab initio methods and a reaction subset for this component was included in the mechanism. However, the thermal stability of $CH_3OCH_2NH_2$ was too low for this pathway to be important under the conditions investigated. The $CH_3+NH_2(+M)$ reaction forming methylamine had a larger impact on modeling predictions. For this step this study adopted the rate coefficients from Jodkowski et al. [115]; they offer a better extrapolation to high pressure than the shock tube measurements of the reverse step by Votsmeier et al. [116]. The CH_3+NH_2 subset was drawn from the recent work of Glarborg et al. [117]. At high pressure and not too high temperature, formation of CH_3OCH_2OO is from recombination of CH_3OCH_2 and O_2. Internal H-abstraction and subsequent O_2 addition could yield another peroxide, $O_2CH_2OCH_2O_2H$. These peroxides may abstract a hydrogen atom from NH_3, but from analogy with $NH_3 + HO_2$, these steps would be expected to be slow. However, the peroxides would react rapidly with nitric oxide formed from the oxidation of NH_3,

$$CH_3OCH_2OO + NO = CH_3OCH_2O + NO_2 \qquad (R5.6)$$

and

$$O_2CH_2OCH_2O_2H + NO = OCH_2OCH_2O_2H + NO_2. \qquad (R5.7)$$

For both reactions, this study has estimated the rate constant by analogy to CH_3OO+NO. The $OCH_2OCH_2O_2H$ adduct is expected to dissociate rapidly; the formation of $2CH_2O+HO_2$ is tentatively assumed.

Table 5.2. Selected reactions in the DME/NH_3 subset of the reaction mechanism. Rate constants are listed in the form $A*T^N *\exp(-E_a/RT)$. Units are calories, cm^3, mol, second.

Reaction Mechanism		A	N	E_a	Source
R5.1	$CH_3OCH_3+NH_2=CH_3OCH_2+NH_3$	9.0E00	3.460	5600	$k_{C2H6+NH2}/5$
R5.2	$CH_3OCH_2+NH_2(+M)=CH_3OCH_2NH_2(+M)$	7.2E12	0.420	0	$k_{CH3+NH2}$
	Low pressure limit	2.2E30	-3.850	0	
R5.3	$CH_3OCH_2+NO_2=CH_3OCH_2O+NO$	1.1E13	0.000	0	$k_{CH3+NO2}$
R5.4	$CH_3OCH_2OO+NH_3=CH_3OCH_2OOH+NH_2$	3.0E11	0.000	22000	$k_{NH3+HO2}$
R5.5	$CH_3OCH_2OO+NH_2=CH_3OCH_2O+H_2NO$	3.0E13	0.000	0	est
R5.6	$CH_3OCH_2OO+NO=CH_3OCH_2O+NO_2$	1.4E12	0.000	-715	est $k_{CH3OO+NO}$
R5.7	$O_2CH_2OCH_2O_2H+NO=OCH_2OCH_2O_2H+NO_2$	1.4E12	0.000	-715	est $k_{CH3OO+NO}$

It is remarked in passing that, while a preliminary report [118] indicated successful simulations using the ammonia submechanism from GRI-Mech 3.0 [119], coupled to a DME mechanism from [35], GRI-Mech 3.0 fails to show ignition of pure ammonia under the experimental conditions in Chapter 3. Consequently, this mechanism is not considered here.

5.2. Results and discussion

5.2.1. Characteristics of the ignition profile

Three different kinds of ignition behavior were observed in the experiments; examples are shown in Fig. 5.1. "Normal" single-stage ignition (steep pressure increase after the post-compression period) was observed in all pure NH_3 measurements and in part of the measurements on pure DME at high pressures. Two-stage ignition phenomenon were observed in some of the pure DME measurements at low pressures and in NH_3/DME blends at φ =1.0 and 2.0. Further, a pre-ignition pressure rise, a slow rise in pressure over several milliseconds prior to ignition, was reproducibly observed in NH_3/DME blends at φ = 0.5. This phenomenon has been reported previously in the NH_3/CH_4 study in Chapter 4 [110] ,where the pre-ignition was observed at 50% CH_4 with high reproducibility, as observed in [108], in contrast to the reports for NH_3 [17] and ethanol [106], reporting only irregular pre-ignition.

The simulated pressure profiles of NH_3 with 2% DME in the mixture at φ = 0.5 and 1.0 are shown in Fig. 5.2. At φ = 0.5 (Fig. 5.2a), while the computed time of ignition is 18% shorter than the measurement, the simulated pressure follows the experimental slow pre-ignition pressure rise faithfully. It is noted that the mechanism used in [110] failed to predict this phenomenon

for ammonia/methane mixtures. At φ = 1.0 (Fig. 5.2b), the simulated pressure profile also shows pre-ignition heat release, while the measured pressure trace shows two-stage ignition. DME mechanism used in these simulations does predict two-stage ignition for pure DME on the low-temperature side of the NTC region; the low DME fraction combined with ammonia appears to access a region of chemical behavior not well-represented in the mechanism. The role of these phenomena in the effect of DME on ammonia ignition will be discussed in Sec. 5.2.5, below.

Regarding the pre-ignition heat release, assuming that the change in pressure occurs adiabatically, the concomitant increase in temperature from the experimental pressure traces to be roughly 50 K above the initial T_c. Of course, there is also heat loss from the adiabatic core during this period that should be considered in the estimate. For this purpose, the reacting temperature is compared with what would be expected in the absence of heat release, i.e. in the adiabatic core derived from the non-reactive pressure trace (with the caveat described above). The temperature difference between reactive and non-reactive case is roughly 100 K. It is noted that the estimated increase in temperature is roughly the same for both slow pre-ignition pressure rise and from first-stage ignition. As will be discussed in Sec. 5.2.5, pre-ignition heat release is considered as an important part of the ignition process for DME/NH_3 mixtures

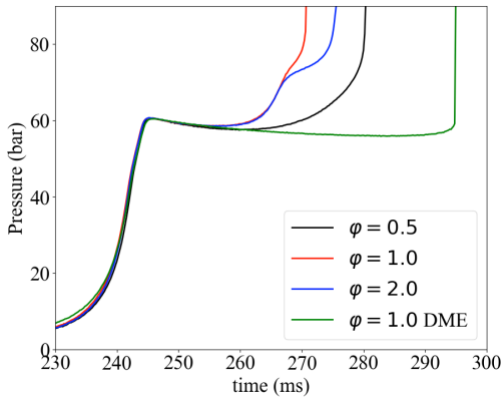

Figure 5.1. Measured pressure traces of NH_3 with 2% DME at T_c = 950 K and P_c = 60 bar. Two-stage ignition is shown at φ= 1.0 and 2.0, slow, pre-ignition pressure rise at φ= 0.5. The curve for DME at φ= 1.0 and 625 K represents "normal" ignition.

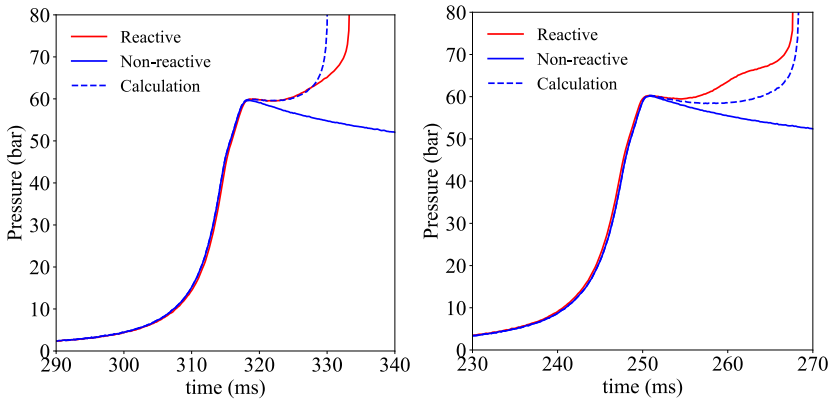

Figure 5.2. Measured and calculated (using the mechanism from this study) pressure traces of the ignition process of NH_3 with 2% DME at P_c=60 bar, T_c=965 K, φ=0.5 (a) and T_c=950 K, φ= 1.0 (b).

5.2.2. Effect of DME fraction

To explore the sensitivity of ammonia ignition to variation in the DME fraction at these low levels, experiments were performed for NH_3/DME mixtures at P_c = 60 bar with DME fractions of 2% (Mixtures 2, 6 and 10 in Table 1) and 5% (Mixtures 3, 7 and 11); the results are shown in Fig. 5.3. For the purposes of comparison, results are also presented for pure ammonia (Mixtures 1, 5 and 9, data taken from Chapter 3) and pure DME (Mixtures 4, 8 and 12, measured here). Both the overall and first-stage ignition delay times decrease monotonically with increasing temperature for all mixtures and conditions. Thus, despite the observation of two-stage ignition, the results do not show evidence of a negative-temperature-coefficient (NTC) region for the range of temperatures studied. DME shows a substantial ignition-enhancing effect on ammonia. For example, at φ = 0.5 (Fig. 5.3a), 2% DME in the mixture reduces the compression temperature T_c at which the overall ignition delay time is ~40 ms from ~1080 K for pure ammonia to ~930 K. Increasing the DME fraction to 5% reduces T_c further to ~830 K, while the pure DME mixtures studied have an ignition delay time of 40 ms at ~ 630 K. These results also indicate the non-linear effect of DME on ignition delay, i.e., that the ignition-enhancing effect of DME decreases at higher DME fraction, which was observed in studies of DME/methanol [38] and DME/n-butane [39]. For comparison, in DME/methanol mixtures [38], roughly 40% DME was needed to effect a reduction in T_c of 150 K to maintain a given ignition

delay time, compared with 2% DME in ammonia. Strong reduction in reaction temperature and the flow-reactor equivalent of two-stage ignition was also reported for small DME fractions in methane at high pressure [111].

Anticipating the analysis in Section 5.2.5, below, this study compares the reduction in T_c necessary to maintain a constant ignition delay time observed here with those reported for admixture of other fuels with ammonia [70,110]. At φ = 0.5 and 60 bar, a fraction of 10% hydrogen in the fuel [70] decreased T_c by ~100 K and 50% methane [110] resulted in a decrease of ~125 K, while 5% DME under the same conditions decreases T_c by ~250 K. Thus, admixture of small fractions of DME enables ignition at temperatures far outside the normal envelope for pure ammonia.

The large shifts in the curves of ignition delay time with temperature make it difficult to compare the changes in ignition delay caused by DME addition directly. Referring to Fig. 5.3a, the overall ignition delay time of the NH_3/DME mixtures is reduced by roughly one order of magnitude when increasing DME fraction from 2% to 5% at φ = 0.5 and T_c= 900 K. A similar effect of DME addition is observed at φ = 1.0 and 2.0. The first-stage ignition delay times are also reduced by an order of magnitude when increasing DME fraction from 2% to 5% for mixtures at φ = 1.0 and 2.0 as shown in Figs. 5.3b and c. The interval between the first stage ignition and overall ignition is more pronounced at higher φ and lower DME fraction. By analogy with other fuels and fuel mixtures (for example, in [37,39,79,120]), the shortening of the first-stage relative to the overall delay time with increasing temperature observed in Fig. 5.3b,c for 2% DME suggests that something resembling an NTC region exists at higher temperatures than those measured here. Since the ignition delay times under these conditions approach 1 ms, shock-tube measurements are indicated to consider this behavior in more detail, as done in [35]. That 2% DME in ammonia (<0.5% DME in the combustible mixture) results in two-stage ignition, while ammonia itself does not show complex ignition behavior, is in our opinion noteworthy and certainly the strong effect for which one hopes when considering the use of an ignition-enhancing “additive”.

As shown in Fig. 5.3, the calculated ignition delay times using the mechanism described above are in good agreement with the measurements for both pure NH_3 and pure DME, with a maximum deviation less than 30% for all conditions. At 60 bar, the mechanism reproduces the trends in the overall ignition delay time with T_c for the NH_3/DME mixtures at all equivalence ratios.

At 2% DME in NH_3, the computations generally agree with the measurements to 50% or better, with a diverging trend with increasing temperature at φ = 1.0 and 2.0; the difference is ~75% at 1025 K and φ = 2.0. At 5% DME, the mechanism predicts a steeper change with temperature than that observed experimentally. At φ = 0.5, the mechanism predicts the measurements better than 10% at the lowest temperature, while progressively diverging (to nearly a factor of 6) at the highest temperature. At φ = 1.0 and 2.0, the discrepancy between calculations and measurements is generally less than 50%. As discussed above and illustrated in Fig. 5.2b, the present mechanism predicts only slow pressure rise under conditions in which two-stage ignition is observed experimentally; as a result, computed ignition delay times for first-stage ignition could not be obtained.

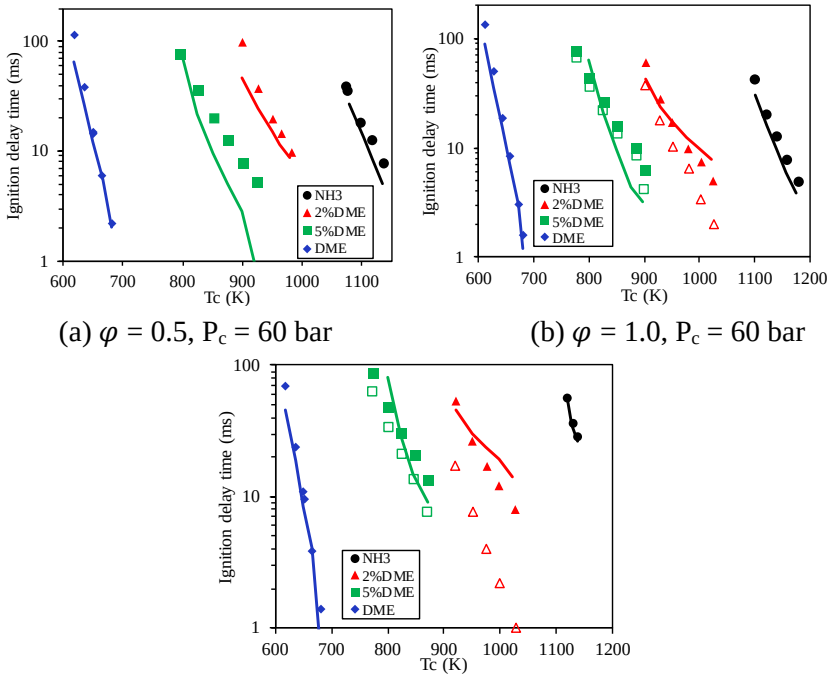

(a) φ = 0.5, P_c = 60 bar

(b) φ = 1.0, P_c = 60 bar

(c) φ = 2.0, P_c=60 bar

Figure 5.3. Measured and calculated ignition delay times of NH_3 with different DME fraction in the fuel mixtures. τ (closed symbols) and τ_1 (open symbols). Note: the error bars of ignition delay times (±5%) are covered by the symbols and thus not visible in the figures.

5.2.3. Effect of equivalence ratio

The measured ignition delay times from Fig. 5.3 are rearranged to expose the effect of equivalence ratio. As discussed in [70] and shown in Fig. 5.4a,

the ignition delay time of pure NH_3 increases with equivalence ratio, by a factor of 2 when φ increases from 0.5 to 1.0 and by another factor of 2 when going from 1.0 to 2.0. At 2% DME in NH_3, Fig. 5.4b, the variation with equivalence ratio has been drastically reduced: the ignition delay times at φ = 0.5 and 1.0 now agree within the experimental uncertainty (less than 5%) at T_c higher than 930 K, while increasing φ from 1.0 to 2.0 increases the ignition delay times by ~50%. Increasing the fraction of DME from 2% to 5%, as seen in Fig. 5.4c, all but erases the variation with equivalence ratio, with the maximum differences being ~30% (φ = 1.0 as compared to at φ = 0.5 and 2.0). The lack of variation resembles the results for pure DME in Fig. 5.4d, which also show only a modest impact of equivalence ratio, with the ignition delay times at φ = 0.5 tending to be somewhat longer (~50%). The trends for pure DME with equivalence ratio observed here at 60 bar are similar to those reported at lower pressures (10-30 bar) by Mittal et al. [37] and Burke et al. [35]

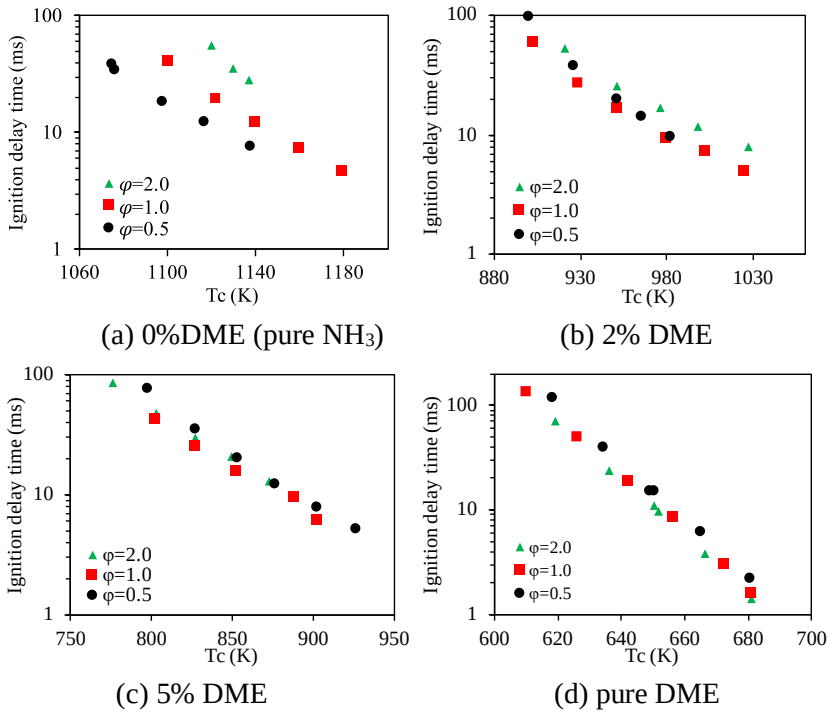

Figure 5.4. Effect of equivalence ratio on the overall ignition delay times (τ) at three DME fractions, pure NH_3, taken from [70] (a), 2%DME (b), 5%DME (c) and pure DME (d). Circles - φ = 0.5, squares – φ = 1.0 and triangles – φ = 2.0.

5.2.4. Effect of pressure

The ignition delay times of NH_3/DME mixtures were measured as function of pressure at φ = 0.5, 1.0 and 2.0. The results at φ = 0.5 and T= 1140, 980, 900 and 680 K for pure NH_3, 2% DME, 5% DME and pure DME, respectively, are shown in Fig. 5.5; the results for φ = 1.0 and 2.0 are shown in the Appendix 5.1.

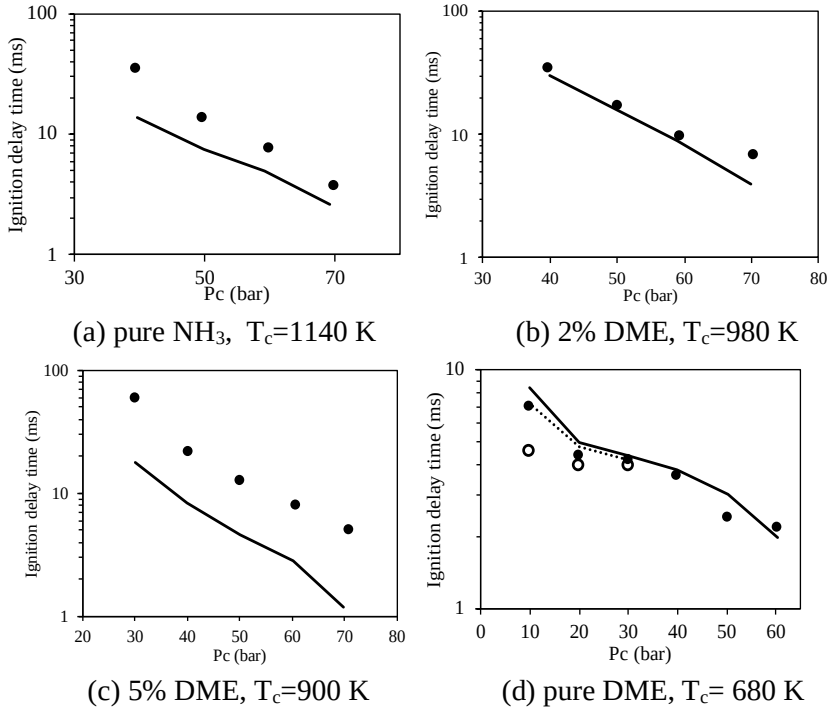

Figure 5.5. Measured (markers) and calculated (lines) ignition delay times at φ = 0.5 for NH_3/DME mixtures of different composition. Open symbols are first-stage delay times; filled symbols are overall times. Solid lines-total ignition delay time, dashed lines – first-stage ignition delay time. Data in Fig. 5.5a are taken from Chapter 3.

Both first stage (at for φ = 1.0 and 2.0) and overall ignition delay times are reduced with increasing compression pressure (P_c). The present mechanism underpredicts the ignition delay times of pure NH_3 by ~40% at high pressure and by a factor of ~2 at low pressure, similar to that observed previously [70]. For 2% DME in NH_3, the calculated ignition delay times generally agree with the measurements to better than 20% at φ = 0.5, generally overpredicting the data at for φ = 1.0 and 2.0 by 50% and 75%, respectively. At 5% DME and φ = 0.5, the mechanism underpredicts the

overall ignition delay times by roughly a factor of 4 (decreasing to a factor of 2 at for φ = 1.0 and 2.0); examination of the data in Fig. 5.3a indicates that fixing the temperature at 900 K for the pressure variation at 5% DME ensures a poorer performance of the mechanism than if a lower temperature had been chosen. The mechanism predicts the overall ignition delay times of pure DME to better than 20%, although it overpredicts the first-stage ignition delay time by a factor of 2 at P_c = 10 bar. It is also noted that the appearance of two-stage ignition in pure DME at pressures below 40 bar, consistent with earlier measurements [37]. Given the lengthening of the first stage relative to the overall ignition delay time shown in Fig. 5.5d, it is expected to be indistinguishable from the overall delay at higher pressures.

Temperature-dependent ignition delay times at 20 and 40 bar for φ = 1.0 and 5% DME (shown in the Appendix 5.1) have similar trends as at 60 bar. Here it is noted that the first stage of ignition is shorter at 20 bar, as compared to the overall delay time. In contrast with the results in Fig. 5.5c, the mechanism substantially overpredicts the ignition delay time at 20 bar.

5.2.5. Kinetic analysis and the impact of DME on ammonia ignition

To gain more insight into the experimental observations on the effect of DME on ammonia ignition at P_c=60 bar, the kinetics and mechanism of the oxidation process are investigated. Here, the focus is on the conditions at φ = 0.5 in detail, where the simulations reproduce the slow pressure rise for the DME/NH_3 mixtures in the experiments. Despite the inability of the mechanism to predict two-stage ignition in the DME/NH_3 mixtures, the model reproduces the overall ignition delay times well at other equivalence ratios. A brief discussion of the kinetics at other equivalence ratios provides insight into the ignition enhancement by DME, as well as into the behavior of the mechanism. Since the analysis of the mechanisms responsible for the ignition of both ammonia [13,22,24,70,110] and DME [34–37] have been discussed in detail elsewhere, it will not be repeated here.

5.2.5.1. Reaction path of NH_3/DME mixtures and sensitivity analysis

Following the methods described in the ignition literature ([24,35,70,108,110] and elsewhere), the reaction path at 20% fuel consumption is examined. The relative changes in the fractions of NH_3 and DME, together with the mixture temperature, are illustrated in Fig. 5.6 (2%

DME, φ = 0.5, T_c= 950 K, P_c=60 bar). It is first observed that the consumption of the fuel, particularly DME, starts long before ignition, with DME oxidation beginning in the initial milliseconds. At 20% consumption of the total fuel fraction, nearly 90% of the DME has been consumed. A similar early decomposition of DME was also observed in DME/CH_4 mixtures in a flow reactor [111]. As will be discussed below, the early oxidation of DME plays an important role in initiating the oxidation at temperatures well below that at which neat ammonia ignites on the timescale of the experiments. Figure 5.6 shows that the temperature begins to increase noticeably within the first milliseconds. To gain insight into the apparently phased oxidation of the fuel mixture, it is illustrative first to consider the reaction path for DME in the mixture at 20% DME consumption. The reaction path for ammonia in the DME mixtures studied here shows only modest changes from that reported previously for pure ammonia [70,110]. Since the ammonia fraction at 2% DME and 5% DME is 49 and 19 times higher, respectively, than that of DME, this is to be expected. In contrast, the direct participation of nitrogen-containing species in the oxidation of DME will be seen to have a substantial impact on both the reaction path of DME and the ignition process.

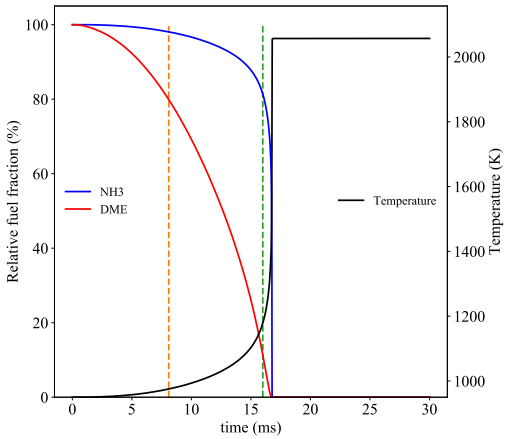

Figure 5.6. Profiles of relative fractions of DME and NH_3, and the temperature. Conditions: 2% DME, φ = 0.5, T_c = 950 K, P_c = 60 bar. Dashed vertical lines indicate: 20% DME consumption (orange) and 20% total fuel consumption (green).

The reaction path of 2% DME in ammonia at φ = 0.5, T_c = 950 K, P_c = 60 bar is shown in Fig. 5.7. At 20% DME consumption, roughly 2% of the ammonia has reacted and the mixture temperature T has risen to 975 K.

Anticipating the discussion of heat release below, recall that the 2% ammonia that is consumed is twice the number of molecules as the 20% DME, together causing a 25 K rise in temperature, even at this early stage in the ignition process. As seen in Fig. 5.7, DME is converted to CH_3OCH_2 primarily by reaction with OH and, interestingly, with NH_2 through reaction R5.1, above. While half of the CH_3OCH_2 is oxidized via dissociation to CH_3+CH_2O or by reaction with O_2 [111] to produce $2CH_2O$+OH (with more or less equal rates), the current mechanism predicts that half is oxidized through the low-temperature sequence [111] indicated in Fig. 5.7: reaction of CH_3OCH_2 with O_2 to form CH_3OCH_2OO, isomerization to CH_2OCH_2OOH, oxygen addition to produce $O_2CH_2OCH_2O_2H$, followed by the chain-branching sequence $O_2CH2OCH2O_2H \rightarrow HO_2CH_2OCHO \rightarrow OCH_2OCHO$ producing two OH radicals. Thus, the mechanism indicates substantial low-temperature chemistry, despite a mixture temperature of 975 K. The analysis shows that the presence of ammonia results in opening the channel from CH_3OCH_2OO to CH_3OCH_2O, by NH_2 and NO (via reactions R5.5 and R5.6 in Table 1). The CH_3OCH_2O is ultimately converted to methyl formate (CH_3OCHO) [111]; while this species is not oxidized further at this point in time, it is ultimately converted to CH_3OCO, which dissociates to CH_3 and CO_2, and CH_2OCHO, which then reacts to CH_2O and HCO.

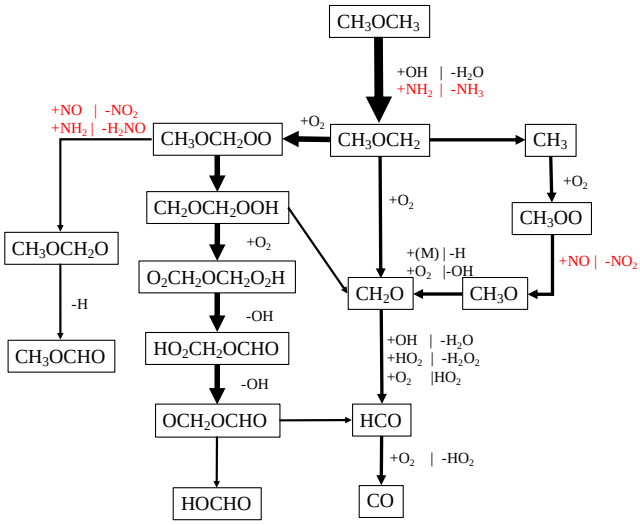

Figure 5.7. Reaction path diagram of DME in mixture with 2%DME in the fuel at φ = 0.5, T_c= 950 K, P_c = 60 bar at the moment of 20% DME consumption. Species in red denote nitrogen-containing reaction partners and products. The thickness of the arrows are roughly proportional to the flux in the individual steps.

Increasing the DME fraction to 5% of the fuel under the same conditions of φ, T_c and P_c, where 20% oxidation of the DME has resulted in T=983 K, gives nearly an identical path to that in Fig. 5.7. With the exception of slightly more of the DME being converted to CH_3 and CH_2O, the mechanism predicts an increase in the fraction of CH_3OCH_2OO being converted to methyl formate, from 10% at 2% DME to 15% at 5% DME. Noteworthy is that reactions involving nitrogen-containing species (specifically, NO, H_2NO and NO_2) are involved in the oxidation of CH_3 and CH_3OO, as observed in NH_3/CH_4 mixtures [110].

As shown in Fig. 5.3, above, increasing the DME fraction from 2% to 5% has such a large effect on the ignition delay time that the entire curve is shifted to lower temperatures. Consequently, it is illustrative to consider the different DME fractions at different temperatures, where they have comparable delay times. This comparison also mirrors the discussion derived from flow reactor data [111]. The reaction path for 5% DME at T_c=850 K is contrasted with that of 2% DME at 950 K, where the ignition delay time is comparable (~20 ms). At 20% DME consumption (where 2.5% of the ammonia has reacted and heat release has increased the mixture temperature to T=893 K) shows that, while the overall oxidation route is similar to that at T_c=950 K, now ~86% of the methoxymethyl reacts via oxygen addition to CH_3OCH_2OO (compared to 50% at T_c=950 K), of which 55% now proceeds through CH_2OCH_2OOH, while 45% reacts with NH_2 and NO (as noted above) to CH_3OCH_2O and further to methyl formate.

At 20% total fuel consumption, the reaction path has shifted considerably, as shown in Fig. 5.8. For 2% DME at T_c=950 K, where the mixture temperature is now 1178 K, the path via CH_3OCH_2OO has all but disappeared, with all the CH_3OCH_2 being oxidized via dissociation or reaction with O_2 to form two formaldehyde molecules and a hydroxyl radical, both accounting for half the consumption of the methoxymethyl radical. At this higher mixture temperature, the oxidation of the methyl radical is now dominated by nitrogen-containing species: the mechanism indicates that roughly 40% is oxidized via $CH_3 \rightarrow CH_3O$, predominantly by H_2NO and NO_2, followed by CH_3O (+M) $\rightarrow$ CH_2O+H (+M), while 60% of the methyl radical recombines with NH_2 to form CH_3NH_2. This species reacts further along the route: $CH_3NH_2 \rightarrow CH_2NH_2 \rightarrow CH_2NH \rightarrow H_2CN/HCNH \rightarrow HCN$. At 5% DME ($T_c$=950 K; at 20% fuel consumption T=1171 K), the path and branching

ratios are nearly identical, with the exception of a significant side-path from CH_3 to CH_3O; ~25% of the CH_3 reacts (reversibly) with O_2 to form CH_3OO, which is further oxidized to CH_3O by NO (99%). At 5% DME and T_c=850 K (T=1086 K at 20% fuel consumption), the computations show 14% of the methoxymethyl radical still being oxidized through CH_3OCH_2OO. Of this, ~40% is predicted to be converted to methyl formate, as described above.

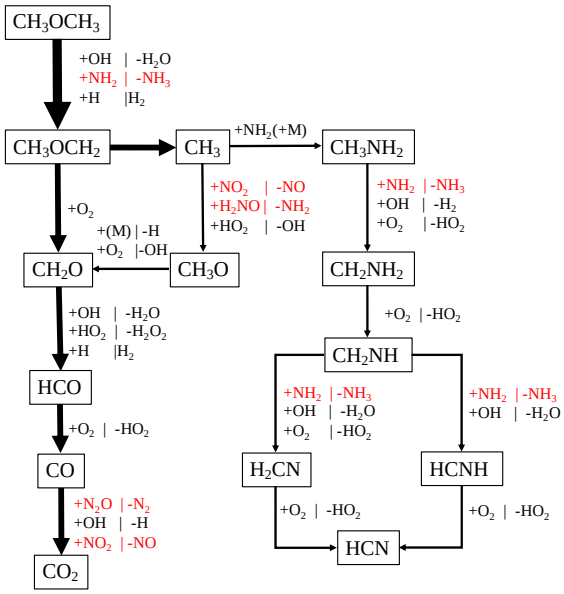

Figure 5.8. Reaction path diagram of DME in mixture with 2%DME in the fuel at φ = 0.5, T_c=950 K, P_c=60 bar at the moment of 20% total fuel consumption. Species in red denote nitrogen-containing reaction partners and products. The thickness of the arrows are roughly proportional to the flux in the individual steps.

The reaction paths at φ = 1.0, T_c=950 K, P_c=60 bar, at both 20% DME and 20% total fuel consumption, show no new features as compared to those at φ = 0.5 discussed above, with the exception of a significant amount of methane at 20% fuel consumption; this is formed from the methyl radical produced from the thermal dissociation of methoxymethyl. However, the reactions of methoxymethyl favor the routes to CH_3 and CH_2O at the expense of the low-temperature route. At 20% DME consumption, for 2% and 5% DME at T_c=950 K, the lower oxygen fraction at φ = 1.0 results in ~35% less $O_2CH_2OCH_2O_2H$ being formed than at φ = 0.5, arising primarily from higher oxygen requirement (two oxygen molecules) for its formation from methoxymethyl, as compared to CH_2O (one O_2) and CH_3 (none). This shift is smaller (~25% less $O_2CH_2OCH_2O_2H$) for 5% DME and T_c=850 K. At φ = 2.0,

this shift towards methane and formaldehyde as dominant intermediates continues. At this equivalence ratio, the computations predict that there is substantial residual ammonia after ignition.

The importance of the low-temperature route in the two-stage ignition of DME [34] suggests that reconsideration of the rates leading to the distribution of products arising from methoxymethyl, and of the ammonia-specific reactions diverting CH_3OCH_2OO from the low-temperature chain-branching reactions (resulting in methyl formate as described above), may improve the mechanism's ability to predict two-stage ignition under the conditions studied here. However, given the very low fractions of DME in the reactive mixture, the possibility that other cross reactions between DME and ammonia species could also be the origin of two-stage ignition cannot be ruled out.

Regarding the reaction path of ammonia, whose major fluxes at 20% fuel consumption are nearly identical to those of pure ammonia under the conditions of pressure, temperature and equivalence ratio at which it ignites [70,110], it is observed that the vast majority of the reactions with C-containing species are only a few percent of the flux at any given point. As observed for the admixture of hydrogen [24,70] and methane [110], the major reactions for production of the species relevant for oxidation and ignition of ammonia with DME, i.e., OH, HO_2 and H_2O_2, do not change dramatically, but their rates do. This is illustrated in Fig. 5.9, which shows the ROP for OH production for pure ammonia and 5% DME at $\varphi = 0.5$, P_c=60 bar and T_c=950 K (ROPs for HO_2 and H_2O_2 at these and other conditions are shown in appendix 5.2).

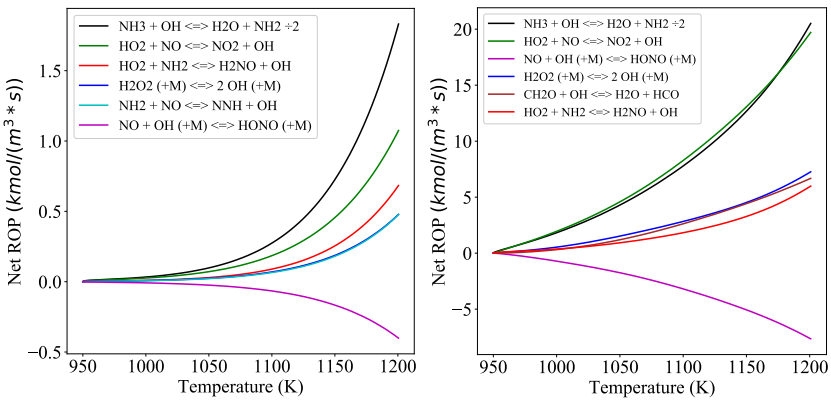

Figure 5.9. Rate-Of-Production analysis for OH production for pure ammonia (left) and 5% DME (right) at φ= 0.5, P_c=60 bar and T_c=950 K. Note that the rate for NH_3+OH has been divided by 2.

The ROP shows that the dominant reactions for OH production in the pre-ignition period (taking the trajectory between T_c and 1200 K for this purpose [110]), $HO_2+NO \rightarrow OH+NO_2$, $HO_2+NH_2 \rightarrow H_2NO+OH$ and H_2O_2 (+M)$\rightarrow$2OH (+M), remain dominant for DME admixture, but increase much more rapidly with temperature than in neat NH_3. This points to the importance of DME oxidation for initiating ammonia decomposition. At 1200 K, 5% DME in the fuel increases the rates of these reactions by a factor of 10-20. The magnitude of the increases in rate at 5% DME observed here are similar to those seen for 50% methane in ammonia [110]. Nearly all the OH is consumed by $NH_3+OH \rightarrow NH_2+H_2O$, keeping the OH fraction very low in until ignition.

The sensitivity analysis for ignition delay time, based on the mechanism presented here, is shown in Fig. 5.10 for the three sets of conditions described above. At both 2% and 5% DME four of the most important reactions are identical to those of pure ammonia at 1000 K reported previously [110], all involving NH_2 and NO/NO_2. The most striking effect of DME admixture on the sensitivity is the introduction of two reactions that compete for OH: the enhancing reaction $CH_3OCH_3+OH \rightarrow CH_3OCH_2+H_2O$, initiating the decomposition of DME, and $NH_3+OH \rightarrow H_2O+NH_2$ that inhibits ignition. At 5% DME and T_c=850 K, these reactions dominate the sensitivity. While the ROP, above, indicates that NH_3+OH is always the dominant pre-ignition OH-consuming reaction, this reaction does not occur in previous sensitivity analyses for pure NH_3 at temperatures extant in an RCM [24,70,110]. This competition underlines the importance of OH for promoting ignition by initiating the decomposition of DME. The parallel step for decomposing the fuel, by $CH_3OCH_3+NH_2 \rightarrow CH_3OCH_2+NH_3$, shows substantial sensitivity as stated in Section 5.1 above, but is relatively insensitive to the DME fraction in the fuel. Further, it is observed that three reactions that have been identified as dominant reactions in the sensitivity analysis for pure DME [32]. The inhibiting reactions $CH_3OCH_2 \rightarrow CH_2O+CH_3$ and $CH_2OCH_2OOH \rightarrow 2CH_2O+OH$ compete with $CH_2OCH_2OOH+O_2 \rightarrow O_2CH2OCH2O_2H$, which leads to low-temperature chain branching as discussed above. The dissociation of hydrogen peroxide shows substantially larger contribution to the sensitivity than for pure ammonia reported previously [24,70,110]. A noteworthy result is that the reaction $CH_3OCH_2OO+NO \rightarrow CH_3OCH_2O+NO_2$, which was seen above to be an important diversion from isomerization to CH_2OCH_2OOH and the further chain-branching reactions, reaches 20%

sensitivity for 5% DME at 850 K, also pointing to the importance of the low-temperature path for ignition under these conditions. Despite the very low fraction of DME in the fuel, it is striking that reactions related to DME oxidation, and particularly those related to low-temperature chain branching, show such relative importance for the ignition delay time in ammonia mixtures. A similar observation on the importance of DME chemistry has been made regarding the effect of DME addition on methane ignition [35], but at DME fractions that are 4-10 times higher than those considered here.

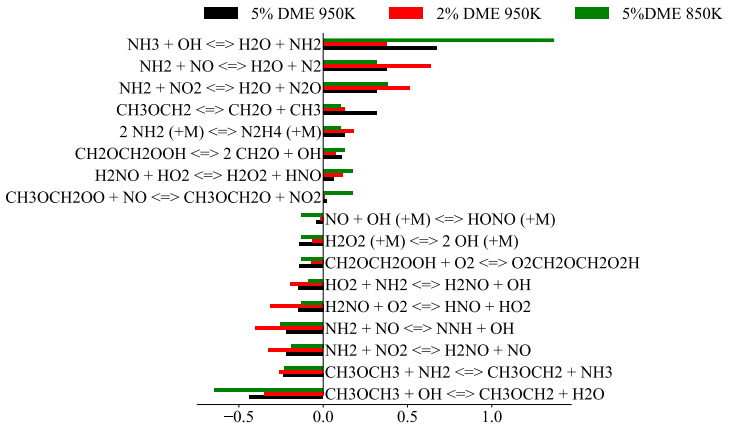

Figure 5.10. Sensitivity analysis for ignition delay time of DME/NH_3 mixture at P_c=60 bar and φ = 0.5, for 2% DME at T_c=950 K and 5% DME at T_c=950 and 850 K.

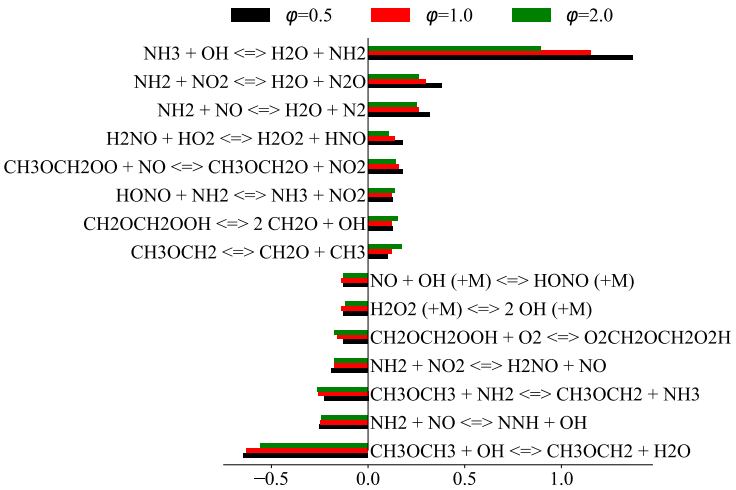

Figure 5.11. Sensitivity analysis of NH_3 with 5% DME at T_c=850 K, P_c=60 bar, and φ = 0.5, 1.0 and 2.0.

The changes in the sensitivity analysis upon varying the equivalence ratio are illustrated in Fig. 5.11, for 5% DME at P_c=60 bar, T_c=850 K and φ = 0.5, 1.0 and 2.0. With the exception of the minor decrease in the sensitivity of the ignition delay time to $NH_3+OH \rightarrow H_2O+NH_2$, there is essentially no change to the important reactions as a function of equivalence ratio. Given that the measured overall ignition delay time has been seen to be nearly insensitive to equivalence ratio (Fig. 5.4c) and that under these conditions the experimental results are well predicted by the mechanism used here, the sensitivity analysis suggests that there is no substantial change in the identity of the dominant reactions that maintain the ignition delay time upon decreasing the oxygen fraction in the fuel.

5.2.5.2. Species profiles and heat release

Having discussed the dominant oxidation paths of the fuel components and identified the important reactions above, the way in which DME accelerates ammonia ignition is now considered. The computed species and heat-release time histories for 5% DME in ammonia, T_c=850 K, P_c=60 bar, and φ = 0.5 in Fig. 5.12, below are used for this purpose. The two vertical dashed lines indicate 20% DME consumption at 893 K and 20% total fuel consumption at 1086 K, as indicated above. In the discussion of the promoting effects of H_2 [70] and CH_4 [110] on ammonia ignition, an orders-of-magnitude increases in pre-ignition fractions of H_2O_2 (as well as HO_2) is observed as compared to pure ammonia under the same conditions. Comparing the H_2O_2 fraction in Fig. 5.12a, the peak of this species for 5% DME in ammonia is as large as that for 50% methane, implying a substantial "reservoir" of OH caused by a modest fraction of additive. At 2% DME, the peak H_2O_2 fraction is proportionally lower for the same conditions of temperature and pressure.

As reported in Chapters 3 and 4 [70,110], Fig. 5.12a bears a strong resemblance to the description of the intermediate-temperature ignition of hydrocarbons [53], where the rapid decomposition of H_2O_2 in the region close to 1000 K results in concomittant OH production, rapid fuel consumption and ignition. It is important to recall here that, while the magnitude of the peak H_2O_2 fraction at 5% DME is similar to that of 50% methane or 10% hydrogen, T_c for DME in Fig. 5.12 is 150 K lower than that for methane and 230 K lower than hydrogen for the same P_c and φ. Figure 5.12a shows that the fraction of H_2O_2 grows slowly from ~850 K (T_c) to its peak value at ~965 K, after which

it declines rapidly. The ROP for H_2O_2 under these conditions is given in Fig. 5.13 and shows that $H_2NO+HO_2 \rightarrow H_2O_2+HNO$ is the dominant reaction producing hydrogen peroxide, with the rate of decomposition exceeding formation above this temperature. Significant heat release is needed to raise the mixture temperature to the point at which H_2O_2 decomposes; in the current example by ~115 K. In hydrocarbon ignition at intermediate temperatures [53], first-stage ignition serves this purpose. As described in Section 5.2.1, above, while at φ = 1.0 and 2.0, first-stage ignition in DME/NH_3 mixtures increases the temperature, the pre-ignition heat release at φ = 0.5 performs the same function.

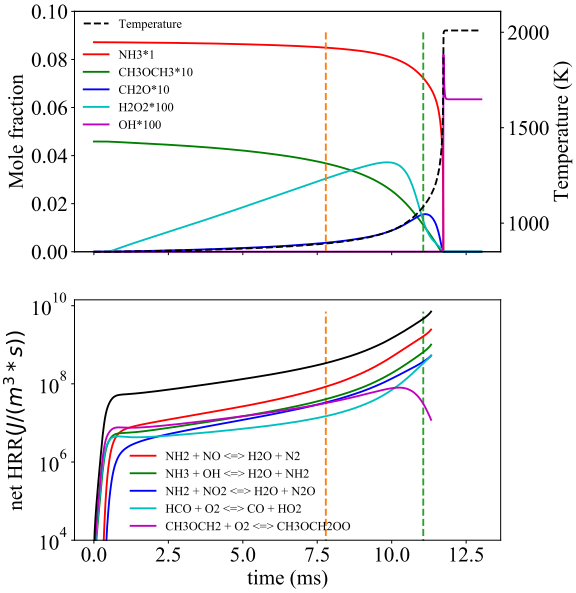

Figure 5.12. Computed time histories of selected species and temperature (a) and net heat release rate (HRR) (b). The vertical dashed lines indicate 20% DME consumption at 893 K (orange) and 20% total fuel consumption at 1086 K (green). Conditions: 5% DME, T_c=850 K, P_c=60 bar, φ = 0.5. The heat release curves are computed up to 1200 K.

The heat release between T_c and 1200 K is given in Fig. 5.12b, for the total heat release and the heat release from a number of the most important contributing reactions. In the first millisecond, the reactions $CH_3OCH_2+O_2 \rightarrow CH_3CH_2OO$, $NH_3+OH \rightarrow H_2O+NH_2$ and $HCO+O_2 \rightarrow CO+HO_2$ generate the most heat. The contribution from these reactions is rapidly equaled or overtaken by $NH_2+NO_2 \rightarrow H_2O+N_2O$ and $NH_2+NO \rightarrow H_2O+N_2$, with the latter reaction dominating the heat release by a factor of 2. Obviously, the contribution from the reaction of methoxymethyl

with oxygen decreases rapidly after the point of 20% fuel consumption, since the DME then becomes depleted. Also, the rapid rise of $HCO+O_2$ starting at ~10 ms corresponds with the formation of the peak in the CH_2O history shown in Fig. 5.12a. With the exception of $CH_3OCH_2+O_2$, the major heat-releasing reactions in the pre-ignition period are from ammonia oxidation itself. A somewhat paradoxical observation is that the three of the major heat-releasing reactions are also the three most important ignition-inhibiting reactions shown in the sensitivity analyses in Figs. 5.10 and 5.11, above. While the heat release is clearly necessary to accelerate the reactions leading to ignition, kinetically, these reactions appear to retard ignition.

Preliminary examination of the origin and effect of heat release at other equivalence ratios indicates similar phenomena (including the strong buildup of H_2O_2); however, the fact that the heat release under these conditions arises from first-stage ignition, which the mechanism does not yet predict properly, dissuades further analysis.

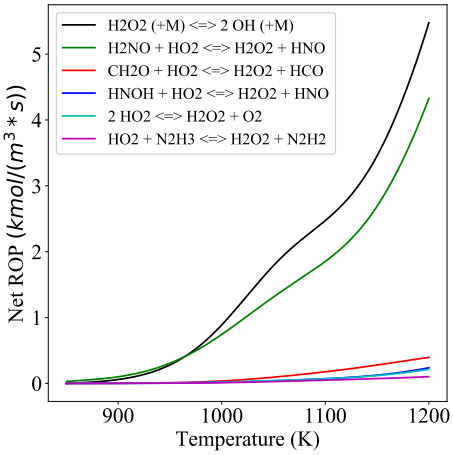

Figure 5.13. ROP for H_2O_2. Conditions: 5% DME, T_c=850 K, P_c=60 bar, φ = 0.5.

While the discussion above indicates the importance of enhanced H_2O_2 formation and oxidation generated by DME admixture, the ROP also shows that decomposition of the hydrogen peroxide "reservoir" is not the entire cause of ignition enhancement. As shown in Fig. 5.13, decomposition of H_2O_2 is only slightly faster than $H_2NO+HO_2 \rightarrow H_2O_2+HNO$; the ROP indicates that, even up to 1400 K, H_2O_2 continues to be formed as fast as it is consumed, with a strongly increasing rate with temperature. Therefore, H_2O_2 is rather a

steady supplier of OH radicals in the period leading to ignition. Perhaps more importantly, other reactions are larger suppliers of OH than H_2O_2 decomposition. As seen in Fig. 5.9, above, $HO_2+NO \rightarrow NO_2+OH$ supplies 50% more OH at 1200 K than H_2O_2 decomposition. Thus, while chain branching from the decomposition of H_2O_2 is an important contribution to the ignition process, rapid OH formation in the ammonia system itself is equally important.

These results imply that the early oxidation of low fractions of DME generates reactive species, particularly HO_2 and OH, which initiate ammonia oxidation. This, in turn, causes substantial pre-ignition heat release, and consequently greatly accelerates the ignition process compared to neat ammonia. The acceleration facilitated by 2-5% DME allows rapid ignition at temperatures after compression that are hundreds of degrees lower than that for ammonia without DME addition.

5.3. Summary and Conclusions

At high pressure, very low fractions of DME admixed with ammonia (2-5% in the fuel) shorten the ignition delay time by more than an order of magnitude. These low fractions effectively shift the curves of ignition delay time vs. temperature at constant pressure. At a constant ignition delay time, 2% DME shifts the ignition curve by ~150 K, while 5% DME shifts the curve by roughly 250 K. Thus, DME admixture allows ignition of the ammonia-based fuel at temperatures far removed from those at which neat ammonia would ignite at the same pressure. This property makes it potentially attractive as a combustion-enhancing additive for ammonia as a fuel. Two-stage ignition is observed at P_c=60 bar and φ=1.0 and 2.0 with 2% and 5% DME in the fuel, despite the very low DME fraction in the combustible mixture (<1%) and the pressure being higher than that at which pure DME shows two-stage ignition. At φ=0.5, a reproducible pre-ignition pressure rise is observed for both DME fractions, which is not observed in the pure fuel components. The equivalent heat release of the first-stage ignition and the slow pressure rise are both roughly 100 K as compared to the temperature that would exist in a non-reactive mixture. This rise in temperature is seen to be an important aspect of the ignition-enhancing effect of DME on ammonia.

The chemical mechanism presented here, which contains several new reactions describing interaction between DME and ammonia species, captures the pre-ignition slow temperature rise faithfully, but does not predict 2-stage

ignition for the ammonia/DME mixtures. The overall ignition delay times are predicted well, generally being within 50% of the experimental values. Simulating the ignition process using the mechanism, it is observed that the DME is oxidized much more rapidly than ammonia, with ~90% of the DME being already oxidized at the time at which 20% of the total fuel (DME+NH_3) has been consumed. Analysis of the mechanism indicates that this 'early DME oxidation' generates reactive species that initiate the oxidation of ammonia, which in turn begins heat release, further accelerating the oxidation process, resulting in ignition. The reaction path analysis shows that the low-temperature chain-branching reactions of DME are important in the early oxidation of the fuel. The sensitivity analysis shows further that several of these reactions of DME are critical to ignition, even at fractions of 2% in the fuel. Regarding the mechanism, the analysis shows that reactions with products of ammonia oxidation divert significant fractions of CH_3OCH_2OO away from the low-temperature chain-branching reactions to form methyl formate. Re-examination of the distribution of products arising from methoxymethyl, and of the ammonia-specific reactions involving CH_3OCH_2OO or other species derived from DME, may improve the mechanism's ability to predict two-stage ignition under the conditions studied here.

Appendix 5.1

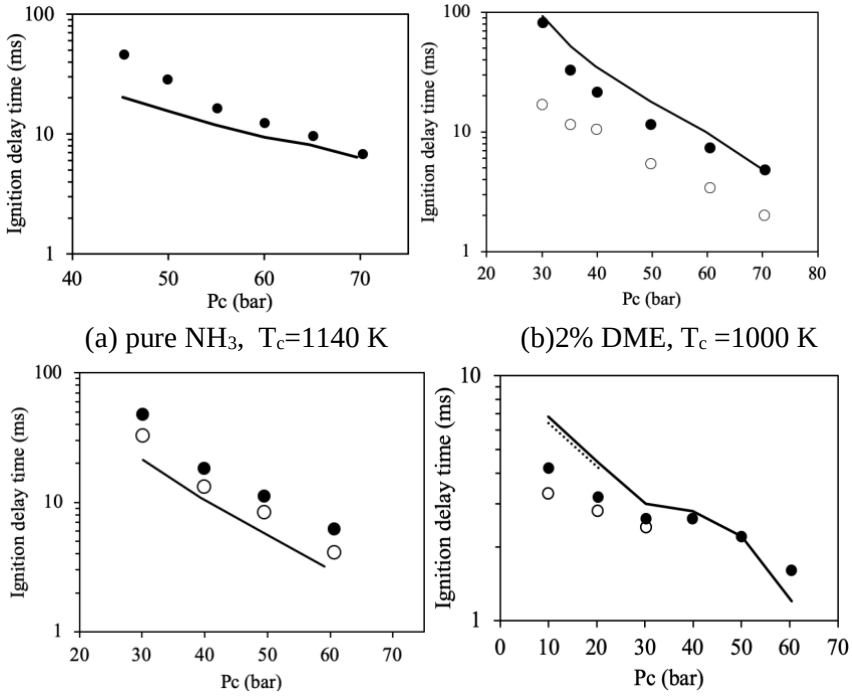

(a) pure NH_3, T_c=1140 K (b)2% DME, T_c =1000 K

(c) 5 %DME, T_c =900 K (d) pure DME, T_c = 680 K

Figure S5.1. Measured (markers) and calculated (lines) ignition delay times at φ = 1.0 for NH_3/DME mixtures of different composition. Open symbols are first-stage delay times; filled symbols are overall times. Solid lines-total ignition delay time, dashed lines – first-stage ignition delay time. Data in Fig. S1a are taken from [70].

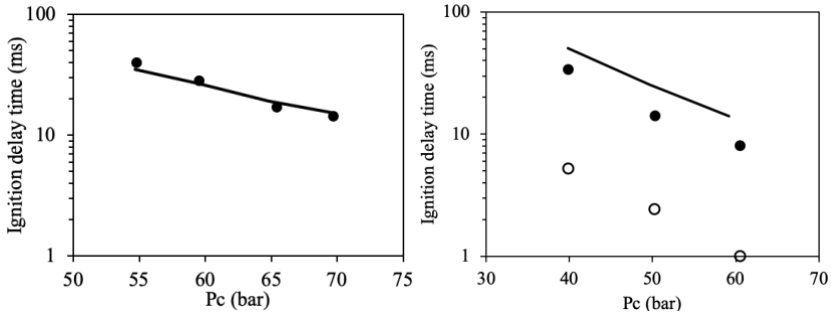

(a) pure NH_3, T_c=1140 K (b)2% DME, T_c=1025 K

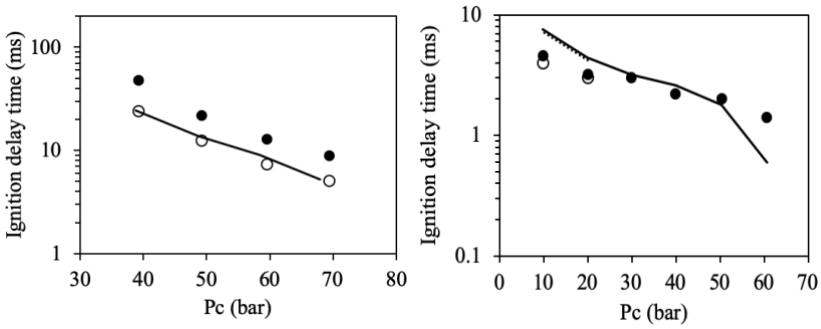

(c) 5 %DME, T_c=875 K (d) pure DME, T_c= 680 K

Figure S5.2. Measured (markers) and calculated (lines) ignition delay times at φ = 2.0 for NH_3/DME mixtures of four different compositions. Open symbols are first-stage delay times; filled symbols are overall times. Solid lines-total ignition delay time, dashed lines – first-stage ignition delay time. Data in Fig. S2a are taken from Chapter 3.

2. Temperature-dependent ignition delay times at 20 and 40 bar for φ = 1.0 and 5% DME

*The inert composition used in the measurements at φ = 1.0 and 5% DME, P_c= 20 and 40 bar is 10%N_2 and 65%Ar, which is different from that at P_c=60bar (50%N_2 and 25%Ar) as presented in Table 5.1.

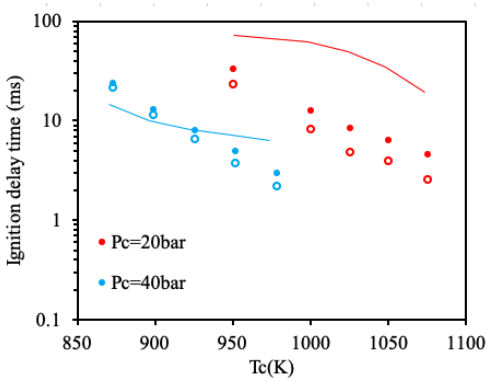

Figure S5.3. Measured and calculated ignition delay times of mixture at φ = 1.0 and 5% DME, P_c= 20 and 40 bar. (The mixture contains 10%N_2 and 65%Ar, which is different from that at P_c=60bar as presented in Table 5.1),. τ (closed symbols) and τ_1 (open symbols). Note: the error bars of ignition delay times (±5%) are covered by the symbols and thus not visible in the figures.

Appendix 5.2

*All ROPs are performed using CONV at P_c= 60 bar, diluted by 75% N_2

φ **= 0.5**

ROP of HO_2

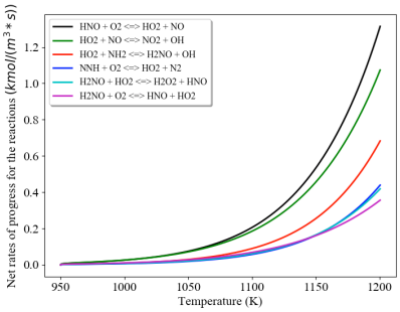

Pure NH_3 T_c = 950 K

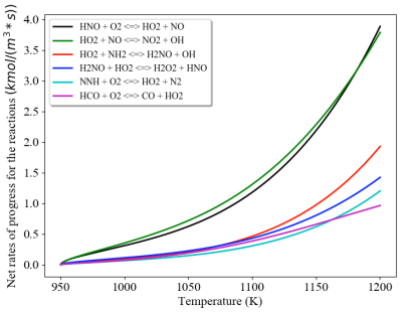

NH_3 with 2%DME T_c = 950 K

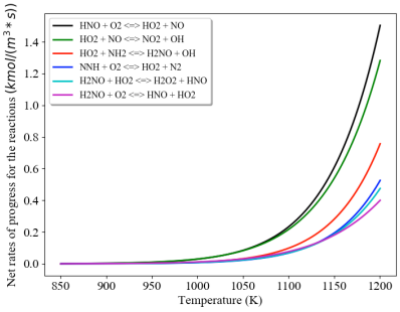

Pure NH_3 T_c = 850 K

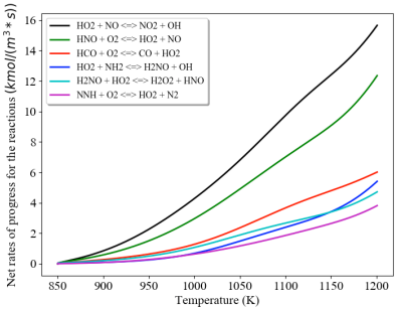

NH_3 with 5%DME T_c = 850 K

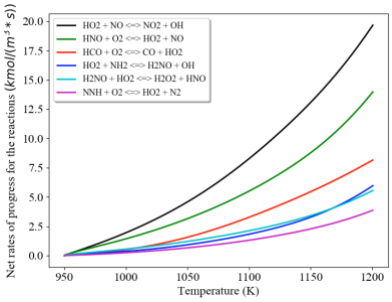

NH_3 with 5%DME T_c = 950 K

ROP of H_2O_2

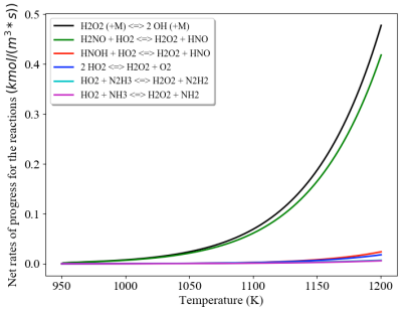

Pure NH_3 T_c = 950 K

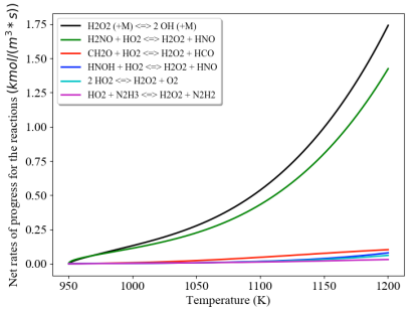

NH_3 with 2%DME T_c = 950

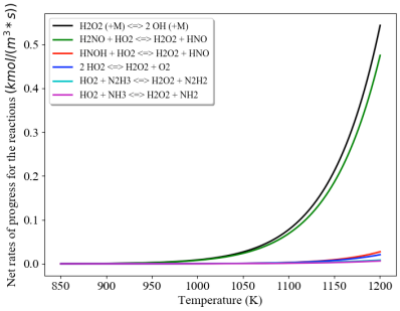

Pure NH_3 T_c = 850 K

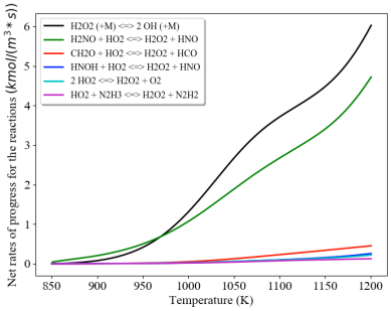

NH_3 with 5%DME T_c = 850 K

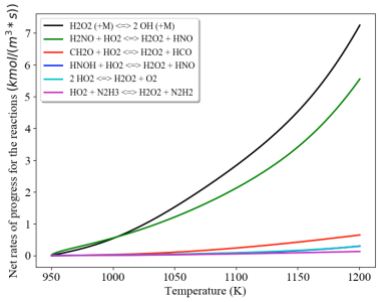

NH_3 with 5%DME T_c = 950 K

ROP of OH

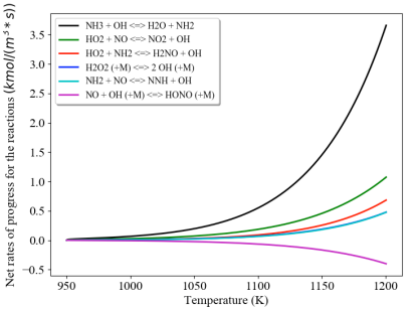

Pure NH_3 T_c = 950 K

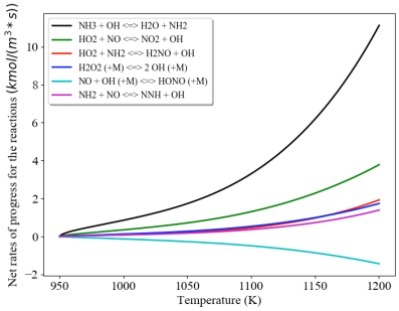

NH_3 with 2%DME T_c = 950 K

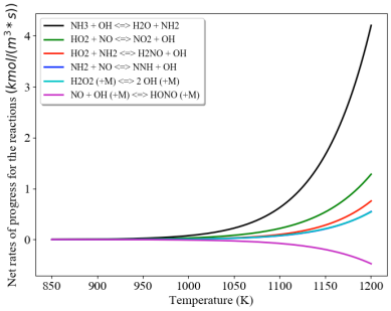

Pure NH_3 T_c = 850 K

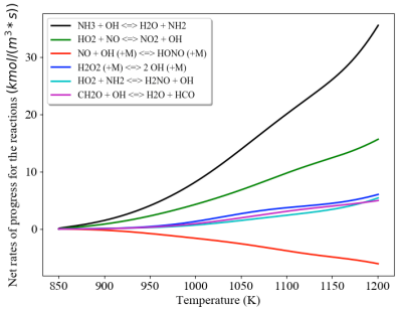

NH_3 with 5%DME T_c = 850 K

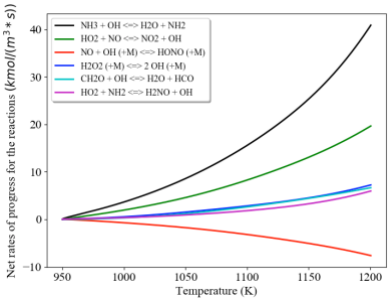

NH_3 with 5%DME T_c = 950 K

φ =1.0

ROP of HO_2

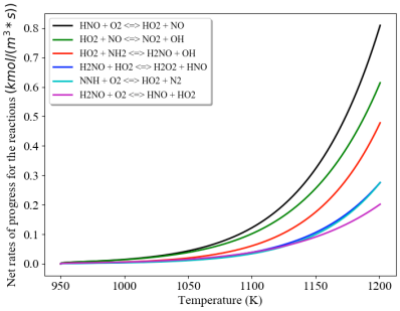

Pure NH_3 T_c = 950 K

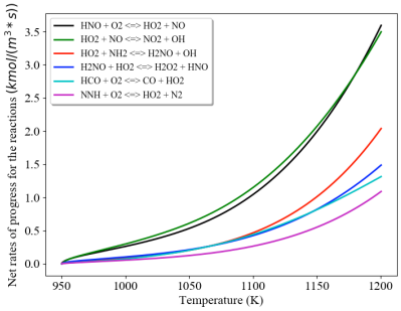

NH_3 with 2%DME T_c = 950 K

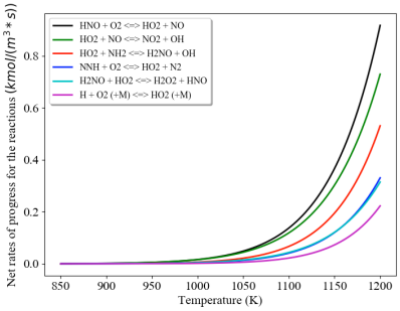

Pure NH_3 T_c = 850 K

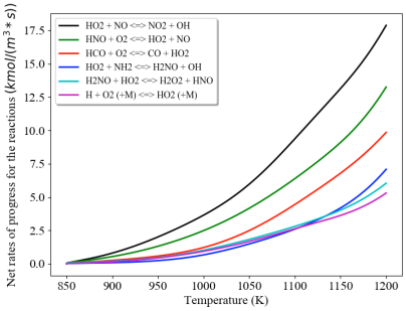

NH_3 with 5% DME T_c = 850 K

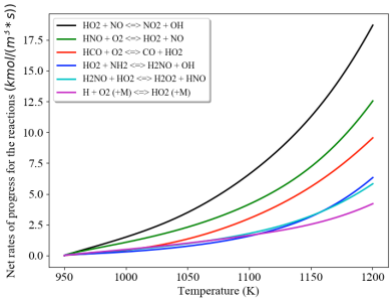

NH_3 with 5%DME T_c = 950 K

ROP of H_2O_2

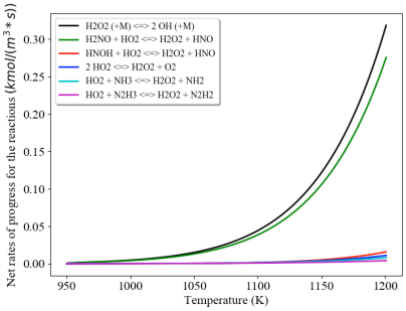

Pure NH_3 T_c = 950 K

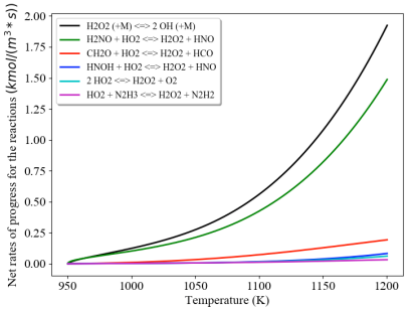

NH_3 with 2%DME T_c = 950 K

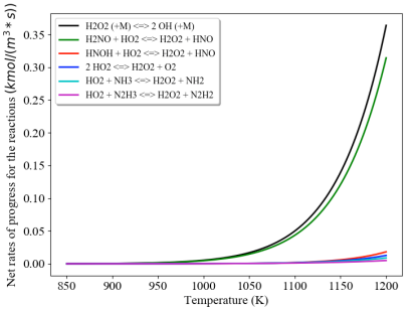

Pure NH_3 T_c = 850 K

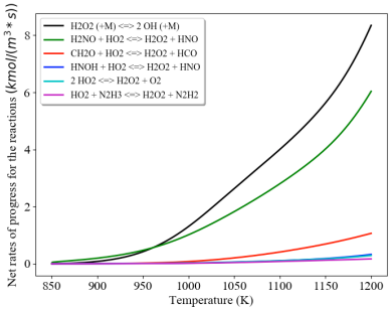

NH_3 with 5%DME T_c = 850 K

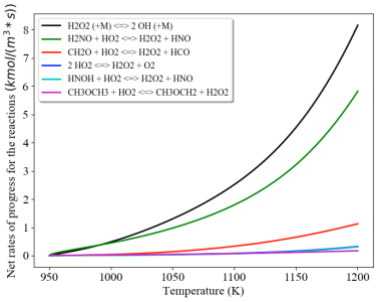

NH_3 with 5%DME T_c = 950 K

ROP of OH

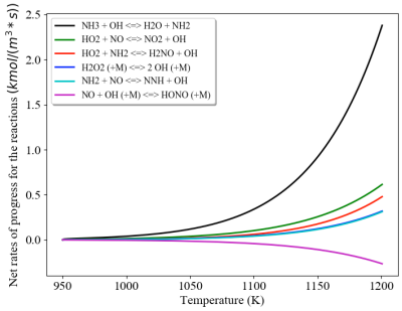

Pure NH_3 T_c = 950 K

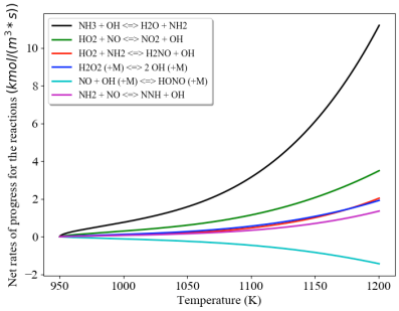

NH_3 with 2%DME T_c = 950 K

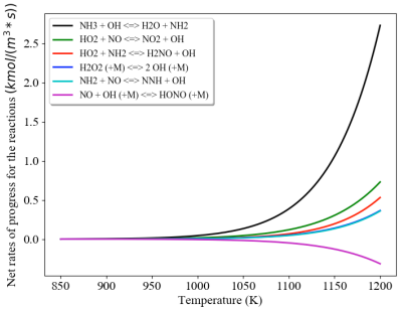

Pure NH_3 T_c = 850 K

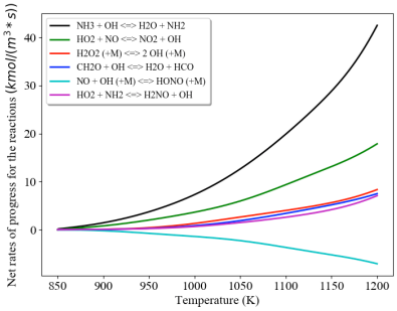

NH_3 with 5%DME T_c = 850 K

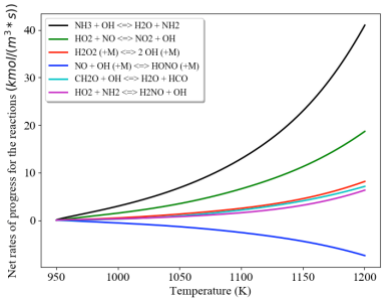

NH_3 with 5%DME T_c = 950 K

Chapter 6: Variation in flame temperature with burner stabilization in 1D premixed dimethyl ether/air flames measured by spontaneous Raman scattering

This chapter is based on the work published in: L. Dai, A. Mokhov, H. Levinsky, Variation in flame temperature with burner stabilization in 1D premixed dimethyl ether/air flames measured by spontaneous Raman scattering, Energy & Fuels. 33 (2019) 11976–11984.

6.1. Experimental conditions and numerical details

This chapter presents the measurements of flame temperatures as a function of exit velocity for DME/air mixtures using spontaneous Raman scattering, which has been discussed in Chapter 2. The variation in temperature vs. exit velocity is then compared with simulations using different chemical mechanisms to assess their predictive power, as indicated in Chapter 1. Dimethyl ether with a purity of 99.8% was used as fuel. The temperature of the fuel/air mixtures was taken as 295 K. Due to the high pressure drop in the burner and low vapor pressure of DME (~ 4.4 bar) at room temperature, the highest exit velocity of unburned DME/air mixture in the present setup is limited to 35 cm/s, which is lower than the free-flame burning velocity at φ = 1.0 (~44 cm/s) reported in other studies [121–123]. As a result, it was impossible to reach adiabatic conditions in DME flames with free burning velocities higher than 35 cm/s. While this limitation has few consequences for the results described below (which rely on the variations in flame temperature with exit velocity), it does limit the assessment of the uncertainty of the Raman measurements at higher temperature. For this purpose, this study uses mixtures of methane (with a purity of 99.995%) and air at room temperature, for which 1-D stabilized and free-burning flames can be obtained with equivalence ratios between 0.7 and 1.3, showing enough variation in absolute temperature for the assessment. Since the reproducibility of the temperature measurements was better than the estimated accuracy ($\pm$ 30 K, see below), the error bars in the temperature plots are $\pm$ 30 K. Additionally to the visual control, the flatness of the flames was verified by measuring the horizontal temperature profiles at all exit velocities. A typical horizontal profile at height of 1 cm for the stoichiometric flame with exit velocity of 30 cm/s is shown in Figure 6.1. As can be seen, the temperature profile is flat with differences not exceeding 30 K at radial distances less than 2 cm from the burner axis. The measured temperature horizontal profiles remain flat up to heights of 2 cm even when exit velocity exceed the free-burning velocity and the ‘hill’ structure is observed visually instead of the flat flame front.

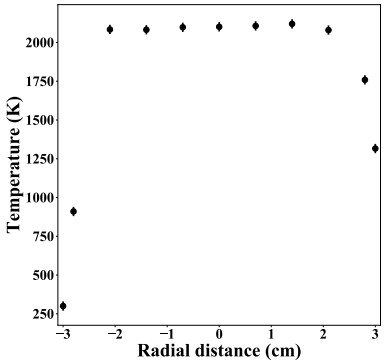

Figure 6.1. Radial temperature profile in methane/air flame at φ = 1.0, v = 30 cm/s, HAB = 1 cm.

The conservation equations for 1-D flames were solved using the Cantera package [47] as discussed in Chapter 1. The 'mixture averaged' model [124] was used for calculation of transport properties. In the calculations, the computation domain was set to 10 cm. The final solution was obtained with a grid of ~140 points. Further increase in the number of grid points resulted in temperature changes less than 10 K. The calculations were performed for both burner-stabilized and free flames. As a rule, the calculations did not converge in the burner stabilized flames with exit velocities in the range higher than 80% of the free burning velocity. For this velocity range, the calculated temperatures shown in the plots below are linearly interpolated. In the Cantera suite, the radiative heat losses are taken into account using the gray-gas approximation in the optically thin limit[125], where CO_2 and H_2O are assumed as the only radiating species. Planck mean coefficients of CO_2 and H_2O are calculated using polynomials from ref. [126,127].

For the assessment of the temperature determination, methane/air flames were simulated using the GRI-Mech 3.0 mechanism, which contains 53 species and 325 elementary chemical reactions [119]. For DME, three widely used chemical mechanisms were evaluated in this Chapter. The 'Zhao Model': the mechanism developed by Zhao et al. [128], based on the studies of the unimolecular decomposition reaction of DME in a flow reactor at a temperature of 980 K and pressure of 10 atm, contains 55 species and 290 reactions. The free-flame burning velocities (S_L) of DME/air flames calculated using this model for equivalence ratios from 0.6 to 2.0 are shown in Figure 6.2. The mechanism proposed by Liu et al. [129] (the 'Liu Model'), obtained by adopting the hydrogen subset from [130] and updating reaction

rate constants of the 'Zhao Model', includes 55 species and 295 reactions. The free-flame burning velocities calculated by Liu Model are also shown in Figure 6.2. As can be seen, the difference between the predictions of these two models are marginal at lean (φ < 1.1) and rich (φ > 1.7) conditions, while the Liu model predicts higher S_L than the Zhao model at 1.1 < φ < 1.7. Lastly, the mechanism developed by Burke et al. [35] ('NUIG Mech_56.54'), based on the studies of the ignition delay time of DME, methane and their mixtures covering a range of conditions relevant to gas turbine environments. This model is more complex than the Zhao and Liu models, and contains 113 species and 710 reactions. Comparing with the Zhao model and the Liu model, the NUIG Mech_56.54 predicts the highest S_L in the range φ from 0.8 to 1.7, while at leaner (φ < 0.8) and richer (φ > 1.7) conditions, the predicted S_L from all three models are indistinguishable as shown in Figure 6.2.

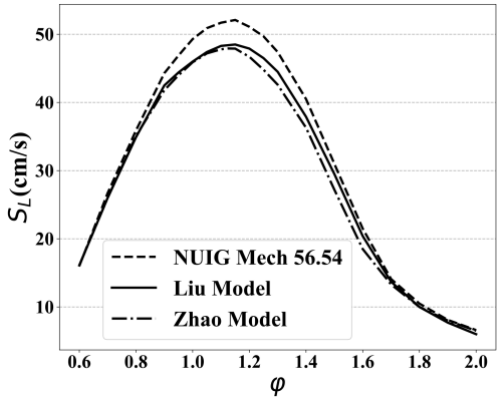

Figure 6.2. Calculated free-flame burning velocities of DME/air flames at temperature 295 K and pressure 1 atm.

6.2. Results and discussion

6.2.1 Temperature measurements in methane/air flames

The accuracy of temperature measurements is assessed here by comparing the measured and calculated temperatures in 'free-burning' flames, i.e. flames without heat transfer to the burner. The temperature of these flames can be calculated using thermodynamics which would obviate uncertainties related to the impact chemical kinetics. To achieve these conditions, the exit velocities of the unburned gas/air mixtures at fixed equivalence ratio are progressively increased to the point at which the flame temperature is

independent of exit velocity. As mentioned above, while the equilibrium temperatures for adiabatic DME/air flames are readily calculated, the free-burning exit velocity could not be reached for these flames under all conditions and methane/air flames were used for this purpose. Figure 6.3 shows temperature profiles measured at φ = 1.0 and v = 10, 20 and 30 cm/s. As expected, the measured flame temperature increases with the exit velocity of the unburned mixture, from ~ 1700 K at v = 10 cm/s up to ~ 2050 K at v = 30 cm/s, indicating decreasing upstream heat losses into the burner surface. At the three exit velocities, the measured temperatures increase to a maximum and then begin to decrease towards the end of the measured domain, the decrease varying with exit velocity. The temperature profiles calculated using GRI-Mech 3.0 without radiative heat loss from the hot gases, as shown Figure 6.3, display the usual increase in temperature from the slow approach to equilibrium caused by radical recombination in the post-flame gases, substantially overpredicting the (measured) temperature. Repeating the calculations while incorporating radiative heat loss improves the agreement with the measured profiles significantly, with a slight overestimate of the heat loss in the measurements for v = 10 cm/s at HAB > 1cm. Very good agreement between the computed profiles with radiative heat losses and the measurements was also observed for other equivalence ratios and exit velocities, implying the necessity of including this heat loss mechanism in the analysis.

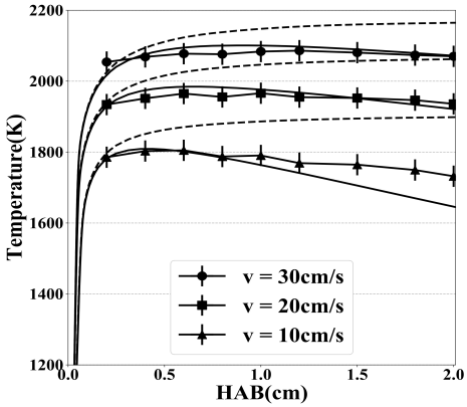

Figure 6.3. Axial temperature profiles in methane/air flames at φ = 1.0. Symbols -measurements in flames at exit velocities 30 cm/s (circles), 20 cm/s (squares), 10 cm/s (triangles). Lines - calculations using GRI-Mech 3.0 with (solid) and without (dashed) radiative heat losses.

The impact of radiative losses on the measured temperature was further analyzed by measuring temperatures at fixed axial distance (HAB = 1cm) in stoichiometric methane/air flames while progressively increasing the exit velocity. The results of these measurements are shown in Figure 6.4. As can be seen, the measured temperature increases with increasing exit velocities up to 38 cm/s. Above this velocity, close to the free burning velocity for stoichiometric methane/air flames [131,132], the measured temperature remains constant, indicating no heat transfer from the flame to the burner. While one would expect the measured flame temperature under these conditions to be the adiabatic stoichiometric value (~2225 K), the maximum measured temperature is ~2150 K. At HAB = 1 cm in a stoichiometric methane/air flame, the observation of a lower temperature can be ascribed to radiative losses and to being upstream of the point at which equilibrium is reached downstream of the burner. The flame temperatures were calculated with and without radiative heat losses as shown in Figure 6.4. The calculations without radiative heat losses overpredict the flame temperature ~ 60 K at v < 38 cm/s, while the calculations with radiative heat losses predict the flame temperature very well up to v = 38 cm/s. This agreement is further examined by varying the equivalence ratio and comparing the measurements for the free-flame temperatures with the computations with and without radiation.

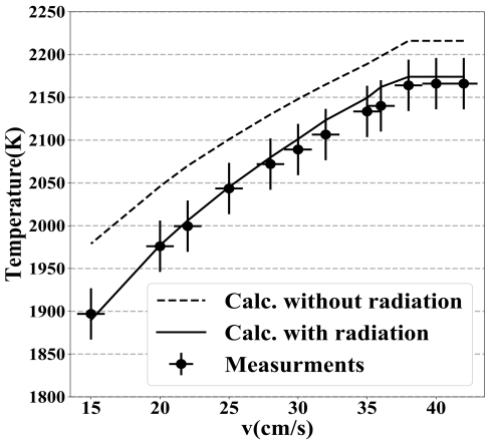

Figure 6.4. Measured (circles) and calculated temperatures with (solid line) and without (dashed line) radiative heat losses at HAB = 1cm as a function of exit velocity in stoichiometric methane/air flames.

Similar measurements were performed at different equivalence ratios. The results of these measurements are presented in Figure 6.5, where the temperatures of free flames at HAB = 1 cm are shown. As can be seen, at all equivalence ratios the measured flame temperatures are lower than adiabatic ones. In rich flames the difference is ~ 40 K, at stoichiometric flame it is ~ 60 K and decreases to ~ 30 K in lean flames. That the flame temperature measured by spontaneous Raman scattering is systematically lower than adiabatic was also observed previously [85]. As discussed above, this discrepancy is attributed to radiative heat losses, which can be substantial in high temperature flames [133–135]. To test this assumption, calculations of 1-D flames taking radiative heat losses into consideration were performed. As can be seen in Figure 6.5, the calculations and measurements agree very well if the radiative heat losses are accounted for.

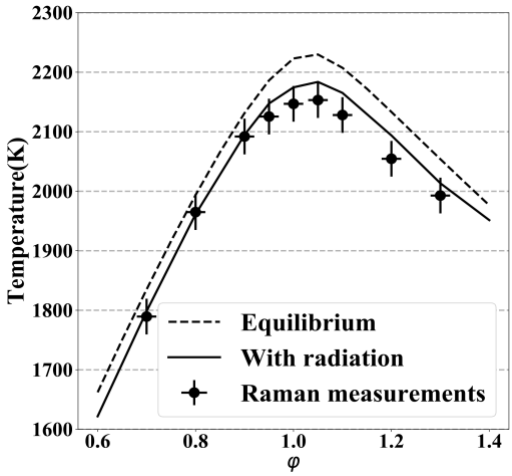

Figure 6.5. The methane/air flame temperature as a function of equivalence ratio at HAB = 1 cm. Measurements (circles) and calculations with (solid line) and without (dashed line) radiative heat losses.

Comparing the measured and calculated temperatures in free-burning flames, the accuracy of the Raman temperature measurements is estimated to be 30 K. Therefore, in the analysis of the performance of the mechanisms below, the disagreement between the measurements and calculations will only be considered as significant if it exceeds 30 K. As mentioned above, this uncertainty is used in the figures showing temperature measurements.

6.2.2 Temperature measurements in DME/air flames

A typical vertical temperature profile in DME /air flame at φ = 1.0, v = 25 cm/s is shown in Figure 6.6, as well as the temperatures calculated using the Liu Model with and without radiative heat losses. Calculations with other mechanisms yielded similar results and are not shown in Figure 6.6 to avoid clutter. As seen for the methane/air results presented above, the calculations without radiation overpredict the measured temperatures, while the inclusion of radiation brings the computed and measured temperature profiles into agreement within the measurement uncertainty. Hence, only the calculations with radiative heat loss will be used for comparison with the measured temperatures in the discussion below.

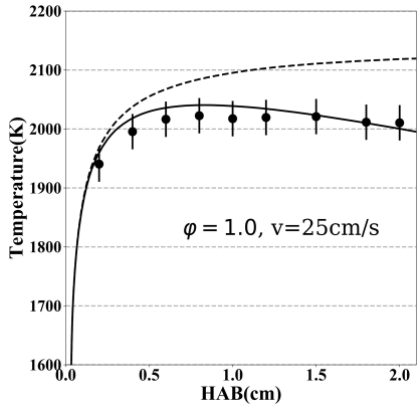

Figure 6.6. Axial temperature profiles in DME/air flames at φ = 1.0, v = 25 cm/s. Circles - measurements in flames, lines - calculations using the Liu Model with (solid) and without (dashed) radiation.

The measured and calculated DME flame temperatures as a function of exit velocities at fixed HAB = 1 cm are shown in Figure 6.7, for equivalence ratios φ = 0.6, 0.8, 1.0, 1.4, 1.7 and 2.0. To view the full range of temperature variation and still amplify the differences observed, the axes for the different equivalence ratios are plotted on different scales; but for all data, the error bars of measured flame temperature and exit velocity were set at 30 K and 1 cm/s, respectively, in all graphs in Figure 6.7. The highest computed exit velocities shown in the figures are those calculated free-flame burning velocities at the specified equivalence ratio shown in Figure 6.2. Experimentally, the free-flame burning velocity is taken either as the exit velocity above which the measured flame temperature remains constant, as in

Figure 6.6, or the exit velocity at which the measured flame temperature reaches the calculated free-flame temperature.

At the lowest equivalence ratio φ = 0.6 (Figure 6.7a), stable flames could be obtained only in the range of exit velocities from 10 to 14 cm/s and the variations in flame temperature are only ~80 K in this range. While all three mechanisms predict temperatures within 20 K of each other, they underpredict the measurements by 30 K or more, i.e., larger than estimated accuracy of the temperature measurements as discussed above. Provided that the sensitivity of temperature to the rate of individual reactions does not change sign with varying the exit velocity, for burner-stabilized flames, recall that if the free-flame burning velocity is too high, then, at a given exit velocity ($v < S_L$) more heat must be transferred to the burner to reduce the actual burning velocity to the exit velocity. Accordingly, the observation that the computations consistently underpredict the flame temperature suggests a free-flame burning velocity that is too high. It is noted here that a stable flat flame could not be made at an exit velocity of ~16 cm/s, which is the predicted free burning velocity for all three mechanisms, but it is observed that at the highest exit velocity attainable (~14 cm/s) the measured temperature has already reached that predicted for the free flame (~ 1700 K) at φ = 0.6. Thus, our measurements indicate that the free burning velocity of DME/air flames at φ = 0.6 is roughly 14 cm/s. Most free-flame burning velocity measurements for DME/air flames were usually obtained in the range φ = 0.7-1.9 [43,136–138]. However, to our knowledge, the only measurement of the free burning velocity at φ = 0.6 was performed by Wang et al. [8] and reported to be slightly less than reported here, ~12 cm/s. The results shown in Figure 6.7(a) show a temperature at 12 cm/s that is significantly lower than that at 14 cm/s, indicating that the value reported by Wang et al.[8] is too low. Being able to indicate whether a predicted (or measured) value is too high or too low is a substantial advantage of examining the behavior of burner stabilized flames.

The differences among the calculated temperatures from all three mechanisms are even less at φ = 0.8 (Figure 6.7b). At this equivalence ratio, all three mechanisms slightly underestimate the measured flame temperatures ($\geq$ 30 K) in the range of v = 10 - 20 cm/s, which is consistent with the underestimation of flame temperature observed at φ = 0.6; the agreement between measurements and calculations is significantly improved at exit velocities above 20 cm/s (temperature above 1900 K).

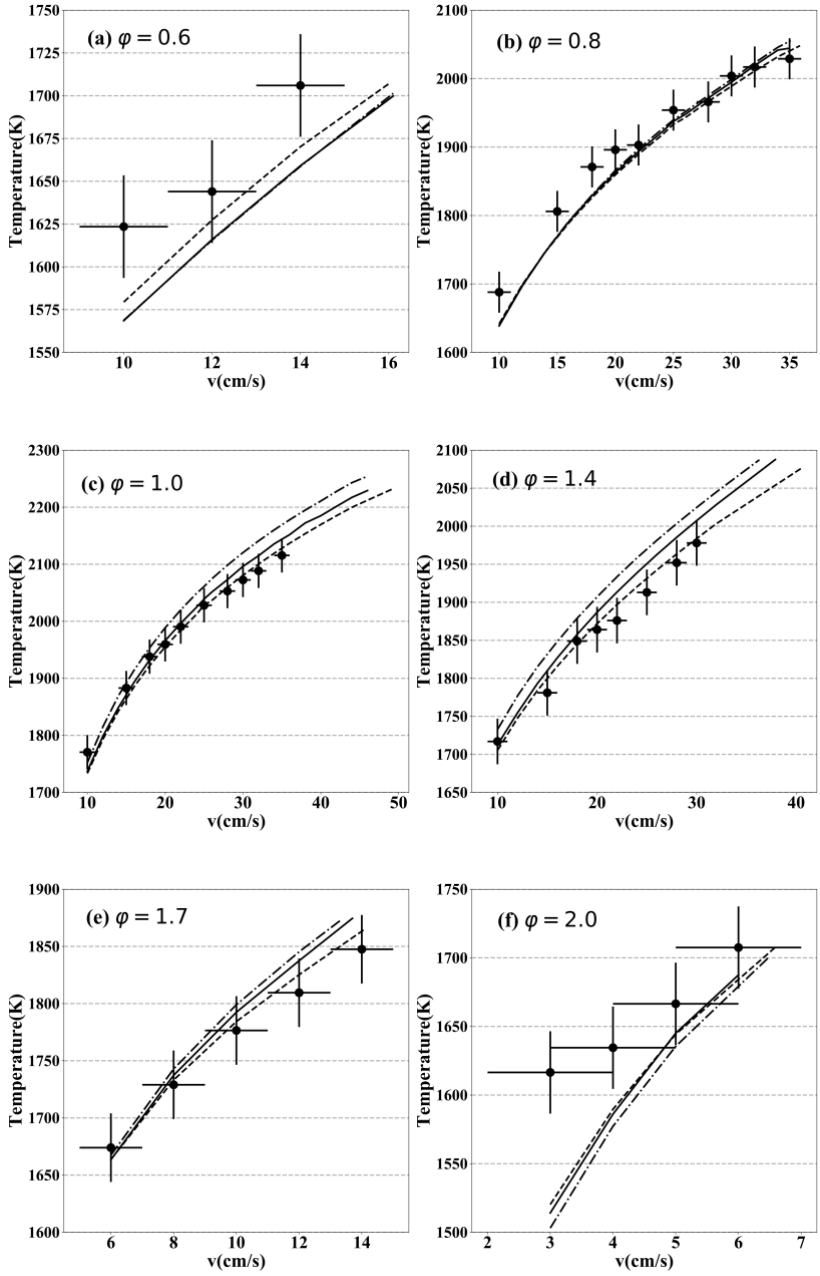

Figure 6.7. Measured (circles) and calculated (solid line - 'Liu Model', dashed line - 'NUIG Mech 56.54', dashed dot line - 'Zhao Model') temperatures in DME/air flames at φ = 0.6 (a), φ = 0.8 (b), φ = 1.0 (c), φ = 1.4 (d), φ = 1.7 (e), φ = 2.0 (f) as a function of exit velocity at HAB = 1 cm.

In stoichiometric (Figure 6.7c) and rich (φ = 1.4, Figure 6.7d) flames, the differences among the temperatures predicted by the three mechanisms become more noticeable. The Zhao Model always predicts the highest temperatures, while NUIG Mech_56.54 predicts the lowest temperature, ~50 K lower than the Zhao Model. The predictions of the Liu Model lie between the other two mechanisms. This observation is consistent with the differences in the free-flame burning velocities shown in Figure 6.2: at φ = 1.0, 46, 45.9 and 49.3 cm/s are predicted by the models Zhao, Liu and NUIG Mech_56.54, respectively, and 36.3, 37.9 and 40.5 cm/s at φ = 1.4. At φ = 1.0, all three models represent the experimental results well at v < 20 cm/s, but diverge at higher exit velocity; at v > 20 cm/s, the Liu Model is still within the experimental uncertainty of the temperature measurements, while NUIG Mech 56.54 is in very good agreement with the experiments and the predictions of the Zhao Model are outside the measurement uncertainty, by nearly 50 K. Similar trends are observed at φ = 1.4 over the entire range of exit velocity studied. These results suggest that the free-flame burning velocities are closer to 49 cm/s and 40 cm/s for φ = 1.0 and 1.4, respectively.

For φ = 1.7 in Figure 6.7(e), the DME flame can only be stabilized in the range of exit velocities 6 – 14 cm/s. All three mechanisms predict the measured temperatures within 30 K; the three mechanisms predict free-flame burning velocities within 13.5±0.5 cm/s.

In the richest flame, φ = 2.0 in Figure 6.7(f), the exit velocities were limited in the range 3 – 6 cm/s. Allowing for the difficulty in stabilizing a fuel-rich flame at exit velocities below 5 cm/s, which is ascribed to buoyancy effects, the three mechanisms tend to underestimate the flame temperature. To our knowledge, the free burning velocity of DME/air flame at φ = 2.0 has not been measured previously, but, based on the measured temperature, the results indicate a free burning velocity ~ 6 cm/s. Considering the ±1 cm/s uncertainty of the measurements, the computed free-flame burning velocities in the range 6 - 6.6 cm/s is considered to be in good agreement with the measurements shown.

Summarizing, the overall performance of the chemical mechanisms in the prediction of flame temperatures as a function of equivalence ratio is good in the region φ = 0.8-1.7, with more deviation at 0.6 and 2.0. Below the possibility of using the method to improve the model predictions is explored.

6.2.3 The sensitivity analysis of flame temperature to variation of rates of chemical reactions

A sensitivity analysis is performed to clarify the performance of the chemical mechanisms in prediction of the measured flame temperatures. The calculations were performed using 'Liu Model'; its performance is similar to 'NUIG Mech_56.54', but its smaller size facilitates the analysis. For this purpose, the pre-exponential factor of Arrhenius equation for the *i*th reaction A_i is increased by 50% and the sensitivity coefficients are calculated by:

$$S_i = 2 * \big(T(x, 1.5A_i) - T(x, A_i)\big), \tag{6.1}$$

where $T(x, 1.5A_i)$ and $T(x, A_i)$ are temperatures calculated at distance x with $1.5A_i$ andA_i, respectively. In this formulation, the sensitivity coefficient is temperature change when increasing A_i by 50%, assuming a linear dependence of temperature upon the rates of chemical reactions.

The sensitivity analysis was performed for flames at equivalence ratios φ = 0.6, 1.0, 1.7 and 2.0, for the exit velocities used in the experiments. The results of the sensitivity analysis at HAB = 1.0 cm are presented in Figure 6.8, only the five most important reactions are shown in the plot for each equivalence ratio. It is first observed that, in contrast to the results for hydrogen/air flames [44], the impact of most sensitive reactions is slightly dependent of exit velocity (differences less than 10 K). Consequently, variation of the rates of these reactions will do little to affect the curvature of the plots of flame temperature vs. exit velocity. For the stoichiometric DME/air flame (Figure 6.8b), the chain branching reaction

$$H + O_2 = O + OH \tag{$R6.1$}$$

has the highest sensitivity $S_{R1} \approx$- 90 K, while the reaction of CO oxidation

$$CO + OH = H + CO_2 \qquad (R6.2)$$

takes the second place with S_{R2} ≈ - 30 K.

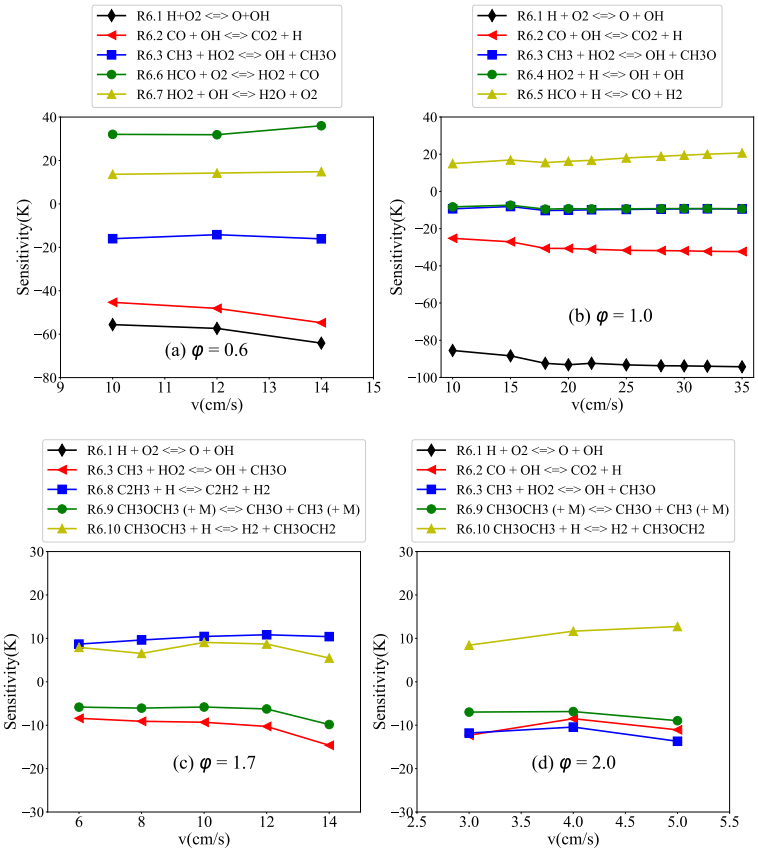

Figure 6.8. Sensitivity coefficient for temperatures at HAB = 1 cm as a function of exit velocity in DME flame,φ = 0.6 (a), φ = 1.0 (b), φ = 1.7 (c), φ = 2.0 (d).

Reactions

$$CH_3 + HO_2 = OH + CH_3O \qquad (R6.3)$$

and

$$HO_2 + H = OH + OH \qquad (R6.4)$$

have close negative sensitivity coefficients (roughly - 20 K), while only reaction

$$HCO + H = CO + H_2 \qquad (R6.5)$$

shows positive influence ~20 K on the flame temperature. Recalling the discussion above, reactions that increase the free-flame burning velocity will reduce the temperature of the burner-stabilized flame. Of course, these five reactions are also the most sensitive reactions for the free burning velocity in stoichiometric methane/air flame[45,137,139,140].

At φ = 0.6, reactions R6.1, R6.2 and R6.3 remain most important reactions, with sensitivity coefficients $S_{R6.1} \approx$ - 60 K, $S_{R6.2} \approx$ - 40 K and $S_{R6.3} \approx$ - 20 K, respectively, while reactions R6.4 and R6.5 are replaced by

$$HCO + O_2 = HO_2 + CO \qquad (R6.6)$$

with the sensitivity coefficient $S_{R6} \approx$ 30 K and

$$HO_2 + OH = H_2O + O_2 \qquad (R6.7)$$

with the sensitivity coefficient $S_{R6.7} \approx$ 15 K. The most sensitive reactions (Figure 6.8a) for DME flame at φ = 0.6 are also important for methane/air flames[141]. To improve the agreement between the measured and computed temperatures, the latter must be increased.

That is, the free-flame burning velocity must be reduced. This implies decreasing the rate of R6.1-R6.3 or increasing the rates of R6.6/R6.7. However, given the importance of these reactions in the burning velocity of methane, the impact of any changes in these rates on the predictions for methane would have to be assessed simultaneously. As such, this study refrains from doing so here.

At φ = 1.7, reaction R6.1 (not shown in Figure 6.8c) and R6.3 still show the highest sensitivity, with coefficients $S_{R6.1} \approx$ - 100 K and $S_{R6.3} \approx$ - 10 K, respectively. Moreover, three new reactions appear in the list of most sensitive reactions: the reaction between vinyl radical and hydrogen

$$C_2H_3 + H = C_2H_2 + H_2, \qquad (R6.8)$$

the decomposition reaction of DME

$$CH_3OCH_3(+M) = CH_3O + CH_3(+M) \qquad (R6.9)$$

and H atom abstraction from DME

$$CH_3OCH_3 + H = H_2 + CH_3OCH_2. \qquad (R6.10)$$

At the richest condition, φ = 2.0, reaction R6.1 still has the largest negative sensitivity ($S_{R6.1} \approx$ - 90 K, not shown in Figure 6.8d) and reaction R6.10 shows the largest positive sensitivity $S_{R6.10} \approx 10$ K. Three other reactions R6.2, R6.3 and R6.9 have S_i of roughly -10 K. At φ = 2.0, considering only the two highest points, as mentioned above, the calculated temperatures are within the vertical and horizontal error bars. Although the predictions for φ = 1.7 are also reasonbly close to the measurements, this equivalence ratio is chosen to examine the potential improved agreement by varying two of the rate constants. Since both R6.9 and R6.10 are sensitive

reactions at this equivalence ratio, and only consider DME, these reactions are chosen as an example. Since the predicted temperatures must decrease to improve the agreement of this mechanism with the experimental temperatures, the rate of R6.9 should be increased and/or R6.10 should be decreased. Figure 6.9 shows the results of increasing R6.9 by a factor of 10 and by reducing R6.10 by the same factor. This is outside the range of uncertainty of these reactions[142,143]. Both of these changes bring the predictions of the Liu Model at higher exit velocity closer to the experiments, while maintaining the agreement at lower velocities. It is noted that the change in R6.9 increases the free-flame burning velocity to 15.2 cm/s, while the decrease in the rate of R6.10 increases the burning velocity to 15.7 cm/s.

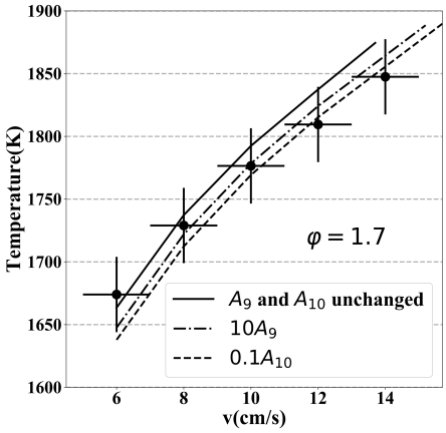

Figure 6.9. Measured (circles) and calculated temperatures as a function of exit velocity at HAB = 1 cm, φ = 1.7. Solid line - with reaction rates unchanged, dashed dot line - the rate of reaction R6.9 increased by a factor 10, dashed line - the rate of reaction R6.10 decreased by a factor 10.

6.3. Summary and Conclusions

In this chapter, the flame temperatures in flat, laminar premixed dimethyl ether (DME)/air flames with varying degrees of burner stabilization were measured by spontaneous Raman scattering in a range of equivalence ratio (φ) from 0.6 to 2.0. Three commonly used mechanisms to describe DME oxidation were evaluated by comparing the calculated variation of flame temperature derived from 1-D flame calculations as a function of DME/air exit velocity with those obtained from the measurements. The results showed

the necessity of incorporating radiative heat losses in the flame calculations. The three mechanisms yield similar results at φ = 0.6 and 2.0, underpredicting the temperatures more than 30 K. Differences between measured and predicted temperatures for burner-stabilized flames are seen to indicate whether a free-flame burning velocity (S_L) is too high or too low. The results suggest a free-flame burning velocity of ~14 cm/s at φ = 0.6, 2 cm/s lower than the mechanisms predict, and burning velocities closer to 49 cm/s and 40 cm/s for φ = 1.0 and 1.4, respectively. Sensitivity analysis of the DME/air flame temperature as a function of exit velocity shows that the DME decomposition reaction and H abstraction from DME become important in the rich flames at φ = 1.7 and 2.0.

Summary and Perspectives

The incentive to limit global temperature rising and reduce man-made greenhouse emissions is driving the development and introduction of alternative fuels in current combustion engines. Ammonia and DME both are considered as promising alternative fuels owing to their physical and chemical properties. Fundamental combustion properties, e.g. ignition delay time and burning velocity of ammonia, DME and their selected blends are essential to design fuel compositions and tailor the engine modifications to fuel properties. Moreover, such measurements are crucial for evaluation of chemical mechanisms describing fuel oxidation, which play an important role in combustion simulations used to analyze the behavior of combustion equipment and fuels. This thesis focused on measuring the ignition delay times of ammonia/additive mixtures and the flame temperatures of DME/air mixtures and testing ability of chemical mechanisms describing the oxidation of these fuels. The experimental setups used in this study, including a rapid compression machine (RCM) and a spontaneous Raman scattering setup were discussed in Chapter 2.

The ignition delay times of NH_3/H_2, NH_3/CH_4 and NH_3/DME mixtures were studied in Chapter 3, 4 and 5, respectively. All these additives show strong ignition-enhancing effect on NH_3, while the effect of additives is non-linear, i.e. that the ignition enhancing effect of additives decreases with higher additive fraction in the fuel. With an eye towards practical use of ammonia/additives, DME is a promising ignition enhancer for ammonia fueled compression ignition engines since the autoignition temperature of ammonia can be reduced by more than 250 K with modest (5%) DME addition. When aiming to increase the burning velocity of ammonia in spark ignition engines, the analysis of ignition delay time and burning velocity should be combined for NH_3/H_2 and NH_3/CH_4 mixtures in the future studies, to evaluate the tradeoff between increasing burning velocity and maintaining high knock resistance. An unanswered question regards the anomalous pre-ignition pressure rise that was observed in measurements at φ = 0.5, NH_3 containing 50% CH_4 and 2 and 5% DME with high reproducibility. Given the possibility that undesired combustion behavior (misfire for CI engines and knocking for SI engines) could occur in practical engines, the origins of this phenomenon are worthy of further investigation. Laser diagnostics could be

employed to detect the key intermediates and measure temperature in the period leading up to ignition.

During the course of this study a new NH_3/DME mechanism that includes interactions between ammonia and DME species was developed and tested. This mechanism predicts the ignition delay times of NH_3/H_2 and NH_3/CH_4 mixtures very well at the conditions studied. For NH_3/DME mixtures, this mechanism predicts the overall ignition delay times well, including the pre-ignition pressure rise, but cannot capture the two-stage ignition phenomenon. Kinetic analysis based on present mechanism indicates that the ignition enhancing effect of H_2 and CH_4 on NH_3 is closely related to the formation and decomposition of H_2O_2, while for NH_3/DME, the enhancing effect is seen to arise from the 'early' oxidation of DME, i.e., the substantial oxidation of DME prior to significant ammonia consumption. The analysis shows oxidation of DME in the early stages via the so-called low-temperature route, which generates heat and reactive species that accelerate the decomposition reactions of ammonia at much lower temperature than for neat ammonia, and thus leads to a reduction in the ignition delay time. The data in this thesis will be used to improve the mechanism further, to capture and analyze the unusual ignition behavior reported here, including the two-stage ignition phenomenon observed under conditions where neither pure fuel shows two-stage ignition.

In Chapter 6, the flame temperatures of burner-stabilized, flat laminar premixed DME/air mixtures were measured using spontaneous Raman scattering. The experimental temperatures were compared to predictions from one-dimensional flame calculations to assess the accuracy of different chemical mechanisms for DME oxidation. In some cases, the results permitted improved recommendations for the burning velocity of these mixtures. As stated above, since the burning velocity is just as important as ignition delay time for considering a fuel for spark-ignited engines, measurement of ammonia/additive mixtures using the same method are recommended to gain more insight in the oxidation process at flame temperatures and to test the NH_3/DME mechanism over a wider range of experimental conditions.

Having investigated the combustion properties of ammonia and ammonia blends with selected additives in this study, a few additional recommendations for future investigation are given below:

1) Which future transportation fuels will be used in different applications is uncertain at present. More kinds of additives can be produced from

renewable energies, for instance, alcohols, biodiesel and other ethers; these should be evaluated to determine their advantages and limitations as combustion promoter for ammonia.

2, The autoignition study of ammonia/additives should be expanded to shock tubes; this allows investigation of the behavior of these mixtures over a wider range of experimental conditions and, together with RCM measurements, serve as benchmarks for mechanism development.

3, As discovered in this study, the low DME fraction combined with ammonia appears to access a region of chemical behavior not well-represented in the mechanism. Thus, more work is needed to improve the mechanism in predicting both the ignition delay times and unusual ignition behaviors. Measurement of ignition and species profiles in high-pressure flow reactors could help accomplish this goal.

4, It is noted that the pre-ignition heat release in some cases might lead to ambiguity of the RCM simulations using inert experiments, more work should be done to precisely determine the specific volume for pre-ignition or two-stage ignition measurements.

Samenvatting

De wens om de mondiale stijging van de atmosferische temperatuur te beperken en de uitstoot van broeikasgassen door menselijke handelen te verlagen drijft de ontwikkeling en implementatie van alternatieve brandstoffen in de huidige verbrandingsmotoren. Vanwege hun fysische en chemische eigenschappen, ammoniak (NH_3) en dimethyl ether (DME) worden beschouwd als veelbelovende alternatieve brandstoffen. Bij het willen toepassen van deze brandstoffen of hun mengsels in bestaande motoren is het beoordelen van hun verbrandingseigenschappen, zoals ontstekingsvertragingstijd en verbrandingssnelheid essentieel, zowel bij het formuleren van de samenstelling van de brandstof als bij het ontwikkelen/aanpassen van het motorontwerp. Bovendien zijn dergelijke metingen onmisbaar bij het beoordelen van chemische mechanismen die de oxidatie van de brandstof beschrijven, die toegepast worden bij de simulatie van verbrandingsprocessen om het gedrag van verbrandingsapparatuur en brandstoffen te analyseren. In dit proefschrift ligt de nadruk op het meten van de ontstekingsvertragingstijd van mengsels van ammoniak met verschillende toevoegingen ("additieven") en van de vlamtemperaturen van DME/luchtmengsels, waarbij het voorspellende vermogen wordt getoetst van mechanismen die de oxidatie van deze brandstoffen beschrijven.

De experimentele opstellingen die in het onderzoek worden toegepast, zoals de Rapid Compression Machine en de opstelling voor Ramanverstrooiing voor het meten van vlamtemperatuur zijn in Hoofdstuk 2 beschreven.

De ontstekingsvertragingstijden van NH_3/H_2-, NH_3/CH_4- en NH_3/DME-mengsels zijn onderzocht in respectievelijk Hoofstukken 3, 4 en 5. Alle drie additieven bevorderen de ontsteking van NH_3 sterk, maar hun ontstekingsbevorderende effect wordt minder met toenemende fractie van additieven in de brandstof. Mengsels van ammoniak met lage fracties DME (2%/5% in de brandstof) laten complex gedrag zien. Bij mengsels met luchtovermaat wordt een langzame drukverhoging in de periode voor ontsteking waargenomen, terwijl stoichiometrische en brandstofrijke mengsels tonen tweetraps-ontsteking. Beide verschijnselen worden niet waargenomen in de pure brandstoffen. Met het oog op praktisch gebruik van ammoniak/additieven-mengsels is DME veelbelovend als toevoeging aan

ammoniak voor motoren die gebaseerd zijn op compressie-ontsteking: bij een bescheiden fractie DME in de brandstof (5%) kan de zelfontbrandingstemperatuur van ammoniak met meer dan 250 K verlaagd worden verlaagd. Bij het verhogen van de verbrandingssnelheid van ammoniak voor gebruik in motoren met vonkontsteking, dienen de verbrandingssnelheid en de ontstekingsvertragingstijden van NH_3/H_2- en NH_3/CH_4-mengsels geanalyseerd te worden om de afweging te kunnen maken tussen verhoogde verbrandingssnelheid en de noodzaak om een hoge klopvastheid te waarborgen.

Tijdens dit onderzoek zijn een aangepaste mechanisme voor NH_3-oxidatie, en een nieuwe NH_3/DME-oxidatiemechanisme, ontwikkeld en getest, waarbij dit laatste mechanisme ook reacties tussen componenten afgeleid van NH_3 en DME bevat. De mechanismen voorspellen de ontstekingsvertragingstijden van NH_3/H_2- en NH_3/CH_4-mengsels goed onder de condities van de experimenten. Voor NH_3/DME-mengsels, voorspelt het mechanisme de overall ontstekingsvertragingstijd goed, inclusief de experimenteel waargenomen geleidelijke drukverhoging, maar voorspelt de tweetraps-ontsteking van de mengsels niet. De mechanistische analyse op basis van de huidige mechanismen associeert het ontstekingsbevorderende effect van H_2 en CH_4 op NH_3 met de vorming en decompositie van H_2O_2. Het effect van DME wordt toegeschreven aan de ‘vroege’ oxidatie van DME, d.w.z. de substantiële oxidatie van DME voordat significante hoeveelheden NH_3 reageren. De analyse laat ook zien dat net na compressie de oxidatie van DME begint door een reeks chemische reacties die kenmerkend is voor de ontsteking van pure DME bij lage temperatuur. De ‘vroege’ oxidatie van DME gaat gepaard met de ontwikkeling van warmte en reactieve componenten die vervolgens de decompositie van NH_3 bespoedigen bij een veel lagere temperatuur dan bij puur NH_3. Dit proces leidt tot een sterke verlaging van de ontstekingsvertragingstijd.

Hoofdstuk 6 beschrijft metingen van vlamtemperatuur bij vlakke, brandergestabiliseerde DME/luchtmengsels, waarbij de vlamtemperatuur door middel van spontane Ramanverstrooiing gemeten is. De variatie in gemeten vlamtemperatuur bij variërende stabilisatie is vergeleken met de resultaten van 1-D vlamberekeningen om de nauwkeurigheid van verschillende chemische mechanismen voor DME-oxidatie te toetsen. Terwijl de drie geteste mechanismen de resultaten redelijk voorspellen, zijn bij enkele

condities aanbevelingen voor verbeterde verbrandingssnelheden gedaan op basis van de metingen.

Hoofdstuk 7 vat de resultaten van het proefschrift samen en geeft aanbevelingen voor toekomstig onderzoek.

References

[1] DNG VL, Energy Transtion Outlook, 2019.

[2] S. Verhelst, T. Wallner, Hydrogen-fueled internal combustion engines, Prog. Energy Combust. Sci. 35 (2009) 490–527.

[3] M. Hattori, S. Iijima, T. Nakao, H. Hosono, M. Hara, Solid solution for catalytic ammonia synthesis from nitrogen and hydrogen gases at 50 °C, Nat. Commun. 11 (2020) 1–8.

[4] Z. Azizi, M. Rezaeimanesh, T. Tohidian, M.R. Rahimpour, Dimethyl ether: A review of technologies and production challenges, Chem. Eng. Process. Process Intensif. 82 (2014) 150–172.

[5] G. Thomas, G. Parks, Potential roles of ammonia in a hydrogen economy: a study of issues related to the use ammonia for on-board vehicular hydrogen storage, US Dep. Energy. (2006) 23.

[6] N.J. Duijm, F. Markert, J.L. Paulsen, Safety assessment of ammonia as a transport fuel, 2005.

[7] G. Thomas, B. Feng, A. Veeraragavan, M.J. Cleary, N. Drinnan, Emissions from DME combustion in diesel engines and their implications on meeting future emission norms: A review, Fuel Process. Technol. 119 (2014) 286–304.

[8] Y.L. Wang, A.T. Holley, C. Ji, F.N. Egolfopoulos, T.T. Tsotsis, H.J. Curran, Propagation and extinction of premixed dimethyl-ether/air flames, Proc. Combust. Inst. 32 I (2009) 1035–1042.

[9] M.Y. Kim, S.H. Yoon, B.W. Ryu, C.S. Lee, Combustion and emission characteristics of DME as an alternative fuel for compression ignition engines with a high pressure injection system, Fuel. 87 (2008) 2779–2786.

[10] S.H. Park, C.S. Lee, Applicability of dimethyl ether (DME) in a compression ignition engine as an alternative fuel, Energy Convers. Manag. 86 (2014) 848–863.

[11] Y. Zhao, Y. Wang, D. Li, X. Lei, S. Liu, Combustion and emission characteristics of a DME (dimethyl ether)-diesel dual fuel premixed charge compression ignition engine with EGR (exhaust gas recirculation), Energy. 72 (2014) 608–617.

[12] Q. Liu, X. Chen, J. Huang, Y. Shen, Y. Zhang, Z. Liu, The characteristics of flame propagation in ammonia/oxygen mixtures, J. Hazard. Mater. 363 (2019) 187–196.

[13] M. Pochet, V. Dias, B. Moreau, F. Foucher, H. Jeanmart, F. Contino, Experimental and numerical study, under LTC conditions, of ammonia ignition delay with and without hydrogen addition, Proc. Combust. Inst. 37 (2018) 621–629.

[14] S. Frigo, R. Gentili, Analysis of the behaviour of a 4-stroke Si engine fuelled with ammonia and hydrogen, Int. J. Hydrogen Energy. 38 (2013) 1607–1615.

[15] J. Li, H. Huang, N. Kobayashi, Z. He, and Y. Nagai, Study on using hydrogen and ammonia as fuels: Combustion characteristics and NOx formation, Int. J. Energy Res. 38 (2014) 1214–1223.

[16] O. Kurata, N. Iki, T. Matsunuma, T. Inoue, T. Tsujimura, H. Furutani, H. Kobayashi, A. Hayakawa, Performances and emission characteristics of NH_3–air and NH_3-CH_4–air combustion gas-turbine power generations, Proc. Combust. Inst. 36 (2017) 3351–3359.

[17] A. Valera-Medina, R. Marsh, J. Runyon, D. Pugh, P. Beasley, T. Hughes, P. Bowen, Ammonia–methane combustion in tangential swirl burners for gas turbine power generation, Appl. Energy. 185 (2017) 1362–1371.

[18] C.W. Gross, S.C. Kong, Performance characteristics of a compression-ignition engine using direct-injection ammonia-DME mixtures, Fuel. 103 (2013) 1069–1079.

[19] K. Ryu, G.E. Zacharakis-Jutz, S.C. Kong, Performance characteristics of compression-ignition engine using high concentration of ammonia mixed with dimethyl ether, Appl. Energy. 113 (2014) 488–499.

[20] A.J. Reiter, S.C. Kong, Combustion and emissions characteristics of compression-ignition engine using dual ammonia-diesel fuel, Fuel. 90 (2011) 87–97.

[21] A.J. Reiter, S.C. Kong, Demonstration of compression-ignition engine combustion using

ammonia in reducing greenhouse gas emissions, Energy and Fuels. 22 (2008) 2963–2971.
[22] O. Mathieu, E.L. Petersen, Experimental and modeling study on the high-temperature oxidation of Ammonia and related NO_x chemistry, Combust. Flame. 162 (2015) 554–570.
[23] B. Shu, S.K. Vallabhuni, X. He, G. Issayev, K. Moshammer, A. Farooq, R.X. Fernandes, A shock tube and modeling study on the autoignition properties of ammonia at intermediate temperatures, Proc. Combust. Inst. 37 (2019) 205–211.
[24] X. He, B. Shu, D. Nascimento, K. Moshammer, M. Costa, R.X. Fernandes, Auto-ignition kinetics of ammonia and ammonia/hydrogen mixtures at intermediate temperatures and high pressures, Combust. Flame. 206 (2019) 189–200.
[25] A.A. Konnov, J. De Ruyck, A possible new route for no formation via N_2H_3, Combust. Sci. Technol. 168 (2001) 1–46.
[26] Y. Zhang, O. Mathieu, E.L. Petersen, G. Bourque, H.J. Curran, Assessing the predictions of a NO_x kinetic mechanism on recent hydrogen and syngas experimental data, Combust. Flame. 182 (2017) 122–141.
[27] Y. Song, H. Hashemi, J.M. Christensen, C. Zou, P. Marshall, P. Glarborg, Ammonia oxidation at high pressure and intermediate temperatures, Fuel. 181 (2016) 358–365.
[28] P. Dagaut, A. Nicolle, Experimental and kinetic modeling study of the effect of SO_2 on the reduction of NO by ammonia, Proc. Combust. Inst. 30 (2005) 1211–1217.
[29] H. Nakamura, S. Hasegawa, T. Tezuka, Kinetic modeling of ammonia/air weak flames in a micro flow reactor with a controlled temperature profile, Combust. Flame. 185 (2017) 16–27.
[30] P. Glarborg, J.A. Miller, B. Ruscic, S.J. Klippenstein, Modeling nitrogen chemistry in combustion, Prog. Energy Combust. Sci. 67 (2018) 31–68.
[31] S.J. Klippenstein, L.B. Harding, P. Glarborg, J.A. Miller, The role of NNH in NO formation and control, Combust. Flame. 158 (2011) 774–789.
[32] L. Yu, Y. Feng, W. Wang, J. Zhu, Y. Qian, X. Lu, Combustion and Flame The effect of ammonia addition on the low-temperature autoignition of n-heptane : An experimental and modeling study, Combust. Flame. 217 (2020) 4–11.
[33] K. Zhang, C. Banyon, J. Bugler, H.J. Curran, A. Rodriguez, O. Herbinet, F. Battin-Leclerc, C. B'Chir, K.A. Heufer, An updated experimental and kinetic modeling study of n-heptane oxidation, Combust. Flame. 172 (2016) 116–135.
[34] H.J. Curran, W.J. Pitz, C.K. Westbrook, P. Dagaut, J.-C. Boettner, M. Cathonnet, A Wide Range Modeling Study of Dimethyl Ether Oxidation, Int. J. Chem. Kinet. 30 (1998) 229–241.
[35] U. Burke, K.P. Somers, P. O'Toole, C.M. Zinner, N. Marquet, G. Bourque, E.L. Petersen, W.K. Metcalfe, Z. Serinyel, H.J. Curran, An ignition delay and kinetic modeling study of methane, dimethyl ether, and their mixtures at high pressures, Combust. Flame. 162 (2015) 315–330.
[36] E.E. Dames, A.S. Rosen, B.W. Weber, C.W. Gao, C.-J. Sung, W.H. Green, A detailed combined experimental and theoretical study on dimethyl ether/propane blended oxidation, Combust. Flame. 168 (2016) 310–330.
[37] G. Mittal, M. Chaos, C.-J. Sung, F.L. Dryer, Dimethyl ether autoignition in a rapid compression machine: Experiments and chemical kinetic modeling, Fuel Process. Technol. 89 (2008) 1244–1254.
[38] H. Wang, R. Fang, B.W. Weber, C.-J. Sung, An experimental and modeling study of dimethyl ether/methanol blends autoignition at low temperature, Combust. Flame. 198 (2018) 89–99.
[39] H. Wu, Z. Shi, C. Lee, H. Zhang, Y. Xu, Experimental and kinetic study on ignition of DME/n-butane mixtures under high pressures on a rapid compression machine, Fuel. 225 (2018) 35–46.
[40] R.T.E. Hermanns, A.A. Konnov, R.J.M. Bastiaans, L.P.H. de Goey, K. Lucka, H. Koohne, Effects of temperature and composition on the laminar burning velocity of CH4 + H2 + O2 + N2 flames, Fuel. 89 (2010) 114–121.
[41] Z. Zhao, A. Kazakov, F.L. Dryer, Measurements of dimethyl ether/air mixture burning velocities by using particle image velocimetry, Combust. Flame. 139 (2004) 52–60.

[42] C.A. Daly, J.M. Simmie, J. Würmel, N. DjebaÏli, C. Paillard, Burning velocities of dimethyl ether and air, Combust. Flame. 125 (2001) 1329–1340.
[43] R. John, V.R. Kishore, M. Akram, Y. Yoon, S. Kumar, Burning velocities of DME (dimethyl ether) -air premixed flames at elevated temperatures, Energy. 126 (2017) 34–41.
[44] A. V. Sepman, A. V. Mokhov, H.B. Levinsky, Extending the predictions of chemical mechanisms for hydrogen combustion: Comparison of predicted and measured flame temperatures in burner-stabilized, 1-D flames, Int. J. Hydrogen Energy. 36 (2011) 9298–9303.
[45] J. Warnatz, U. Maas, R.W. Dibble, Combustion, 4th ed., Springer Berlin Heidelberg, 2006.
[46] V. Gururajan, F.N. Egolfopoulos, Direct sensitivity analysis for ignition delay times, Combust. Flame. 209 (2019) 478–480.
[47] D.G. Goodwin, H.K. Moffat, R.L. Speth, Cantera: An Object-oriented Software Toolkit for Chemical Kinetics, Thermodynamics, and Transport Processes. Version 2.3.0, (2017).
[48] J.P. Botha, D.. Spalding, The laminar flame speed of propane/air mixtures with heat extraction from the flame, Proc. R. Soc. Lond. A. Math. Phys. Sci. 225 (1954) 71–96.
[49] K. R.J, G. J.F., M.D. Smooke, J.A. Miller, M. E., Premix: A program for modeling steady, laminar, one-dimensional premixed flames, Reaction Design, San Diego, 1998.
[50] C.F. Curtiss, J.O. Hirschfelder, Transport properties of multicomponent gas mixtures, J. Chem. Phys. 17 (1949) 550–555.
[51] R.J. Kee, M.E. Coltrin, P. Glarborg, H. Zhu, Chemically Reacting Flow:Theory, Modeling, and Simulation, Second Edition, Wiley, 2017.
[52] H. Hashemi, J.M. Christensen, S. Gersen, P. Glarborg, Hydrogen oxidation at high pressure and intermediate temperatures: Experiments and kinetic modeling, Proc. Combust. Inst. 35 (2015) 553–560.
[53] C.K. Westbrook, Chemical kinetics of hydrocarbon ignition in practical combustion systems, Proc. Combust. Inst. 28 (2000) 1563–1577.
[54] U. Maas, J. Warnatz, Ignition Processes in Hydrogen-Oxygen Mixtures, Combust. Flame. 74 (1988) 53–69.
[55] A. Kéromnès, W.K. Metcalfe, K.A. Heufer, N. Donohoe, A.K. Das, C.J. Sung, J. Herzler, C. Naumann, P. Griebel, O. Mathieu, M.C. Krejci, E.L. Petersen, W.J. Pitz, H.J. Curran, An experimental and detailed chemical kinetic modeling study of hydrogen and syngas mixture oxidation at elevated pressures, Combust. Flame. 160 (2013) 995–1011.
[56] F. Behrendt, J. Warnatz, The dependence of flame propagation in H_2-O_2-N_2 mixtures on temperature, pressure, and initial composition, Int. Assoc. Hydrog. Energy. 10 (1985) 749–755.
[57] G.E. Burcat, A. Ruscic B, Ideal gas thermochemical database with updates from active thermochemical tables, Http://Garfield.Chem.Elte.Hu/Burcat/Burcat.Html. (2016).
[58] B.J. Mcbride, S. Gordon, Properties and coefficients, computer program fro calculating and fitting thermodynamic functions, National Aeronautics and Space Administration, Blenn Research Center, OH, 1999.
[59] B. Ruscic, Active Thermochemical Tables: Sequential Bond Dissociation Enthalpies of Methane, Ethane, and Methanol and the Related Thermochemistry, J. Phys. Chem. A. 119 (2015) 7810–7837.
[60] C.K. Westbrook, F.L. Dryer, Chemical kinetic modeling of hydrocarbon combustion, Prog. Energy Combust. Sci. 10 (1984) 1–57.
[61] J.A. Miller, R.J. Kee, C.K. Westbrook, Chemical Kinetics and Combustion Modeling, Annu. Rev. Phys. Chem. 41 (1990) 345.
[62] M. Frenklach, H. Wang, M.J. Rabinowitz, Optimization and analysis of large chemical kinetic mechanisms using the solution mapping method-combustion of methane, Prog. Energy Combust. Sci. 18 (1992) 47–73.
[63] C.J. Howard, Kinetic measurements using flow tubes, J. Phys. Chem. 83 (1979) 3–9.
[64] L. Pan, S. Kokjohn, Z. Huang, Development and validation of a reduced chemical kinetic model

for dimethyl ether combustion, Fuel. 160 (2015) 165–177.
[65] M.C. Lee, S. Bin Seo, J.H. Chung, Y.J. Joo, D.H. Ahn, Industrial gas turbine combustion performance test of DME to use as an alternative fuel for power generation, Fuel. 88 (2009) 657–662.
[66] D.M. Golden, Experimental and theoretical examples of the value and limitations of transition state theory, J. Phys. Chem. 83 (1979) 108–113.
[67] H.J. Curran, Developing detailed chemical kinetic mechanisms for fuel combustion, Proc. Combust. Inst. 37 (2019) 57–81.
[68] S.J. Klippenstein, L.B. Harding, M.J. Davis, A.S. Tomlin, R.T. Skodje, Uncertainty driven theoretical kinetics studies for CH_3OH ignition: $HO_2 + CH_3OH$ and $O_2 + CH_3OH$, Proc. Combust. Inst. 33 (2011) 351–357.
[69] M. Altarawneh, A.H. Al-Muhtaseb, B.Z. Dlugogorski, E.M. Kennedy, J.C. Mackie, Rate constants for hydrogen abstraction reactions by the hydroperoxyl radical from methanol, ethenol, acetaldehyde, toluene, and phenol, J. Comput. Chem. 32 (2011) 1725–1733.
[70] L. Dai, S. Gersen, P. Glarborg, H. Levinsky, A. Mokhov, Experimental and numerical analysis of the autoignition behavior of NH_3 and NH_3/H_2 mixtures at high pressure, Combust. Flame. 215 (2020) 134–144.
[71] J. Gao, Y. Nakamura, Low-temperature ignition of dimethyl ether: Transition from cool flame to hot flame promoted by decomposition of HPMF (HO_2CH_2OCHO), Combust. Flame. 165 (2016) 68–82.
[72] R.K. Hanson, D.F. Davidson, Recent advances in laser absorption and shock tube methods for studies of combustion chemistry, Prog. Energy Combust. Sci. 44 (2014) 103–114.
[73] S.S. Goldsborough, S. Hochgreb, G. Vanhove, M.S. Wooldridge, H.J. Curran, C.-J. Sung, Advances in rapid compression machine studies of low- and intermediate-temperature autoignition phenomena, Prog. Energy Combust. Sci. 63 (2017) 1–78.
[74] G.A. Pang, D.F. Davidson, R.K. Hanson, Experimental study and modeling of shock tube ignition delay times for hydrogen-oxygen-argon mixtures at low temperatures, Proc. Combust. Inst. 32 I (2009) 181–188.
[75] C.J. Sung, H.J. Curran, Using rapid compression machines for chemical kinetics studies, Prog. Energy Combust. Sci. 44 (2014) 1–18.
[76] S. Tanaka, F. Ayala, J.C. Keck, J.B. Heywood, Two-stage ignition in HCCI combustion and HCCI control by fuels and additives, Combust. Flame. 132 (2003) 219–239.
[77] S. Gersen, Experimental study of the combustion properties of methane / hydrogen mixtures, Ph.D. Thesis, University of Groningen,http://hdl.handle.net/11370/8161b901-4e2b-40dd-8140-c926a9243a4e, 2007.
[78] P. Park, J.C. Keck, Rapid Compression Machine Measurements of Ignition Delays for Primary Reference Fuels, in: SAE Tech. Pap., SAE International, 1990.
[79] S. Gersen, A. V. Mokhov, J.H. Darmeveil, H.B. Levinsky, Ignition properties of n-butane and iso-butane in a rapid compression machine, Combust. Flame. 157 (2010) 240–245.
[80] H.J. Curran, P. Gaffuri, W.J. Pitz, C.K. Westbrook, A Comprehensive Modeling Study of n-Heptane Oxidation, Combust. Flame. 114 (1998) 149–177.
[81] S. Tanaka, F. Ayala, J.C. Keck, A reduced chemical kinetic model for HCCI combustion of primary reference fuels in a rapid compression machine, Combust. Flame. 133 (2003) 467–481.
[82] A.V. Sepman, Effects of burner stabilization on nitric oxide formation and destruction in atmospheric-pressure flat premixed flames, Ph.D. Thesis, University of Groningen, 2006.
[83] A.C. Eckbreth, Laser Diagnostics for Combustion Temperature and Species, Second Edi, Gordon and Breach, 1996.
[84] P.N. Langenkamp, Laser diagnostics of combustion-generated nanoparticles, University of Groningen, 2018.
[85] A. V. Sepman, V. V. Toro, A. V. Mokhov, H.B. Levinsky, Determination of temperature and

concentrations of main components in flames by fitting measured Raman spectra, Appl. Phys. B Lasers Opt. 112 (2013) 35–47.

[86] K.P. Shrestha, L. Seidel, T. Zeuch, F. Mauss, Detailed Kinetic Mechanism for the Oxidation of Ammonia Including the Formation and Reduction of Nitrogen Oxides, Energy and Fuels. 32 (2018) 10202–10217.

[87] S.J. Klippenstein, L.B. Harding, B. Ruscic, R. Sivaramakrishnan, N.K. Srinivasan, M.C. Su, J. V. Michael, Thermal decomposition of NH_2OH and subsequent reactions: Ab initiotransition state theory and reflected shock tube experiments, J. Phys. Chem. A. 113 (2009) 10241–10259.

[88] P. Van Khe, J.C. Soulignac, R. Lesclaux, Pressure and temperature dependence of NH2recombination rate constant, J. Phys. Chem. 81 (1977) 210–214.

[89] V.A. Lozovskii, V.A. Nadtochenko, O.M. Sarkisov, S.G. Cheskis, Study of NH_2 radical recombination by intraresonator laser spectroscopy, Kinet. Catal. 20 (1979) 918–922.

[90] O.M. Sarkisov, S.G. Cheskis, V.A. Nadtochenko, E.A. Sviridenkov, V.I. Vedeneev, Spectroscopic study of elementary reactions involving HCO, NH2 and HNO, Arch. Combust. 4 (1984) 111–120.

[91] K. Fagerström, J.T. Jodkowski, A. Lund, E. Ratajczak, Kinetics of the self-reaction and the reaction with OH of the amidogen radical, Chem. Phys. Lett. 236 (1995) 103–110.

[92] G. Altinay, R.G. MacDonald, Determination of the rate constant for the NH_2(X2B1) + NH_2(X2B1) recombination reaction with collision partners He, Ne, Ar, and N_2 at low pressures and 296 K. Part 1, J. Phys. Chem. A. 116 (2012) 1353–1367.

[93] R.W. Diesen, Mass spectral studies of kinetics behind shock waves. II. Thermal decomposition of hydrazine, J. Chem. Phys. 39 (1963) 2121–2128.

[94] E. Meyer, H.A. Olschewski, J. Troe, H.G. Wagner, Investigation of N_2H_4 and H_2O_2 decomposition in low and high pressure shock waves, in: Symp. Combust., Elsevier, 1969: pp. 345–355.

[95] P. Genich, A.A. Zhirnov, G.B. Manelis, Decomposition of Hydrazine behind Reflected Shock Waves at High Pressures, Zh, Phys. Khim. 48 (1974) 728–729.

[96] O. V. Dorofeeva, O.N. Ryzhova, T.A. Suchkova, Enthalpies of Formation of Hydrazine and Its Derivatives, J. Phys. Chem. A. 121 (2017) 5361–5370.

[97] D. Feller, D.H. Bross, B. Ruscic, Enthalpy of Formation of N_2H_4 (Hydrazine) Revisited, J. Phys. Chem. A. 121 (2017) 6187–6198.

[98] Y. Wu, Y. Liu, C. Tang, Z. Huang, Ignition delay times measurement and kinetic modeling studies of 1-heptene, 2-heptene and n-heptane at low to intermediate temperatures by using a rapid compression machine, Combust. Flame. 197 (2018) 30–40.

[99] U. of C. at S.D. Mechanical and Aerospace Engineering (Combustion Research), Chemical-Kinetic Mechanisms for Combustion Applications, http://web.eng.ucsd.edu/mae/groups/combustion/mechanism.html, (2014).

[100] Z. Tian, Y. Li, L. Zhang, P. Glarborg, F. Qi, An experimental and kinetic modeling study of premixed $NH_3/CH_4/O_2$/Ar flames at low pressure, Combust. Flame. 156 (2009) 1413–1426.

[101] R. Li, A.A. Konnov, G. He, F. Qin, D. Zhang, Chemical mechanism development and reduction for combustion of NH3/H2/CH4 mixtures, Fuel. 257 (2019) 116059.

[102] E.C. Okafor, Y. Naito, S. Colson, A. Ichikawa, T. Kudo, A. Hayakawa, H. Kobayashi, Experimental and numerical study of the laminar burning velocity of CH_4–NH_3–air premixed flames, Combust. Flame. 187 (2018) 185–198.

[103] S. Gersen, N.B. Anikin, A. V. Mokhov, H.B. Levinsky, Ignition properties of methane/hydrogen mixtures in a rapid compression machine, Int. J. Hydrogen Energy. 33 (2008) 1957–1964.

[104] H. Hashemi, J.M. Christensen, S. Gersen, H. Levinsky, S.J. Klippenstein, P. Glarborg, High-pressure oxidation of methane, Combust. Flame. 172 (2016) 349–364.

[105] S. Gersen, H. Darmeveil, H. Levinsky, The effects of CO addition on the autoignition of H2, CH4 and CH4/H2 fuels at high pressure in an RCM, Combust. Flame. 159 (2012) 3472–3475.

[106] R.D. Büttgen, T. Raffius, G. Grünefeld, H.J. Koß, A. Heufer, High-speed imaging of the ignition of ethanol at engine relevant conditions in a rapid compression machine, Proc. Combust. Inst. 37 (2019) 1471–1478.
[107] M. Figueroa-Labastida, J. Badra, A.M. Elbaz, A. Farooq, Shock tube studies of ethanol preignition, Combust. Flame. 198 (2018) 176–185.
[108] B.W. Weber, C.J. Sung, Comparative autoignition trends in butanol isomers at elevated pressure, Energy and Fuels. 27 (2013) 1688–1698.
[109] G. Mittal, M.P. Raju, C.J. Sung, CFD modeling of two-stage ignition in a rapid compression machine: Assessment of zero-dimensional approach, Combust. Flame. 157 (2010) 1316–1324.
[110] L. Dai, S. Gersen, P. Glarborg, A. Mokhov, H. Levinsky, Autoignition studies of NH_3/CH_4 mixtures at high pressure, Combust. Flame. 218 (2020) 19–26.
[111] H. Hashemi, J.M. Christensen, P. Glarborg, High-pressure pyrolysis and oxidation of DME and DME/CH_4, Combust. Flame. 205 (2019) 80–92.
[112] J. Gao, Y. Guan, J. Lou, H. Ma, J. Song, Kinetic modeling for unimolecular B-scission of the methoxymethyl radical from quantum chemical and RRKM analyses, Combust. Flame. (2018).
[113] A.M. Mebel, M.C. Lin, Prediction of Absolute Rate Constants for the Reactions of NH_2 with Alkanes from ab Initio G2M/TST Calculations, J. Phys. Chem. A. 103 (1999) 2088–2096.
[114] Q.S. Li, R.H. Lü, Direction Dynamics Study of the Hydrogen Abstraction Reaction $CH_2O + NH_2 \rightarrow CHO + NH_3$, J. Phys. Chem. A. 106 (2002) 9446–9450.
[115] J.T. Jodkowski, E. Ratajczak, K. Fagerström, A. Lund, N.D. Stothard, R. Humpfer, H.-H. Grotheer, Kinetics of the cross reaction between amidogen and methyl radicals, Chem. Phys. Lett. 240 (1995) 63–71.
[116] M. Votsmeier, S. Song, D.F. Davidson, R.K. Hanson, Sensitive detection of NH_2 in shock tube experiments using frequency modulation spectroscopy, Int. J. Chem. Kinet. 31 (1999) 445–453.
[117] P. Glarborg, C.S. Andreasen, H. Hashemi, R. Qian, P. Marshall, Oxidation of methylamine, Int. J. Chem. Kinet. 52 (2020) 893–906.
[118] G. Issayev, B.R. Giri, A.M. Elbaz, W.L. Roberts, A. Farooq, Combustion Behaviour of Ammonia Blended with Dimethyl Ether, in: 9th Eur. Combust. Meet., Lisboa, Portugal, 2019.
[119] G.P. Smith, D.M. Golden, M. Frenklach, N.W. Moriarty, B. Eiteneer, M. Goldenberg, T. c. Bowman, R.K. Hanson, S. Song, W.C. Gardiner, J.V. V. Lissianski, Z. Qin, http://combustion.berkeley.edu/gri-mech/, (n.d.).
[120] S. Gersen, A. V. Mokhov, J.H. Darmeveil, H.B. Levinsky, P. Glarborg, Ignition-promoting effect of NO_2 on methane, ethane and methane/ethane mixtures in a rapid compression machine, Proc. Combust. Inst. 33 (2011) 433–440.
[121] X. Qin, Y. Ju, Measurements of burning velocities of dimethyl ether and air premixed flames at elevated pressures, Proc. Combust. Inst. 30 (2005) 233–240.
[122] Z. Huang, Q. Wang, J. Yu, Y. Zhang, K. Zeng, H. Miao, D. Jiang, Measurement of laminar burning velocity of dimethyl ether-air premixed mixtures, Fuel. 86 (2007) 2360–2366.
[123] H. Yu, E. Hu, Y. Cheng, X. Zhang, Z. Huang, Experimental and numerical study of laminar premixed dimethyl ether/methane–air flame, Fuel. 136 (2014) 37–45.
[124] R.J. Kee, M.E. Coltrin, P. Glarborg, Chemically reacting flow : theory and practice TT -, Wiley-Interscience, Hoboken, NJ :, 2003.
[125] Y. Liu, B. Rogg, Prediction of radiative heat transfer in laminar flames, Combust. Sci. Technol. 118 (1996) 127–145.
[126] Sandia national lab TNF workshop, http://www.sandia.gov/TNF/radiation.html, (n.d.).
[127] W.L. Grosshandler, RADCAL: A Narrow-Band Model for Radiation Calculations in a Combustion Environment, NIST Tech. Note. (1993).
[128] Z. Zhao, M. Chaos, A. Kazakov, F.L. Dryer, Thermal decomposition reaction and a comprehensive kinetic model of dimethyl ether, Int. J. Chem. Kinet. 40 (2008) 1–18.
[129] D. Liu, J. Santner, C. Togbé, D. Felsmann, J. Koppmann, A. Lackner, X. Yang, X. Shen, Y. Ju,

K. Kohse-Höinghaus, C. Togb, D. Felsmann, J. Koppmann, A. Lackner, X. Yang, X. Shen, Y. Ju, Kohse-Hinghaus, Katharina, Flame structure and kinetic studies of carbon dioxide-diluted dimethyl ether flames at reduced and elevated pressures, Combust. Flame. 160 (2013) 2654–2668.

[130] M.P. Burke, M. Chaos, Y. Ju, F.L. Dryer, S.J. Klippenstein, Comprehensive H_2/O_2 kinetic model for high-pressure combustion, Int. J. Chem. Kinet. 44 (2012) 444–474.

[131] M.I. Hassan, K.T. Aung, G.M. Faeth, Measured and predicted properties of laminar premixed methane/air flames at various pressures, Combust. Flame. 115 (1998) 539–550.

[132] L.P.H. de Goey, A. van Maaren, R.M. Quax, Stabilization of Adiabatic Premixed Laminar Flames on a Flat Flame Burner, Combust. Sci. Technol. 92 (1993) 201–207.

[133] T.F. Guiberti, C. Garnier, P. Scouflaire, J. Caudal, B. Labegorre, T. Schuller, N. Darabiha, Experimental and numerical analysis of non-catalytic partial oxidation and steam reforming of $CH_4/O_2/N_2/H_2O$ mixtures including the impact of radiative heat losses, Int. J. Hydrogen Energy. 41 (2016) 8616–8626.

[134] S. Haider, Paper NO.: 274 Combustion and radiation modeling of laminar premixed flames using OpenFOAM : A numerical investigation of radiative heat transfer in the RADIADE project, 27th CIMAC World Congr. (2013).

[135] N. Lamoureux, K. Marschallek-Watroba, P. Desgroux, J.F. Pauwels, M.D. Sylla, L. Gasnot, Measurements and modelling of nitrogen species in $CH_4/O_2/N_2$ flames doped with NO, NH_3, or NH_3+NO, Combust. Flame. 176 (2017) 48–59.

[136] H. Yu, E. Hu, Y. Cheng, K. Yang, X. Zhang, Z. Huang, Effects of hydrogen addition on the laminar flame speed and markstein length of premixed dimethyl ether-air flames, Energy and Fuels. 29 (2015) 4567–4575.

[137] E. Ranzi, A. Frassoldati, R. Grana, A. Cuoci, T. Faravelli, A.P. Kelley, C.K. Law, Hierarchical and comparative kinetic modeling of laminar flame speeds of hydrocarbon and oxygenated fuels, Prog. Energy Combust. Sci. 38 (2012) 468–501.

[138] J. De Vries, W.B. Lowry, Z. Serinyel, H.J. Curran, E.L. Petersen, Laminar flame speed measurements of dimethyl ether in air at pressures up to 10 atm C3 mechanism is used here, Fuel. 90 (2011) 331–338.

[139] J. Warnatz, The structure of laminar alkane-, alkene-, and acetylene flames, Symp. Combust. 18 (1981) 369–384.

[140] A.A. Konnov, The effect of temperature on the adiabatic laminar burning velocities of CH_4-air and H_2-air flames, Fuel. 89 (2010) 2211–2216.

[141] W.K. Metcalfe, S.M.S.M. Burke, S.S. Ahmed, H.J. Curran, A hierarchical and comparative kinetic modeling study of C1 - C2 hydrocarbon and oxygenated fuels, Int. J. Chem. Kinet. 45 (2013) 638–675.

[142] R. Sivaramakrishnan, J. V. Michael, A.F. Wagner, R. Dawes, A.W. Jasper, L.B. Harding, Y. Georgievskii, S.J. Klippenstein, Roaming radicals in the thermal decomposition of dimethyl ether: Experiment and theory, Combust. Flame. 158 (2011) 618–632.

[143] R.S. Tranter, P.T. Lynch, X. Yang, Dissociation of dimethyl ether at high temperatures, Proc. Combust. Inst. 34 (2013) 591–598.

Acknowledgements

This thesis can never be completed without the help from my supervisors, family and friends. First of all, I would like to thank Prof. Howard Levinsky and Dr. Anatoli Mokhov for their guidance and encouragement with wisdom and humor. I benefited not only from their supervision in my researches, but also from the philosophy they shared with me about how to do scientific research properly. For sure, I shall always remember their advice, 'take care of the data and data will tell the story'.

I received great help from Prof. Peter Glarborg at Technical University of Denmark; I want to express my gratitude to him for providing ammonia combustion mechanisms and collaborating in writing articles.

Furthermore, I sincerely appreciate the help from my colleagues at DNVGL, Dr. Sander Gersen and Dr. Martijn van Essen for their useful discussions on RCM experiments and Harry Darmeveil for teaching me the operation of RCM setup. I thank my colleague Peter Langenkamp for teaching me the operation of Raman setup with patience and having interesting discussions beyond researches. Besides, I also thank Bahram Nourani and Jiawei Cao for sharing a good time with them.

I would like to thank the members of the reading committee, Prof. T. Van Der Meer, Prof. A. Purushothaman Vellayani and Prof. D. Roekaerts, for reviewing this thesis and providing constructive remarks.

Last but not least, I want to thank my parents and sisters, I could never have reached this point without their unconditional love.

博士毕业时我已过而立之年，父母亲则已年近古稀，感谢你们这么多年含辛茹苦，供我读书，教我做人。如今少小离家老大回，惟愿天增岁月人增寿，青丝虽已见白发，常伴左右无牵挂。

Liming Dai
Groningen
September 7, 2020